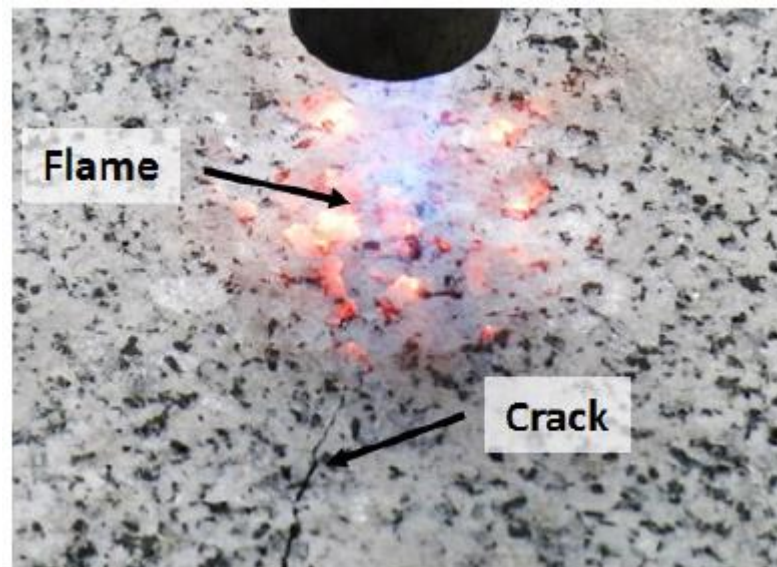




Schlussbericht vom 21. Juli 2017

Untersuchung der Anwendungsmöglichkeiten von Hydrothermal Spallation Drilling für die Erschliessung von geothermischen Tiefenreservoirs



Quelle: Thermal Spallation Drilling: Application Possibilities and Viability Assessment of a Novel Drilling Technology, 2017



ETH zürich

Datum: 21. Juli 2017

Ort: Bern

Subventionsgeberin:

Bundesamt für Energie BFE
Sektion Energieforschung und Cleantech
CH-3003 Bern
www.bfe.admin.ch

Subventionsempfänger/innen:

ETH Zürich
Institut für Verfahrenstechnik
Sonneggstrasse 3
8092 Zürich
<https://ipe.ethz.ch/>

Autor/in:

Michael Kant, Institut für Verfahrenstechnik, ETH Zürich, kant@ipe.mavt.ethz.ch

BFE-Projektbegleitung:

Gunter Siddiqi, gunter.siddiqi@bfe.admin.ch

BFE-Vertragsnummer: SI/500676-02

Für den Inhalt und die Schlussfolgerungen sind ausschliesslich die Autoren dieses Berichts verantwortlich.

DISS. ETH NO. 24582

Thermal Spallation Drilling: Application Possibilities and Viability Assessment of a Novel Drilling Technology

A thesis submitted to attain the degree of
DOCTOR OF SCIENCES of ETH ZURICH
(Dr. sc. ETH Zurich)

presented by
MICHAEL ALEXANDER KANT
Dipl.-Ing., Karlsruhe Institute of Technology

born on 03.12.1987
citizen of Germany

accepted on the recommendation of
Prof. Dr. Dr. h.c. Philipp Rudolf von Rohr (ETH Zurich), examiner
Dr. Gunter Siddiqi (Swiss Federal Office of Energy), co-examiner
Prof. Dr. Martin Saar (ETH Zurich), co-examiner

2017

We are at the very beginning of time for the human race. It is not unreasonable that we grapple with problems. But there are tens of thousands of years in the future. Our responsibility is to do what we can, learn what we can, improve the solutions, and pass them on.

Richard Feynman

Preface

Writing this thesis was quite a journey. Therefore, I would like to take the chance to thank several people.

First of all, I want to express my gratitude to my doctoral advisor Prof. Philipp Rudolf von Rohr. He gave me the freedom to develop my own ideas and the support for the projects conducted in this thesis. I enjoyed the countless scientific discussions with him and the time he spent for me. Secondly, I would like to sincerely thank my co-advisor Dr. Gunter Siddiqi. Regardless of his busy schedule, he always found the time to help me with problems, to discuss the recent developments and to give me the hints I was looking for. His ideas and comments significantly contributed to this thesis and were certainly advancing for my personal and professional development. In addition, many thanks to Prof. Martin Saar for also co-advising my thesis. I appreciate the enthusiasm you have for spallation drilling and I hope that you bring the technology to success in the future.

Additionally, I would like to thank all my current and former colleagues at LTR for the excellent working atmosphere and the time we spent together in H-Floor. We had a great time together, floating down the Limmat, skiing everywhere in Switzerland, biking up the Klausen Pass, watching football in the students room, enjoying the Riviera Party in Nice or the driving range in Stanford, making Feuerzangenbowle or various other things. Even though this thanks goes to everybody from the institute, I have to name a few people individually, who worked with me on thermal spallation drilling and helped me throughout my thesis: Edoardo, thank you for the great help since you started your master thesis with me and now your PhD at LTR. Martin, thank you for the 24-7 support. You were always there, if something went wrong, even when you had your head full of other things. Claudio, thank you for your geological consulting services. You taught me what a rock is and without you I would still mix up Granites and Sandstones. Thanks to my long-term office colleagues (Helena, Roger, Marco, Thomas, Christoph and Sergio) for bearing with me in the office for nearly 4 years. Additionally, I sincerely want to thank all the students who supported me in my doctoral studies: the master thesis of Edoardo and Jonas, the long term help of Oliver, Dustin who is now a colleague here at LTR and all my other

students (Lukas, Raphael, Gian, Damian, Alex, Joachim and Martin). The successful completion of my doctoral thesis would not have been possible without the support of our excellent workshop. I have to thank Peter, Stefan, Daniel, Bruno and Rene for their great support, especially during the Grimsel project. You were always extremely valuable for me and never annoyed, even if I came with some last minute requests. I also enjoyed the various discussion with you guys, which certainly helped me to become a better engineer.

There are some more people and surely I cannot list all of them. But I will miss the time with all of you here at ETH.

I thank the people from the Grimsel Test Site who help me to run our big field test (Flo, Linus, Rene, Michael, Ingo, Hansruedi). We thoroughly enjoyed the time in the tunnel, even though we had to learn some hard lessons about the real drilling life. Very special thanks also to Bochum (Shahin, Volker, Denis) for the great adventure, which is called the hybrid project.

What would live be without friends? I thank all my friends for the endless discussion you shared with me about drilling a rock with a flame, for building me up in bad times and for giving me excellent breaks from my work to get my mind free. Finally, I would like to cordially thank my family for the support they provided me, the trust in my ideas and for teaching me what really matters in life. And last but not least, I thank Lisa for her support not only during my PhD but in my life in general. I'm looking very much forward to our common future.

Abstract

In order to promote the development of geothermal energy production from deep resources, cost effective solutions to increase the drilling performance have to be developed. Currently, the drilling costs account for up to 70% of the total investment for a deep geothermal project. Besides the different attempts to intensify the conventional drilling process, several emerging technologies are currently investigated by researchers around the world. One of these alternative technologies is the spallation technology, which is based on the effect of hard, crystalline rocks disintegrating into small fragments, if rapidly heated by a hot fluid jet. Thermal spallation drilling has the benefits of high penetration rates in hard rock formations, an efficient energy transport to the bit and reduced wear-rates. Previous research has indicated that these benefits could lead to a decrease of the drilling costs and therewith to a boost in the development of geothermal energy production from deep resources. Even though, thermal spallation drilling is used since decades for hard rock excavation, no deep bore hole has been drilled with the technology, as some important questions remain still open. The presented thesis aims at closing these open questions and to demonstrate the application possibilities of thermal spallation drilling and its operational readiness. Thereby, the deeper understanding of the physics of the spallation process and their transfer to practical applications shall be an essential building block for the discussion about this technology.

In order to assess the viability and the economical aspects of thermal spallation drilling without extensive full-scale experiments, a comprehensive modeling approach is required. This model has to be capable to predict the operating conditions of a thermal spallation drill head, which are required to drill a certain formation with a desired drilling velocity without any further calibration measurements. Only if such a model is available, an economical assessment of the technology, evaluating if thermal spallation drilling can reduce the drilling costs, is possible. Therefore, two interlinked models are presented. The first model is based on a linear fracture mechanical consideration and can be used to predict the operating conditions, which are required to drill a certain rock formation and to assess the spallability of rock formations. The second model

is based on an analytical heat transfer approach and predicts the drilling velocity, which can be reached by using thermal spallation drilling, as a function of the drill head operating conditions and the prevailing rock formation. This model can also be used to design spallation drill heads with respect to the applied combustion reaction and the required jet velocities.

After the introduction of the spallation model, opportunities and challenges for thermal spallation drilling in deep drilling operations are discussed. A case study is conducted, comparing the investments, which are required to drill an exemplary well with thermal spallation drilling and with conventional drilling methods. Therewith, it gives a perspective on the financial aspects of thermal spallation projects in great depths. Thereafter, the differences between laboratory experiments and drilling operations in deep bore holes are discussed. Finally, supply solutions for the reactive fluids, required to establish the flame-jet, are assessed and their applicability is investigated. The chapter closes with a recommendation of the application possibilities of thermal spallation drilling and with a discussion, which limitations restrict the use of this technology.

In order to solve the revealed issues of stand-alone thermal spallation drilling, a combination of spallation drilling and mechanical drilling is investigated. The principles of such a combined drilling method are assessed together with its potential benefits. In order to demonstrate the general feasibility of a thermo-mechanical drilling system, a first feasibility study by means of thermal treatments is conducted and implementation possibilities are discussed. The applicability of this hybrid system is demonstrated in a full-scale hybrid drilling system, designed in cooperation with the Geothermal Center in Bochum (GZB). This system has a length of about 11m and a diameter of 140mm. The design aspects of the system are discussed and the drill head is tested in a laboratory environment. With these experiments, the feasibility of a combined system is shown and its potential impact on the enhancement of geothermal energy production is revealed.

Additionally, a novel process is developed in this thesis, which utilizes thermal spallation drilling to enhance and enlarge the bore hole diameter in the reservoir section of the well. Thermal bore hole enlargement aims at removing near well bore impedances, enhancing the access to natural fractures and providing efficient fracture initiation points for hydraulic stimulation. Therewith, the developed technology has the potential to reduce the efforts of hydraulic stimulation and to increase the production rate of a well. The principles of this process are introduced and a process procedure is developed, which facilitates the application in deep bore holes. The operational readiness of the technology is shown in a field test conducted in the Grimsel Test Site. Two different enlargement geometries could be successfully drilling in a water-filled bore hole in a maximal depth of 13.8m.

In summary, this thesis discusses the viability of thermal spallation drilling for deep drilling operations. Two major application possibilities are revealed: a combined thermo-mechanical drilling system for drilling deep wells in hard rock sections and thermal bore hole enlargement, to increase the diameter in the production zone of the well. For each of this two technologies a field test is conducted or prepared, demonstrating the operational readiness of the systems, which could be achieved during the progression of this project. Therewith, the thesis shows that thermal spallation drilling can contribute to the development of geothermal energy production from deep resources, as it can be used to enhance the drilling process and to increase the production rate.

Zusammenfassung

Um die Entwicklung von Tiefengeothermie zu fördern, werden kostengünstige Bohrverfahren benötigt. Momentan beziehen sich bis zu 70% der Gesamtkosten für ein Geothermie Projekt nur auf den Bohrprozess. Daher werden weltweit, neben der Verbesserung der aktuellen Bohrentechnologie, andere kostengünstigere Verfahren gesucht. Eine mögliche neue Technologie ist Thermal Spallation Drilling. Diese Technologie basiert darauf, dass bestimmte Gesteine lokal zersplittern, wenn sie hohen thermischen Lasten ausgesetzt werden. Thermal Spallation Drilling hat den Vorteil, dass hohe Bohrgeschwindigkeiten erreicht werden können, die Energie effizient zum Bohrkopf transportiert werden kann und die Verschleissraten gesenkt werden können. Vorausgegangene Experimente haben gezeigt, dass diese Vorteile zu einer Kostenreduktion führen können, was die Entwicklung von Tiefengeothermie fördern würde. Obwohl Thermal Spallation Drilling schon seit Jahrzehnten zum Abtragen von harten Gesteinsstrukturen verwendet wird, wurde bis jetzt noch kein tiefes Bohrloch damit gebohrt, da einige prinzipiellen Fragen noch offen sind. Die vorliegende Arbeit versucht diese Fragen zu beantworten und die Anwendungsmöglichkeiten des Prozesses aufzuzeigen. Dabei basiert die Arbeit darauf die fundamentalen physikalischen Zusammenhänge zu verstehen und diese auf praktische Anwendungen zu transferieren.

Um die Realisierbarkeit und ökonomische Aspekte von Thermal Spallation Drilling ohne aufwendige Feldversuche diskutieren zu können, wird ein umfassendes Model des Prozesses benötigt. Dieses Model muss in der Lage sein ohne zusätzliche Messungen die Betriebsbedingungen eines thermischen Bohrkopfes vorherzusagen, die benötigten werden um eine bestimmte Gesteinsformation mit einer gewünschten Bohrgeschwindigkeit zu bohren. Nur wenn ein solches Model verfügbar ist, ist eine realistische Einschätzung, ob Thermal Spallation Drilling die Bohrkosten reduzieren kann, möglich. In der vorliegenden Arbeit werden zu diesem Zweck zwei gekoppelte Modelle vorgestellt. Das erste Model basiert auf einer bruchmechanischen Überlegung und schätzt die Betriebsbedingungen ab, die benötigt werden um eine bestimmte Gesteinsformation zu spallieren. Das zweite Model basiert auf einem analytischen Wärmeübertragungsmodel und berechnet die mögliche Bohrgeschwindigkeit.

keit von Thermal Spallation Drilling in Abhängigkeit von den Betriebsbedingungen und den Gesteinseigenschaften. Dieses Model kann zudem verwendet werden um thermische Bohrköpfe anhand der Verbrennungsreaktion und der Düsenaustrittsgeschwindigkeit auszulegen.

Nach dem diese Modelle vorgestellt wurden, werden die Chancen und Herausforderungen von Thermal Spallation Drilling in Tiefenbohrungen erörtert. Als erster Beweis der Wirtschaftlichkeit der Technologie wird eine Fallstudie durchgeführt, welche die Kosten von konventiollen Bohrtechnologien und Thermal Spallation Drilling vergleicht, die benötigt werden um ein beispielhaft ausgewähltes Bohrloch zu erstellen. Anhand dieser Fallstudie wird die Durchführbarkeit von Thermal Spallation Drilling diskutiert und sie erlaubt einen Ausblick auf die wirtschaftlichen Aspekte eines solchen Projektes. Danach werden die Unterschiede zwischen Versuchen im Labor und im Feld diskutieren und verschiedene Versorgungsmöglichkeiten für den thermischen Brennkopf vorgestellt. Das Kapitel endet mit einer Empfehlung wo Thermal Spallation Drilling eingesetzt werden kann und welchen Einschränkungen die Technologie unterliegt.

Um diese Einschränkungen aufzuheben, wird im darauffolgenden Kapitel ein Bohrtechnologie vorgestellt, welche thermische und mechanische Verfahren kombiniert. Die prinzipiellen Abläufe des Prozesses werden diskutiert, gemeinsam mit den potenziellen Vorteilen die sich aus der Anwendung ergeben. Um die Einsetzbarkeit des Prozesses zu zeigen wird eine Machbarkeitstudie anhand verschiedener thermo-mechanischer Versuche vorgestellt. Die Durchführbarkeit des Prozesses auch in tiefengeothermischen Projekten wird durch ein Feldversuch gezeigt, der in Kooperation mit dem Geothermie Zentrum in Bochum vorbereitet wurde. Das dabei verwendete System besitzt eine Länge von ca. 11m und einen Durchmesser von 140mm. Die Konstruktion dieses Systems wird diskutiert und der Bohrkopf wird im Labor auf seine Funktionsfähigkeit getestet.

Zudem wurde eine innovativer Prozess entwickelt der Thermal Spallation Drilling dazu verwendet, den Durchmesser eines bestehenden Bohrloches zu vergrössern. Thermal Bore Hole Enlargement beseitigt

Formationsschäden, die durch das Bohren verursacht wurden, verbessert den Zugang zu bereits vorhanden Rissen im Gestein und erstellt Sollbruchstellen für den hydraulischen Stimulationsvorgang. Damit hat diese Technologie das Potenzial den Stimulationsaufwand zu reduzieren und die Förderrate der Bohrung zu erhöhen. Die Grundlagen dieses Prozesses werden vorgestellt und ein Ablaufverfahren entwickelt, dass den Einsatz in grossen Tiefen ermöglicht. Die Einsatzbereitschaft der Technologie wird in einem Feldversuch gezeigt, der im Grimsel Untergrund Labor durchgeführt wurde. Zwei verschiedene Vergrösserungsgeometrien konnten erfolgreich in einer maximalen Tiefe von 13.8m in einem mit Wasser gefülltem Bohrloch gebohrt werden.

Zusammenfassend, zeigt diese Arbeit die Anwendungsmöglichkeiten von Thermal Spallation Drilling in der Tiefengeothermie. Zwei Hauptanwendungsfelder konnten identifiziert werden: Ein kombiniertes thermomechanisches Bohrverfahren für harte Gesteinsformationen und eine Bohrlochvergrösserung mittels Thermal Spallation Drilling. Für jede dieser beiden Anwendungsfelder wurde ein Feldversuch durchgeführt bzw. vorbereitet. Damit zeigt die vorliegende Arbeit, dass Thermal Spallation Drilling zur Entwicklung der Tiefengeothermie beitragen kann, da es genutzt werden kann um den Bohrvorgang zu verbessern und die Förderrate der Bohrung zu erhöhen.

Contents

Preface	II
Abstract	IV
Zusammenfassung	VII
Nomenclature	XVI
1 Introduction and motivation	1
1.1 Motivation	2
1.2 Objectives	3
1.3 Overview over the thesis	4
2 Background: geothermal energy and thermal spallation drilling	7
2.1 Deep geothermal systems - energy from the subsurface . .	10
2.1.1 Hydrothermal systems	10
2.1.2 Petrothermal systems	12
2.2 Current development status	13
2.2.1 Worldwide perspective	13
2.2.2 Geothermal energy in Switzerland	14
2.3 Required steps to boost the development of geothermal energy	15
2.4 State of the art in the drilling technology	18
2.4.1 Drill bits for mechanical drilling	19
2.4.2 Main components of a drilling system	20
2.4.3 Completion: casing and cementing	22
2.4.4 Differences between drilling for hydrocarbons and geothermal purposes	23
2.5 Thermal spallation drilling - a novel drilling technology .	24
2.5.1 Mechanisms of the technology	24
2.5.2 Known benefits of the technology	26
2.5.3 Technical operating principles of thermal spallation drill heads	26
2.5.4 Historical development and current status	28
2.5.5 Open questions	29
2.6 Conclusions of this chapter	30

3	Experimental setups and methods	31
3.1	The universal small scale setup (s-ASDP)	32
3.1.1	Air configuration	32
3.1.2	Oxygen configuration	34
3.2	Central Aare granite, the reference rock material	35
3.3	Heat flux measurement techniques	38
3.3.1	Heat flux sensors based on the thermopile principle and their calibration	38
3.3.2	Non-intrusive heat flux measurement technique	40
3.4	Conclusion of this chapter	51
4	A comprehensive model for thermal spallation drilling	53
4.1	Preliminary study: experimentally derived operating conditions	57
4.1.1	Minimal required boundary conditions	57
4.1.2	Complete operating curve	65
4.1.3	Conclusions	69
4.2	Theory on the spallability of rocks	69
4.2.1	Principles of the model	71
4.2.2	Derivation of the spalling criterion	71
4.2.3	Sensitivity analysis and characteristics of the derived spallation criterion	78
4.2.4	Validation with Central Aare granite	81
4.2.5	Rock spallability criterion	84
4.2.6	Conclusions	85
4.3	Model for the maximum drilling velocity	86
4.3.1	Quasi-steady state model	87
4.3.2	Implementation of the spallation limits	90
4.3.3	Validation with experimental data	92
4.3.4	Design of spallation drill bits	93
4.4	Conclusions of this chapter	98
5	Thermal spallation drilling in deep drilling operations	99
5.1	Cost assessment of thermal spallation drilling	100
5.1.1	The cost model	101
5.1.2	Assessment of the optimal ROP	102
5.1.3	Case study with the derived cost model	104

5.1.4	Conclusions	110
5.2	Drilling at great depths	110
5.2.1	Non-spallable rocks	110
5.2.2	Stress relieving fractures	112
5.2.3	Significant intrusion of fluids	114
5.3	Supply of the reactive fluids	116
5.3.1	Transport via drill string or coiled tubing	117
5.3.2	Storage in the BHA	118
5.4	Conclusions of this chapter	119
6	The hybrid drilling project	121
6.1	Combined drilling process	122
6.2	Thermal rock weakening	125
6.2.1	Preliminary experiments	125
6.2.2	Strength analysis	128
6.2.3	Footprint in the thermal properties	131
6.3	Air shield protection	133
6.3.1	Experimental setup and procedure	134
6.3.2	Experimental results	135
6.4	First conclusions	138
6.5	Field test in cooperation with GZB Bochum	138
6.5.1	Design of the system	140
6.5.2	Test of the flame system in the lab	145
6.6	Conclusions of this chapter	148
7	Thermal bore hole enlargement	149
7.1	Thermal bore hole enlargement	151
7.2	Field test in the Grimsel Test Site	153
7.2.1	The experimental setup	154
7.2.2	Experimental procedure	157
7.2.3	Results of the field test	159
7.3	Conclusions	163
8	Conclusions & outlook	165
8.1	Conclusions	166
8.2	Outlook for future work	168

A	Appendix	171
A	Complete describtion of the matrix structure	172
B	Physical properties of the spallability map	177
C	Cost tables of the case study	178
D	Technical drawing of the hybrid head	182
Bibliography		183
List of publications		206
Curriculum Vitae		211

Nomenclature

Abbreviations

AFL	Air to fuel ratio
ASDP	Ambient spallation drilling plant
BHA	Bottom hole assembly
EGS	Engineered geothermal system
FP	Failure plane
HDR	Hot dry rock
PDC	Polycrystalline diamond compact
LWD	Logging while drilling
MWD	Measuring while drilling
ROP	Rate of penetration
SOD	Standoff distance
SP	Spallability
UCS	uniaxial compressive strength
WOB	Weight on bit

Roman symbols

A	Area [m^2]
a	Crack length [m]
a	Edge length of an element in y-direction [m]
b	Edge length of an element in z-direction [m]
Bi	Biot-number [-]
C	Costs [USD]
c_p	Specific heat capacity [$J/(kg\ K)$]
D, d	Nozzle diameter [m]
dt	time step [s]
E	Young's modulus [Pa]
f	General function

I	Current [A]
i, j	Local element number in y- and z-direction $[-]$
H	Distance nozzle - surface [m]
h	Enthalpy [J/kg]
h	Heat transfer coefficient [$W/(m^2 \cdot K)$]
J	Number of temperature observers in a specific direction $[-]$
K	Number of heat flux elements in a specific direction $[-]$
K	Stress intensity factor [$Pa \sqrt{m}$]
L, l	Length [m]
M	Magnitude on the Richter scale $[-]$
\dot{m}	Mass flow [kg/h]
n	Total number of time steps $[-]$
P	Power [W]
p	Pressure [Pa]
q	Heat flux [W/m^2]
r	Time step of current evaluation $[-]$
S	Domain [m]
S	Sensitivity [$V/(W/m^2)$]
Sp	Spallability number $[-]$
s, a	Local element vectors [m]
T	Temperature [$^{\circ}C$]
t	Time [s]
U	Voltage [V]
u	Velocity [m/s] or [m/h]
\dot{V}	Volume flow rate [m^3/h]
v	Response to a unity step [$^{\circ}C$]
X	Sensitivity [$K m^2/W$]
x, y, z	Directions [m]
z	Distance from the surface [m]

Greek letters

α	Linear thermal expansion coefficient [K^{-1}]
α	Surface absorption [-]
Δ	Difference
Δx	Particle size [μm]
ε	Emissivity [-]
ϵ	Strain component [-]
η	dynamic viscosity [$kg/(m \cdot s)$]
Θ, ϑ	Temperature difference [K]
κ	Thermal diffusivity [m^2/s]
λ	Thermal conductivity [$W/(m \cdot K)$]
λ	Wavelength [μm]
ν	Poisson's ratio [-]
ν	kinematic viscosity [m^2/s]
ξ	Dimensionless distance [-]
ρ	Density [kg/m^3]
σ	Stress vector [Pa]
τ	Dimensionless time [-]
Φ	Angle [$^\circ$]
φ	Air to fuel ratio [-]

Sub- and superscripts

1	Orthogonally to the surface
1	Principle stress direction
<i>I</i>	Referring to mode I cracking
2	Parallel to the surface
<i>C</i>	Critical
<i>f</i>	Fixed
<i>fl</i>	Referring to the fluid or the flame
<i>fuel</i>	Referring to the fuel

i, o	Initial Conditions
i, j	Element location number in y- and z-direction
T	Referring to the time
K	Referring to the crack
M	Referring to the melting temperature
oxy	Referring to the oxidizer
q	Referring to a heat flux element
r	Arbitrary time step
$rock$	Referring to the rock
s	Surface
$sens$	Referring to the sensor
$spec$	Specific
T	Referring to temperature
t	Thermal, time
v	Variable, evaporation
xx	Normal to the x-axis
yy	Normal to the y-axis
zz	Normal to the z-axis

Dimensionless numbers

$Pr = c_p \eta / \lambda$	Prandtl number
$Nu = h D / \lambda$	Nusselt number
$Re = u D / \nu$	Reynolds number

CHAPTER 1

Introduction and motivation

In order to give a general overview over the contents of the present thesis, the motivation and objectives are briefly discussed in this chapter. Additionally, the single chapters of this thesis are introduced and their main statements are discussed.

1.1 Motivation

The production of electricity from deep geothermal resources requires substantial financial investments. In particular, the establishment of the required deep wells and the creation of the downhole heat exchanger are cost intensive project steps during the construction of a geothermal power plant. Long wells have to be drilled in hard, abrasive rock formations. The state of the art technology can drill these formations only with low penetration rates and under substantially wear of the mechanical cutters, leading to unacceptable high costs. Additionally, the creation of the underground heat exchanger, by means of a large fracture network, with hydraulic stimulations implies certain difficulties: near well bore impedances and insufficient access to preexisting natural fractures can inhibit the stimulation process. Additionally, during hydraulic stimulation, major seismic events (earthquakes) can be triggered.

Therefore, in order to boost the development of deep geothermal energy, different technologies are currently investigated by researchers around the world, with the aim to reduce the specific well costs (USD/MWh) and to enhance the creation of the underground fracture network. One of these technologies is thermal spallation drilling, which uses a hot fluid jet to thermally excavate the rock. Even though, thermal spallation drilling has been used for decades for hard rock excavation, no deep bore hole has been drilled with the technology, as some important questions remain still open. The motivation of this thesis is to answer these questions, discuss the viability of thermal spallation drilling and to derive application possibilities of the technology, where it can contribute to the development of deep geothermal energy production.

1.2 Objectives

In order to derive potential application fields of thermal spallation drilling and to enable a viability assessment of the technology, several aspects of the process have to be investigated. First, a deeper understanding of the physics of this technology is required. The influence of the rock properties on the process have to be investigated and understood. Further, the operating window of the flame jet system, which can be applied to drill a certain rock formation, has to be known. There, the process parameters, which lead to an optimized drilling velocity, play a key role.

With the fundamental physics of the technology known, the potential limitations of the technology in real drilling applications can be evaluated. A cost study would indicate the financial viability of the technology. Besides the significant influence of the rock properties on the drilling performance, what are other effects appearing in natural rock formations which could put a potential limit to the process? The present thesis aims at discussing the differences between experiments in laboratory and field environments and their consequences for thermal spallation drilling. Only if these differences are known, a comprehensive and objective evaluation of the potential of spallation drilling for deep drilling processes is possible, application possibilities for geothermal heat mining can be derived and necessary steps towards a commercial application can be identified. Finally, this thesis will show the operational readiness and the potential impact of thermal spallation drilling in two field tests.

1.3 Overview over the thesis

The present thesis consists of nine main chapters (see Fig. 1.1). After this introduction, which gives a brief overview over the thesis and its contents, deep geothermal energy and thermal spallation drilling are introduced (Chapter 2). Thereafter, some important experimental setups and methods used throughout the thesis are discussed. Additionally, Central Aare Granite is introduced as the reference rock material of this report (Chapter 3).

In Chapter 4, a model for thermal spallation drilling is introduced, assessing the physics of the process. The model consists of two submodels. The first submodel can be used to determine the required operating conditions to initiate thermal spallation drilling on a certain rock formation. The second submodel estimates the drilling velocity through various rock formations under certain flame operating conditions. Additionally, the model can be used to derive design guidelines for thermal spallation drilling tools and to perform a cost-benefit analysis.

After the introduction of the model, the opportunities and challenges for the implementation of spallation drilling in deep drilling operations are discussed (Chapter 5). A cost study evaluates the competitiveness of thermal spallation drilling in comparison with conventional drilling techniques. Additionally, the chapter highlights the differences between laboratory experiments and drilling operations in a real bore hole. The chapter closes with recommendations where spallation drilling can be used and which limitations restrict the application of this technology.

Thereafter, the so far linear structure of the thesis finishes and the laboratory environment is left. In Chapter 6, the preparation for a field test, combining thermal spallation drilling with conventional drilling techniques on a 40 ton drill rig is, discussed. This hybrid drilling technique solves most of the problems discussed in Chapter 5.

In Chapter 7, a field test conducted in the Grimsel Test Site is presented, which shows the applicability of thermal spallation drilling to enhance and enlarge the production section of a geothermal well, reducing costs and stimulation efforts. The field test was conducted with a 25m long thermal spallation drilling setup, excavating in a water-filled borehole. These two chapters present the application possibilities of thermal spalla-

tion drilling and show the operational readiness, which could be achieved during the progression of this dissertation.

Finally, the thesis ends with some conclusions, which could be drawn during the research on this technology and with suggestions how the technology can be further developed and eventually used in deep drilling operations.

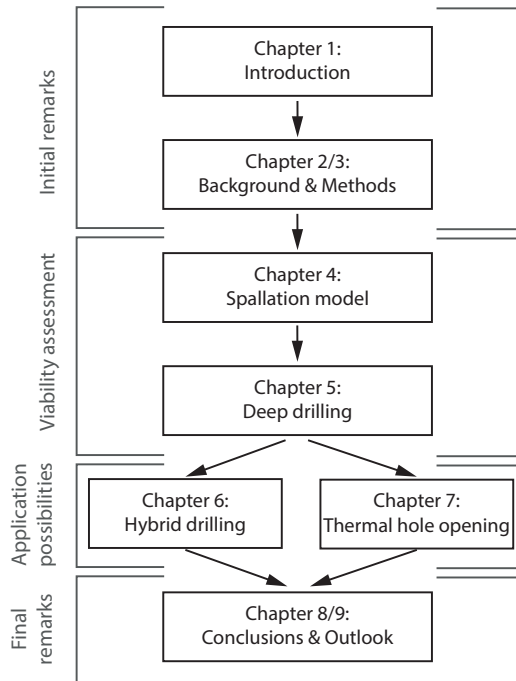


Figure 1.1: Structure and brief overview over the thesis

CHAPTER 2

Background: geothermal energy
and thermal spallation drilling

The energy sources oil, coal, gas and uranium form today, with about 75% of the total produced electricity worldwide [1], the basis of mankind's energy supply. Due to the limited availability of these resources in the future and the climate change triggered by the extensive CO₂ release during the combustion of hydrocarbons, alternative ways to satisfy the world's energy demand have to be found. One currently pursued solution are renewable energy sources, which release far less CO₂ and are basically available in unlimited amount. The future use of nuclear energy is currently not considered by many countries, due to difficulties in long-term storage of the produced waste and safety concerns, as *i.a.* in Fukushima. The most important and common renewable energy sources are wind, solar power, geothermal energy, hydro power and energy production from bio-products.

Since the late 90's of the last century, extensive efforts have been conducted by various countries around the world to migrate from a hydrocarbon based energy supply towards a sustainable electricity system based on renewable energy sources. The focus in recent years has mainly been on the development of wind and solar power. In the absence of widespread grid interconnection on a continental scale, a problem of these mentioned energy sources is that no constant, base-load electricity can be produced, as the production is highly dependent on the constantly changing wind and solar radiation conditions. Additionally, an optimal use is limited to areas with high-wind loads (*e.g.* coastal areas or off-shore) or with high solar-loads (mainly between the northern and southern tropic). Solar and wind power is in many countries, and here Switzerland has to be especially mentioned, supported by already established hydro power stations, which were mostly built in the middle of the last century [2]. They form an important basis for base-load electricity by already facilitating large energy storage capacities. As their use is connected to a strong environmental impact [3] and most of the suitable locations for large dams are at least in Switzerland already exploited [4, 5], additional renewable energy resources, which can deliver base load electricity, are necessary to accomplish the pursued energy transition ("Energy Strategy 2050") [6].

One additional solution, which can deliver base-load electricity, is the energy supply from geothermal resources. Geothermal resources are thermal energy stored in the Earth, generated mainly from the radioactive

decay of minerals or originating from the planet's original formation [7–9]. These resources can be tapped and used for heat production (heat constitutes about 50% of the world's final energy consumption [10]) or electricity generation. Due to the constant heat provided in the underground, this energy can be used all year around at any times as required. In general, geothermal energy can be divided into shallow heat sources and deep geothermal systems (Fig. 2.1). Shallow and near-surface (a few 100m deep) systems, as *e.g.* geothermal heat pumps, can supply low temperature heat for industrial and domestic heating purposes and are an important contributor to Switzerland's energy strategy. Nevertheless, they do not provide the temperature level required for economical large scale electricity production with the technology of today. For this purpose deep geothermal systems with wells reaching depths of 3000-6000m are required [7, 8]. Although these systems have provided energy around the world for more than a century [7], the development of geothermal power stations for electricity production has mostly been limited to areas with readily accessible reservoirs, close to volcanic hot-spots, rift zones or islands-arcs as *e.g.* in Iceland, Italy, the East African Rift Zone or New Zealand.

In order to enhance the development of geothermal power in less economically viable regions of the world, cost-effective solutions to establish a geothermal power plant have to be found.

In this chapter, the major deep geothermal systems are introduced. Additionally, the current status worldwide and in Switzerland is assessed, together with the required steps to enhance the development of geothermal energy production. The currently used drilling technology is introduced, as the state of the art, and in the last section, the main technology of this thesis called thermal spallation drilling is discussed.

2.1 Deep geothermal systems - energy from the subsurface

In the following chapter, the principles of energy supply from geothermal systems are explained. Thereby, the discussion excludes surface-near (10-1000m deep) systems as *e.g.* geothermal heat pumps and focuses on deep geothermal systems (Fig. 2.1). Deep geothermal systems can be mainly divided into two systems: hydrothermal geothermal systems and petrothermal systems.

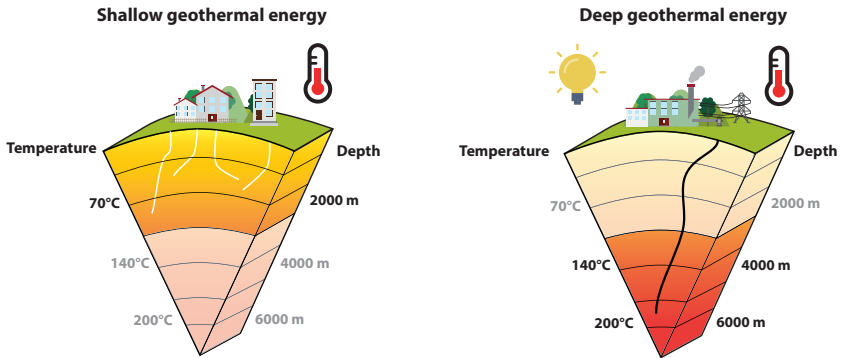


Figure 2.1: Illustration of shallow geothermal systems used mainly for heating purposes and deep geothermal systems for heating and electricity production.

2.1.1 Hydrothermal systems

Hydrothermal systems exploit hot water from deep (3-5 km), water-bearing formations, as *e.g.* hot aquifers, which transport a sufficient amount of water through permeable rock structures. Therefore, two wells are drilled in rock formations with a high permeability, which is usually further increased by hydraulic, thermal or acid stimulation [8]. These hot water reservoirs are tapped into and the water is transported through the production well up to the surface, where its energy is extracted by surface heat exchangers (see Fig. 2.2). The heat can be further transferred into electricity, if the energy level is high enough or used as process and residential heat supply. The cooled brine is afterwards

pumped down again through the injection well in order to maintain the pressure in the reservoir, extending the life time of the reservoir, and to return the usually highly mineralized water [8]. Hydrothermal systems are often part of large geothermal networks with several production and injection wells as *e.g.* the facilities in Iceland and in the region of Larderello, Italy [7, 8, 11].

However, prognosis and estimates of permeability and achievable flow rates of such a system are highly uncertain. Only drilling into the reservoir and hydraulic stimulation, which together require up to 70% [7, 8] of the total investment volume, will eventually decide, if the requirements for an economically interesting production are met. Several hydrothermal projects in Switzerland had to be stopped after the drilling process, due to insufficient production rates, as *e.g.* the Triemli project in the city of Zurich or the project in St. Gallen, where the latter yielded only 5 l/s instead of the targeted 50 l/s [8].

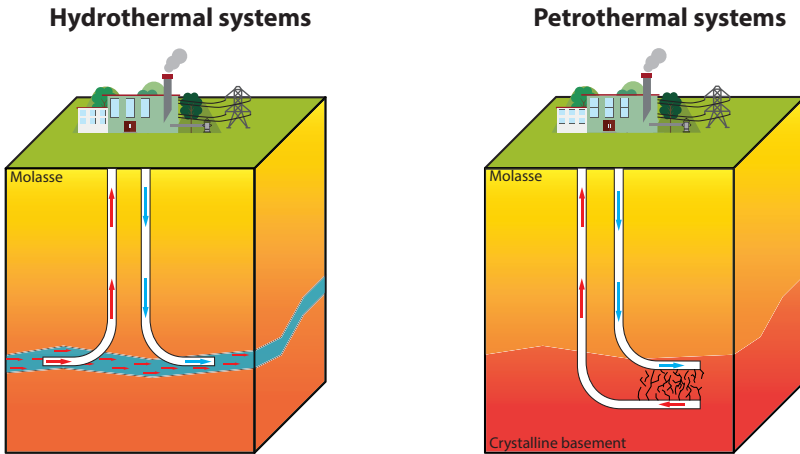


Figure 2.2: Illustration of the two main systems for deep geothermal energy production.

2.1.2 Petrothermal systems

If no economically viable flows of natural water are present, petrothermal systems are used to exploit heat from the subsurface. In these systems, wells are drilled into the crystalline basement to depths of 3-7km [8, 12]. As these formations are characterized by a high temperature, with no significant natural water flow and an artificial reservoir has to be created, this type of geothermal system is also called Engineered Geothermal Systems (EGS) or Hot Dry Rock (HDR).

At least two wells of these systems have to hit a fault zone or other geological zones, where the chances are high to find high temperatures and a large density of preexisting natural fractures. In order to achieve a certain permeability, these initially present fractures are stimulated with high water pressures until the fracture toughness is exceeded and fractures grow further into the formation [7, 8]. This hydraulic stimulation is continued in multiple steps until a network of fractures is created with a sufficient number of flow paths between the two wells, which can be used as a downhole heat exchanger [8]. Water is then injected into the injection well, circulated through the fracture network, where it is heated up and then pumped to surface via the production well. On surface, the hot water/steam can be used for electricity production or as process and district heat (see Fig. 2.2). The required hydraulic stimulation process is connected with induced seismicity. In the deep geothermal project in Basel, several seismic events, with a maximum magnitude of $M=3.4$ on the Richter scale were triggered, causing damage at houses and infrastructure in the city of Basel with a damage claim of 9 Mio. USD, eventually leading to the stop of the whole project [8, 13, 14].

Although petrothermal systems offer a huge potential and are not limited to areas with excellent prerequisites, only a limited amount of projects have been successfully accomplished as *e.g.* in Soultz-sous-Forêts, France [15]. The high unit well cost (USD/MWh) of the drilling process, due to the required long wells, the uncertain prediction of the flow-rates and the unsolved problem how to reduce and predict seismic events during the stimulation phase are currently limiting this technology.

2.2 Current development status

2.2.1 Worldwide perspective

Currently most of the heat from deep geothermal resources is generated in areas with good access to the heat, characterized by high thermal gradients, due to plate tectonic activities or local hot spots as Iceland, the St. Andreas fault in California, the Ring of Fire along Indonesia and Japan or the East African Rift system (see Fig. 2.3). Due to the close proximity of the heat source to the surface, shorter wells are required, which significantly reduces the costs, making more resources economically viable. The nations with the highest installed capacity of geothermal facilities are the United States, Indonesia, Philippines, Italy, New Zealand, Mexico and Iceland, which share together 77% of the worldwide produced geothermal power [16]. Thereby, the countries with the highest production rate per head are Iceland with 29%, El Salvador with 25%, Kenya with 20%, the Philippines with 15% and New Zealand with 14% [8].

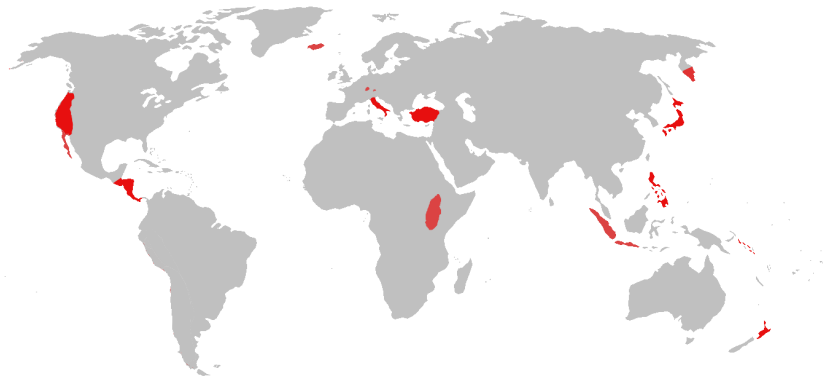


Figure 2.3: World map with areas of major geothermal exploitation highlighted.

2.2.2 Geothermal energy in Switzerland

Currently geothermal energy in Switzerland is mainly provided by underground heat pumps for district and industrial heating. Geothermal heat pumps delivered in 2013 a total heat of 2626 GWh, making Switzerland one of the world leaders in geothermal heat pumps utilization [17, 18]. Regarding deep geothermal systems, the situation in Switzerland is different. Only nine power plants are currently in service with a total installed power of 8.4 MWt, whereas only heat is produced and no electricity. This is significantly less than the installed power of the neighboring countries (Italy (1034 MWt), France (290 MWt), Germany (209 MWt), Austria (52 MWt)) [8]. The largest facility currently online is situated in Riehen (BS) with an installed capacity of 3.5 MWt. Hot brine with a temperature of 62°C and an average flow rate of 10l/s is produced from a 1547m deep production well, located in a fractured aquifer of the Upper Muschelkalk, and reinjected with a temperature of 25°C into the 1247 m deep reinjection well [19]. Certainly a drawback in the development of geothermal power in Switzerland was the cancellation of the two deep geothermal projects in Basel and St. Gallen. As discussed before, in Basel a major seismic event was triggered, damaging houses and infrastructure in the city. In St. Gallen insufficient flow rates together with a high natural gas inflow resulted in the termination of the project [8, 12]. Nevertheless, Switzerland's population has decided to further promote and pursue the development of electricity production from geothermal resources [20] and according to the Energy Strategy 2050 in the near future 4.4 TWh of the yearly energy consumption might be covered by geothermal resources [6], which is certainly a major challenge for the next decades. Currently three projects in Switzerland are under construction (two for heat and one for electricity production) and another nine projects are in planning [8]. The project closest to operation is currently planned in Haute-Sorne in the canton of Jura, with an electricity production of maximal 5 MWe [14]. In June 2015, the regional government approved the project plans and the start of construction is scheduled for 2018. In order to avoid induced seismicity, a multistage stimulation process is planned, which allows to control the fluid pressures and flow rates within the individual stages during hydraulic stimulation [14].

2.3 Required steps to boost the development of geothermal energy

As discussed above, electricity production from geothermal resources is still a not well established technology in Switzerland. The current use of geothermal power is mainly restricted to areas with good access to heat, which are mostly characterized by high thermal gradients, resulting in high temperatures directly below the surface. If zones with lower thermal gradients should be encountered, significantly deeper wells are required to be able to mine fluids with the desired temperatures. These deep geothermal projects are connected with high costs and a high risk of failure. A deep geothermal well costs 3-30 Mio. USD [7] and the general risk of a geothermal project to fail is around 25% [21], due to insufficient production flow rates, too low temperatures or induced seismicity with a high magnitude.

Fig. 2.4 illustrates how costs and risk are typically apportioned among the different steps of a geothermal project, from the planning phase until the final operation of the plant [22].

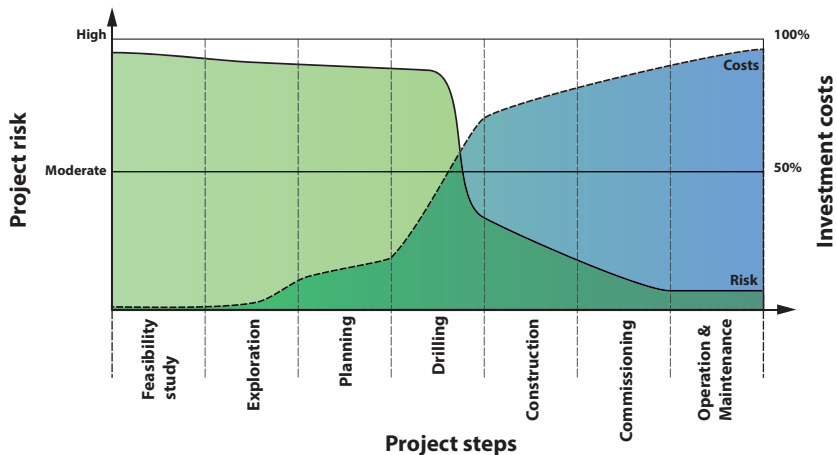


Figure 2.4: Involved costs and risk of the different project steps of a geothermal power plant, adapted from Gehringer *et al.* [22].

More than half of the total project costs will have been expended, when the risk of the project has decreased to a moderate level. This situation represents a development obstacle and financial hurdle, which has to be resolved in order to boost the development of geothermal energy production from deep resources [20]. The drilling process is a central step during the establishment of a geothermal power plant. During the drilling phase, up to 70% of the total costs have to be invested [7] and only after the well construction is finished, the risk of the project to fail drops considerably. Although forecasts are made in the planning phase of a geothermal well about the achievable temperature level and flow rates, only after completion and final stimulation of the well, the actual production conditions can be determined. Insufficient temperature levels and flow rates will lead to an uneconomical and inefficient prospect of the geothermal project, potentially leading to the abortion of the project. Additionally, in drilling processes near active tectonic zones, the risk to induced seismic events is considerably higher [23]. Drilling related activities or stimulation processes can trigger seismic events, which have the potential to cause damage to the drill site and the surroundings, as happened in Basel 2006 [14] and St. Gallen 2014 [24].

In conclusion, the currently prevailing high costs of the drilling process, connected with the also unfavorable risk assessment leads to a difficult situation for the development of geothermal systems. In order to overcome this problem and to increase the development of geothermal energy, two actions are possible: the risks have to be shifted away from the expensive project steps towards the beginning of the project, or the costs have to be moved away to low risk project steps (see Fig. 2.5). The first possibility can be tackled with an increased knowledge about the underground. Thereby, detailed information of the geology, the temperature gradients and permeabilities are required. Additionally, detailed models of heat and fluid flow in the underground are important. Starting with global models to enable an appropriate selection of the power plant location and finishing with models at a micro basis, describing the heat flow through engineered or natural fractures. Another important issue is that the risk of induced seismicity has to be reduced and suitably forecasted to gain acceptance in the local community beforehand.

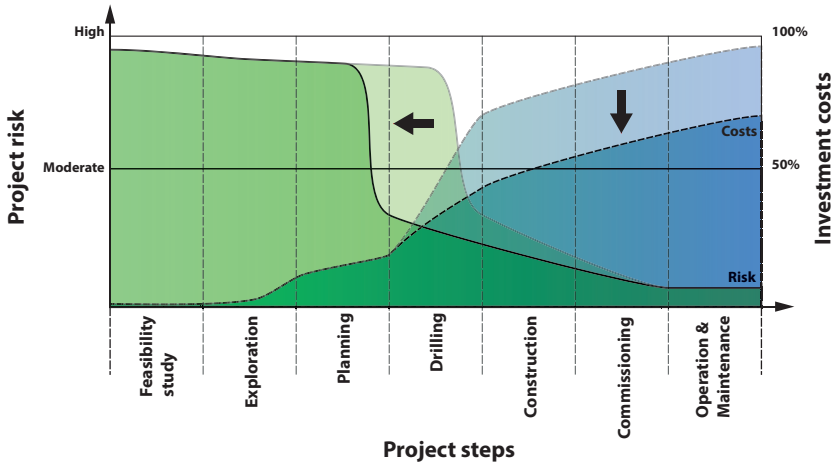


Figure 2.5: Required steps to increase the development of geothermal energy production, adapted from Gehringer *et al.* [22].

The second possibility discussed above, the reduction of the well unit cost, can be accomplished by developing appropriate tools for drilling in hard, abrasive rocks (*e.g.* Basalts, Granites). These tools could be new tools based on the conventional mechanical excavation of the rock or novel drilling technologies as *e.g.* thermal destruction of the rock material. To this end, researchers around the world are currently investigating different novel techniques. In order to develop methods to reduce the drilling costs, a fundamental understanding of the actual drilling technology is required. Therefore, in the next chapter, the conventional drilling technology is presented together with spallation drilling a novel drilling technology, which has the potential to reduce the drilling costs. Among the different attempts to intensify the drilling process, thermal spallation drilling is one of the most promising approaches. This technology uses a high heat flux from an impinging flame jet to destroy the rock surface [25, 26].

2.4 State of the art in the drilling technology

Drilling for geothermal resources is considerably adapted from drilling in the oil and gas industry. Nevertheless some important differences such as larger bore hole diameters, higher temperatures or different formations, distinguish the two drilling processes. In this chapter, the main principles of the state of the art will be shortly discussed. Thereby, only the most important components and steps of the drilling process are described. A more detailed description of the drilling process can be found in literature *e.g.* in the Standard Handbook for Petroleum and Natural Gas Engineering [27].

As wells are step-by-step cemented and equipped with steel casings to secure the well (see Chapter 2.4.3), the diameter of the bore hole has to decrease in sections from the surface to the bottom of the well. Fig. 2.6 shows such a section-wise design of a typical geothermal well. The specific design, diameter, number and length of the sections are thus depending on the prevailing rock formation and stress and temperature conditions, the target fluid and energy production rate and various other parameters [8].

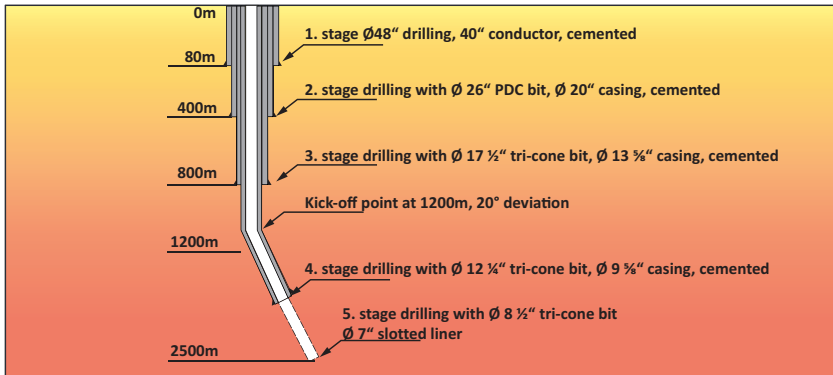


Figure 2.6: Example of the design for a medium sized geothermal well with a vertical depth of 2500m, 5 sections and a deviated layout. Drilling and casing parameters according to Polsky *et al.* [28].

2.4.1 Drill bits for mechanical drilling

The rock excavation process during conventional rotary drilling is performed by drill bits, which are in close contact to the rock at the bottom of the borehole. By rotating the drill bits under weight, the rock is comminuted by mechanical abrasion, shearing and crushing [29, 30]. Rotational speed, the torque and weight-on-bit (WOB) is transferred by metal drill pipes, which are connected up to surface, where the drill rig creates and controls rotation and axial movement of the drill string. Drill bits can be classified mainly in two major categories: roller-cone bits and polycrystalline-diamond-compact (PDC) drilling bits. The roller-cone bit (Fig. 2.7 (a)) crushes the rock with teeth-shaped tungsten carbide inserts, welded on usually three rotating roller cones [8].

Currently, the industry moves gradually away from roller-cone bits towards PDC drilling bits (Fig. 2.7 (b)). By 2004 the footage drilled by PDC bits has surpassed that of roller cone bits [31]. A PDC drill head consists of numerous PDC cutters, which are distributed over several fixed cutter blades. These cutters are extremely hard and destroy the rock mainly by shear. They outperform (higher rate of penetration, less torque and WOB) other drill bits in rather soft formations such as sandstones, clays and limestones [31]. With their fixed blade, they are less prone to fail and have a high bit life time [32, 33]. However, they underperform in hard, abrasive rock formations such as Granite or Basalt [34, 35]. Therefore, researchers around the world are working on solutions to enable the use of PDC cutters also in extremely hard and abrasive rocks. Here, work mainly focuses on new design features of the single PDC cutters, as *e.g.* conical shapes or rotating cutters, and on a combination of PDC cutters with other drill bits as *e.g.* with a roller cone bit.

Generally, for both drill bit types, a wide range of configurations is possible. With an appropriate design or selection of the drill bit, the performance of the drilling process can be optimized and costs can be reduced. Additionally, induced vibrations can be significantly damped, increasing the life time of the bit and other components of the drill string.



Figure 2.7: (a) Roller cone bits and (b) large-diameter PDC drill head, used at the geothermal site in Blanc-Mensil, France.

The two presented drill bits work well in soft and medium-hard formations. But in basement formations which will be encountered in deep geothermal projects, the efficiency of these drill heads will decrease rapidly, due to high wear-rates, caused by the high abrasivity of these rocks [36], leading to low rates of penetration and to high wear-rates of the drill bits. This causes extremely low average bit lives and thus a poor drilling performance and high cost. As an example, for drilling the injection well GPK3 in the EGS project in Soultz-sous-Forêts (France) in total 33 tricone bits were used with an average bit life of less than 50 hours [15]. On average, each bit drilled less than 200 m before it had to be replaced by a new bit [15]. The average rate of penetration was low with roughly 3.5 m/h [15]. When the cutters are worn-out, the drill string has to be tripped up to the surface and replaced by a new drill head. This is a time-consuming and therefore expensive step, which significantly decreases the cost-efficiency of the drilling project.

2.4.2 Main components of a drilling system

The components following after the drill bit form together with the drill bit the bottom hole assembly (BHA). Drill collars are installed, which are heavy items with a length of about 10m and a weight of 2-3.5 tons, providing the weight on the bit, which is required to efficiently drill the rock [30]. Additionally, stabilizers are integrated into the BHA, which are large-diameter, hollow, cylindrical bodies with stabilizing blades,

minimizing bit stability problems from vibrations and problems with the directional control during drilling [37]. In many BHAs a mud motor enables the bit to rotate with a higher rotational speed than the drill string. Additionally, the mud motor provides energy for directional drilling, measurements-while-drilling (MWD) and logging-while-drilling (LWD) tools.

The large distance (up to a few kilometers) between surface and the bottom hole assembly is covered by the drill string. It consists of numerous drill pipes which are standardized metal pipes with connection threads at both ends (see Fig. 2.8). On the inside, drilling fluid is pumped to the drill head. In order to save time, usually two (doublet) or three (triplet) drill pipes are already mounted and stored on surface at the drill rig and are then added to the existing drill string with advancing drilling progress.

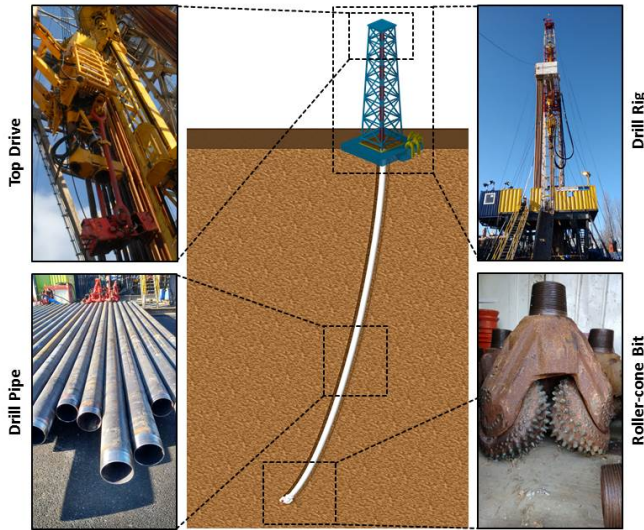


Figure 2.8: Illustration of a conventional drilling process with some main components highlighted

On surface, the drill rig controls the entire drilling process, supplies

the required materials and provides the required forces and motions (see Fig. 2.8) [38]. Also, lateral movement, weight on bit and rotational speed of the whole drill string are controlled by the top drive [27]. During the drilling process, drilling fluid is injected at the top drive and pumped down inside the drill string. After the drilling fluid exits the drill string at the front face of the drill head, it travels back through the annulus between formation and drill string. One of the main tasks of the drilling fluid is to transport cuttings from the bottom of the well to surface. On surface, the drilling fluid is usually recycled by separating the cuttings in different filter stages, as *e.g.* centrifuges and mud shakers. Other purposes of the drilling fluid are lubrication and cooling of the drill bits, suspension of particles, when the drilling process is paused, pressure control inside the well to avoid well collapse and formation fluid (*e.g.* combustible gases) from entering the well bore and transport of hydraulic energy for downhole-tools, *e.g.* mud-motors [29]. In order to fulfill all these task, the mostly oil- or water-based drilling fluids are complemented by various additives.

Besides the above-mentioned components, various other components are required for a successful drilling process, such as blow-out preventers, control systems or mud pumps. A complete description of these components and the drilling process in general can be found in literature [7, 29, 30, 39].

2.4.3 Completion: casing and cementing

In regular intervals, the well is secured with a steel casing. During casing operation, the drilling process is interrupted and the drilling equipment is removed from the bore hole. A steel pipe (casing) is lowered down into the bore hole and cement is pumped into the annulus between casing string and rock formation, creating a rigid connection between the two. The distance between the different casing sections depend on the rock formation and the integrity of the borehole. Once the casing and cementing process of a section is finished, the drilling process continues with a drill bit smaller in diameter than the steel casing to prevent damage to casing and bit. This leads to the characteristic shape of the well bore, starting from a large diameter at surface and as the well deepens, the diameter of the sections decreases (see Fig. 2.6) [40]. The casing

string protect the well from collapse. Additionally, in the shallow sections contamination of groundwater by drilling fluid or brine is prevented [40]. In the deeper sections, the casing isolates the well from abnormally pressured, fractured and lost circulation zones, providing well control during the drilling process [40]. At the end of the well, a perforated liner is generally installed, which allows the fluid from entering the well, while preventing loose rock material from blocking the flow.

2.4.4 Differences between drilling for hydrocarbons and geothermal purposes

In general, the drilling process for hydrocarbons and geothermal resources is based on the same suite of technologies. Thousands of wells are drilled every year by the oil and gas companies, in contrast to only a few wells drilled worldwide for geothermal purposes. Therefore, the oil and gas companies and the service industry are the driving force for further developments of the drilling technology. Generally, the unit cost (USD/MWh) for geothermal wells are considerably higher than for oil and gas purposes [7]. In the following, several major reasons for these high costs are listed, which also highlights the differences in the two drilling applications. For deep geothermal systems, long wells into the basement formation have to be drilled. These hard, abrasive rocks lead to high wear rates of the drill bits [29, 36, 41], resulting in low rates of penetration and short bit-life times. Typical geothermal wells have large completion diameters (7in. to 9-5/8 in.) to be able to accommodate the required flow rates of hot fluids [42]. These large production diameters lead to significantly larger diameters in all sections of the well [7, 29, 30], which increases the drilling costs significantly. Geothermal wells encounter higher temperatures than oil or gas wells. Therefore, special and expensive equipment, which can withstand these harsh conditions, is necessary.

In conclusion, the high costs of geothermal wells are mainly caused by the hard abrasive rock conditions, the required large diameters and required high-temperature equipment.

2.5 Thermal spallation drilling - a novel drilling technology

In order to boost geothermal energy production from deep resources, ways to decrease the drilling costs have to be found (compare Section 2.3). Besides the possibility to intensify current drilling technologies, new, alternative methods are currently investigated by researches around the world [25, 43–46]. One such alternative option are thermal drilling methods, where rock is comminuted by utilizing the thermal spallation effect.

In the following chapter, thermal spallation drilling is introduced. The principles of the process are explained, the benefits of the technology are discussed and technical operating principles of a spallation drill head are introduced. The chapter closes with a discussion of the remaining open questions, which have to be answered to assess the viability and application possibilities of this novel drilling technology. The deeper understanding of the physics of the spallation process and the transfer to practical applications is, however, an essential building block for the investigation of this technology.

2.5.1 Mechanisms of the technology¹

Thermal spallation drilling is based on the effect that certain brittle rocks will locally disintegrate into small fragments, if rapidly exposed to high thermal loads. Rapid heating produces high temperatures and high temperature gradients in the rock, which induce high thermal stresses in the upper layer of the rock. If these stresses exceed a certain threshold, surface cracks, initially present in the rock structure, are activated (Fig. 2.9). These cracks propagate through the solid and connect with other cracks until a rock fragment, so-called spall, is formed. Eventually, this spall detaches from the surface and expose a newly created rock surface, where the process continues [48–50]. In order to limit the crack growth to a localized zone and to prevent global cracking, which would lead to a relieve of the stresses, the rock, surrounding the immediate region that

¹This section is based on Kant et al., Journal of Geophysical Research: Solid Earth [47]

is being drilled, has to act as a confinement. This can be achieved by a sufficiently large compact rock mass or by additional, artificial or natural pressure components, acting on the rock. The spallation process takes place during a short time scale ($1 - 10ms$) and produces small particles ($50\mu m - 10mm$).

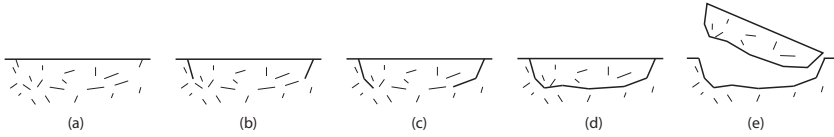


Figure 2.9: Principles of the spalling mechanism: (a) initial rock structure with micro-cracks, (b) crack propagation, (c) crack coalescence, (d) spall formation, (e) spall ejection

In order to facilitate the spallation process, a certain difference between the temperature, when the spall is formed, and the initial temperature is required. If this specific temperature difference, which is a function of the physical properties of the rock, is not exceeded, the generated thermal stresses are insufficient to induce thermal cracking of the rock surface. The efficiency of the process improves with increasing temperature and heat flux, as this induces a stronger temperature gradient, enhancing the thermal stress field in the upper layer of the rock. During spallation, the surface temperature has to be kept under the melting temperature of the rock, as melting prevents the spallation effect, due to weakening of the rock.

The spallation process has already been utilized for thermal, contactless drilling technologies, where hot fluid jets, laser beams, or plasma jets are used as the required heat source [25, 43–46]. Hence, the use of flames seems to be the most appropriate option. Flames provide an easy controllable system, which can be maintained under various operating conditions, *e.g.* in an aqueous, high-pressure environment [25, 51, 52]. Additionally, the required reactants can be easily transported from surface to the drill head or stored in the BHA.

2.5.2 Known benefits of the technology²

During thermal spallation drilling, the flame nozzle is adjusted to a certain distance from the rock, keeping the contact between rock and drill head at a minimum. Therewith, the technology has the potential to feature low wear rates [53, 54], leading to high operating times of the individual heads, followed by reduced tripping efforts [7, 55]. High rates of penetration (ROP) of about 15 m/h have been reported for granitic rock, crystalline sandstone and quartzite [56]. Conventional rotary drilling is characterized by poor energy transfer, due to significant drag and torque losses along the drill string [57]. Thermal spallation drilling could potentially enhance the energy transfer, as most of the energy is transferred as fuel inside the drill string or stored in the bottom hole assembly, where fewer losses are encountered. Therefore, less torque and weight on bit might be required, increasing the overall efficiency of the process. Generally, thermal spallation drilling has shown its applicability for drilling shallow holes in hard rock formations with depths up to 311 m and ROPs of 15 m/h [58]. In order to extend the application to deep wells, the gaseous flame has to be sustained in the high density setting of the liquid drilling fluid at high pressures. In this environment, entrainment of dense drilling fluid into the low-density flame jet can lead to significant heat losses before the energy can be transferred to the rock [51, 59]. Additionally, by using thermal spallation drilling, it is difficult to control shape and trajectory of the bore hole, due to local variation of the ability of the formation to spall [47]. A broader discussion of the limitations of the technology and possible solutions can be found in Chapter 5 of this thesis.

2.5.3 Technical operating principles of thermal spallation drill heads³

In this section, general technical design principles of thermal spallation drill heads for deep drilling processes are reported. In general, the reactants used to provide the required heat can be gases or liquids. In the past, mostly methane or ethanol in combination with air or oxygen

²This section is based on Kant et al., OIL GAS European Magazine [25]

³This section is based on Kant et al., OIL GAS European Magazine [25]

have been used at the Institute of Process Engineering of ETH Zurich [51, 60]. Three possibilities to supply these reactants to the drill head are conceivable in general: transport of the fluids via dual or triple drill strings [61, 62] from the top drive to the drill head, storage in tanks integrated in the BHA or downhole electrolysis of oxyhydrogen from the drill mud. The geometry of a thermal spallation drill head is optimized to transfer a maximum of heat onto the rock surface, as well as to expose the entire area below the head to the heat (Fig. 2.10) [25].

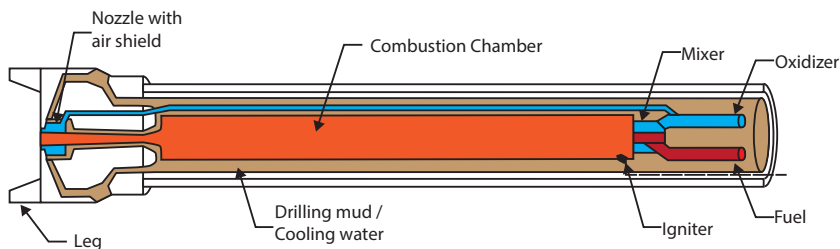


Figure 2.10: Typical drill head used for thermal spallation drilling at ETH Zurich

Reactive fluids are mixed and afterwards pumped into a combustion chamber, where a mechanism ignites and monitors the flame. For this purpose, heat wires [52], sparks [60] or glow plugs [63] were successfully utilized at the Institute of Process Engineering. The created combustion gases are accelerated through a nozzle, before they impinge on the rock surface. Circulation of drilling mud keeps the parts at an acceptable operating temperature and flushes away the produced particles. Recent research showed that the drilling mud must be removed from the combustion zone and injected above the head to guarantee an effective heat transfer process. If this is not possible, a protection of the combustion jet by an air shield reduces entrainment and increases the treatment zone (see Fig. 2.10 and Section 6.3). As the distance from the outlet of the combustion chamber to the rock surface determines the heat transfer capacity, cooled or uncooled legs are used to guarantee an optimal and fixed distance. At the same time, they promote a safer use of the drill, preventing blocking of the nozzles.

2.5.4 Historical development and current status

Spalling of rocks was for the first time scientifically investigated by Preston and White [48] in the 1930s, who found out that the brittle failure during spallation cannot be only described by exceeding the compressive strength of the material, but that also preexisting cracks contribute to the rock failure. Shortly after the research of Preston and White, the technology was firstly commercially used by the Linde Air Products Division of Union Carbide, which built in total 42 spallation rigs to create blast holes in quarries [41, 56, 64, 65]. The drill heads were operated with a mixture of gasoline and oxygen combusted in a water cooled combustion chamber. The hot combustion gases were accelerated through multiple laval nozzles, which yielded super-sonic jets, impinging on the rock surface [41]. In order to guarantee an equal distribution of the heat and a circular borehole, the drill head was rotating at about 25 RPM [41]. This concept was economically advantageous over other techniques available at that time and was successfully applied in various quarries in the United States.

In 1966 a second company called Browning Engineering Inc. started to sell spallation drilling equipment [41, 58, 65]. Their system used gasoline and air, which were also combusted in a jet-like water-cooled combustion chamber and then accelerated through a single non-rotating nozzle [58, 66]. Browning's system focused on blast holes in quarries, but they also performed two experiments to investigate spallation drilling as a technology for deep wells. Wells, 311m and 130m deep, were drilled with an average ROP of 16m/h and 7m/h, showing the feasibility to use the spallation technology for well drilling applications [41, 64, 65]. However, they also found the first major limitation of the process, when used in deep drilling projects: when a certain depth was reached, the flow of combustion gases alone was insufficient to transport the rock cuttings to surface [41] and if larger discontinuities in the rock were present (*e.g.* fractures) no continuous spalling of the rock was possible [58]. Both companies stopped their activities in the 1980s, as the cost for fuel were increasing and mechanical drilling technologies improved, making the spallation technology economically unviable [41, 63, 64].

As fuel prices dropped again in the 90's, attempts were made to overcome the problem that the maximum well depth is limited by the low

capability of the combustion gases to transport cuttings. Potter Drilling was one of the first companies to implement hydrothermal flame jets in order to use thermal spallation drilling for drilling deep geothermal wells [67, 68]. Hydrothermal flames can be operated in a supercritical aqueous environment and would therefore solve the problem of cutting transport. Potter Drilling was substantially supported in their development by Prof. Jefferson Tester, who focused his research on the hydrothermal flame drill head [54], the occurring boundary conditions [69] and models for spallation drilling [70, 71]. Potter Drilling developed a coiled tubing drill rig, where a mixture of peroxide, methanol and water was used for combustion [68] and successfully drilled in field tests until the company closed down in 2013, due to financial reasons.

In 2008 the Institute of Process Engineering at ETH Zurich started to apply their extensive experience of flames in supercritical water and high-pressure equipment for spallation drilling [72]. First spallation attempts were made in a small-sized high-pressure reactor [41, 73]. With the development of a new, large, high-pressure setup and a setup working under ambient condition the work on spallation was intensified [51, 63]. Progress was made in ignition of the flames without preheating of the reactants [52], the influence of the process parameters and confinement pressures on the rock [63].

2.5.5 Open questions

As discussed above, thermal spallation drilling has been investigated for decades and many problems have been overcome [52, 74, 75]. Nevertheless, up to now the technology has not been applied in any deep drilling project, as some important questions still remain open: the operating range, where the process can be used, is unknown. Which rock properties are favorable for spallation drilling and which are not? If a rock can be spalled, what are the minimal and maximal possible flame operating conditions and which process parameters will lead to an optimized and efficient drilling process? Additionally, the maximum drilling velocity reached with spallation is an important factor, as it directly relates to the required financial efforts. Therefore, a model is required, which can be easily used to estimate the required operating conditions and the drilling velocity. If an average drilling velocity for a specific well can be

predicted, a cost evaluation of the technology is possible.

Furthermore, the potential limitations of the technology for real drilling applications are still not completely evaluated. Besides the significant influence of the rock properties on the drilling performance, what are other features of natural rock formations, which might limit the process? Only when these aspects are known and understood, one may be able to perform a comprehensive evaluation of the potential of spallation drilling for deep drilling processes.

This thesis aims to close these open questions by presenting a comprehensive model, evaluating the applicability of the technology and discussing possible applications for the technology in deep drilling projects.

2.6 Conclusions of this chapter

Geothermal energy from deep resources can significantly contribute towards a sustainable electricity production. However, its development is hampered by the substantial financial investment, required during the drilling phase, and by the high risk of project failure. In order to reduce these drilling costs, novel drilling techniques are investigated by researchers around the world. One such option is thermal spallation drilling, which is a contactless drilling technology using a hot fluid jet to induce high local thermal stresses. If a certain stress threshold is exceeded, the rock structure breaks and the rock is excavated. The technology features high drilling velocities together with low bit wear rates and has already been successfully applied in shallow drilling operation. Nevertheless, in order to use it in deep drilling operations, several scientific questions still have to be answered. The following chapters of this thesis aim at closing these open questions. A deeper understanding of the physics of the spallation process will be developed and the application possibilities and operational readiness of the technology will be shown in two large-scale field tests.

CHAPTER 3

Experimental setups and methods

In this chapter of the thesis some experimental setups and methods are presented, which have been used throughout the investigations presented in this thesis. Other setups or measurement techniques, which are used only once during the work, are discussed directly in the corresponding chapters.

3.1 The universal small scale setup (s-ASDP)

For an experimental investigation of thermal spallation drilling appropriate setups are required to induce the necessary surface temperatures and high heat transfer coefficients. Further, they need to allow for measurements of the observed effects, for good visual access and for high flexibility to adapt to different experimental procedures. Therefore, a multi-purpose experimental setup was established. This small ambient spallation drilling setup (s-ASDP) is used throughout the thesis for the experimental validation of the operating conditions, surface temperatures, heat transfer coefficients or later to investigate entrainment solutions. The setup was used in two different modifications, in an air and oxygen configuration. Both setups share the same platform, with a length of about 2m, height of 2.5m and a width of 1m. The burner systems and rock samples are placed inside a metal box to reduce disruptions from the surroundings and to protect the user from dislodged hot rock particles.

3.1.1 Air configuration

The s-ASDP in its initial configuration used air as oxidizer, keeping the rock's surface temperature at a low but sufficient level for spallation. The flame jet is created by a 10kW methane-air burner (Pharos E-354, Fig 3.1 (a) and Fig 3.1 (b) (1)), creating flame temperatures of about $T_{fl} = 1300^{\circ}C$. The flame impinges on the rock sample (2), which is placed at a certain standoff distance (SOD) from the nozzle of the burner. Air and methane are supplied by the in-house gas supply network respectively a methane bottle. For both supply lines, the pressure is regulated and monitored with pressure regulators and flame

arrestors, ensuring a safe operation of the setup. The flow rates of the fluids are controlled by two Bronkhorst EL-FLOW Select Series mass flow controllers (3).

The progression of the surface temperature of the rock samples during the spallation process is captured by two Optris OPTCTL3MH2CF2 pyrometers (4), which can measure temperatures from 200°C up to 1500°C with a sampling rate of 1000Hz at a wavelength of $\lambda = 2.3\mu\text{m}$. The focus spot of the pyrometers has a diameter of 1.5mm. With this high sampling rate and the small measuring spot it is possible to resolve the detachment of single spalls (see Chapter 4.1.1.4 for details). Additionally, a video camera (5) is installed, allowing later visualization of the experiments.

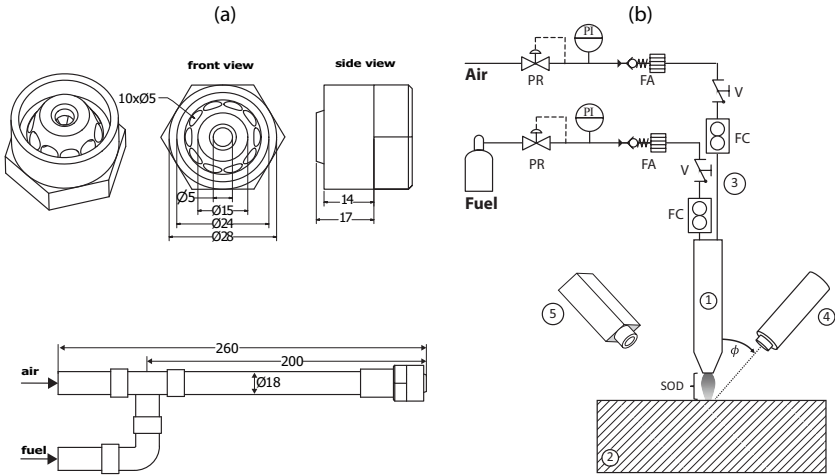


Figure 3.1: s-ASDP setup in its air configuration: (a) Schematic drawing of the nozzle with the most important dimensions in [mm]. (b) Illustration of the experimental setup and the supply network, (1) burner, (2) rock sample, (3) control and supply system, (4) infrared pyrometer, (5) camera. Symbols: PR - pressure reducer, FA - flame arrestor, V - valve, FC - flow controller.

3.1.2 Oxygen configuration

In order to further increase the applicable operating range of the system and to induce higher surface temperatures until melting of the rock occurs, the burner, mentioned above, was replaced by a new burner system (Arnold Group 141/1b ESL, Fig. 3.2 (a)), operating with methane and an adjustable oxygen-air mixture, creating a maximum combustion power of 20kW and flame temperatures of about $T_{fl} = 1800^{\circ}C$. The different fluid flows are mixed in a nozzle, which creates a stable flame-jet inside the combustion chamber. In this combustion chamber, the hot exhaust gas is accelerated through a nozzle and impinges on the rock surface. The burner system is ignited with a piezo-electric spark igniter. This configurations allows for use of the system submerged in water. The flow rates are controlled by flow controllers and the supply system mentioned above, with an additional supply line for the oxygen (Fig. 3.2 (b)). The same pyrometers and video camera, as for the air configuration, are installed.

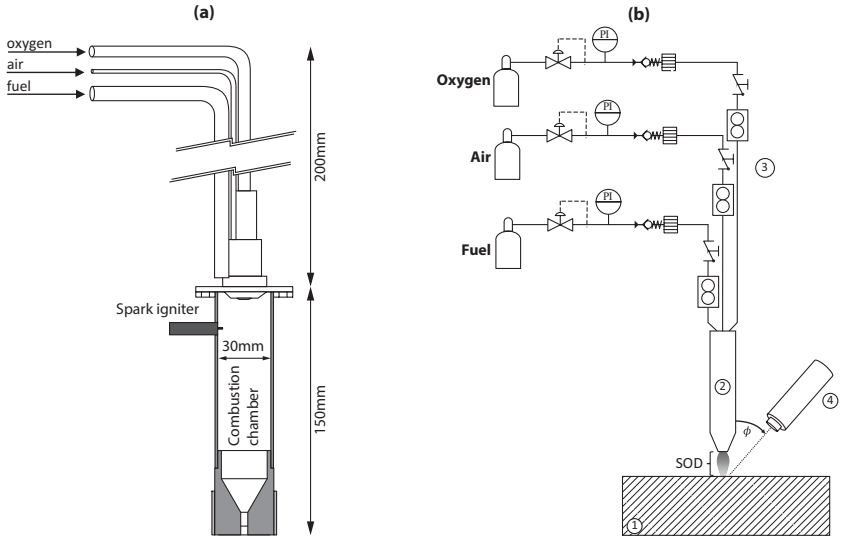


Figure 3.2: s-ASDP setup in its oxygen configuration: (a) Schematic drawing of the burner head, (b) Illustration of the experimental setup and the supply network, same labels and symbolic as in Figure 3.1.

3.2 Central Aare granite, the reference rock material¹

In order to allow a comparison between the different experiments conducted, evaluations and models, one rock type with a fixed sample size has been used as a reference material throughout this thesis. Central Aare granite was selected as a suitable material for this purpose. Spalling has been observed for this rock and due to the intensive research on this formation, the physical properties have been well document by other researchers (Table 3.1). All rock samples are taken from Chüenzentennlen close to the Grimsel Pass in the Swiss Alps and approximately 1km away from the entrance to the Grimsel Test Site (see Chapter 7), an underground laboratory. Additionally, the rock type is representative for the

¹This section is based on Kant et al., Geophysical Research Letters [76]

conditions encountered at great depths and can be easily accessed. Rock cores with a diameter of 85 mm and a length of 150 mm are selected. The rock material has a classical granitic composition with about 45% quartz, 30% K-Feldspar, 20% plagioclase, 3% biotite and minor amounts of other minerals. The rock is very heterogeneous and the grain sizes are highly variable, ranging from a few micrometers up to ca. 4 mm for feldspar, ca. 1 mm for plagioclase and biotite and ca. 0.9 mm for quartz (see Fig. 3.3 for a thin-section from the rock).

Table 3.1: Some physical properties of Central Aare granite; data obtained from literature; all values have been evaluated at room temperature; (A): [77–79], (B): [78–80], (C): [81], (D):[82],(E): [79, 83], (F) [76].

Physical properties	Values	Ref.
Young's modulus	$E = 30 - 40 \text{ GPa}$	(A)
Poisson's ratio	$\nu = 0.19 - 0.33$	(B)
Fracture toughness	$K_{IC} = 1.5 \text{ MPa m}^{0.5}$	(C)
Crack length	$a = 20 \text{ }\mu\text{m}$	(D)
Coeff. of thermal exp.	$\alpha = (7.8 - 8.2) \cdot 10^{-6} \text{ 1/K}$	(E)
Density	$\rho = 2550 \text{ kg/m}^3$	(F)
Thermal conductivity*	$\lambda = 3.25 \text{ W/(m K)}$	(F)
Heat capacity*	$c_p = 0.77 \text{ kJ/(kg K)}$	(F)
Thermal diffusivity*	$\kappa = 1.66 \text{ mm}^2/\text{s}$	(F)

*see Chapter 6.2.3

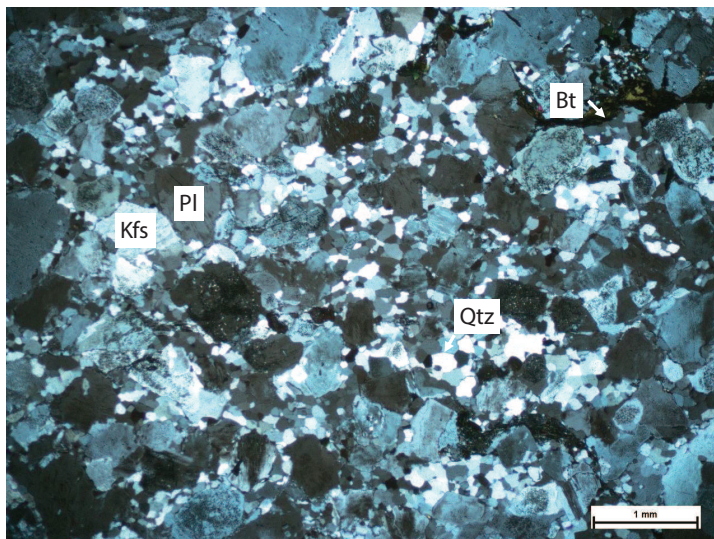


Figure 3.3: Thin-section of Central Aare granite. The rock is mainly composed of quartz (Qtz), K-feldspar (Kfs), plagioclase (Pl) and minor amounts of biotite (Bt).

3.3 Heat flux measurement techniques

The heat transfer coefficient, induced on the rock surface during the spallation process, is an important process parameter, as it is proportional to the drilling velocity and determines the required flame jet velocity [70]. Therefore, appropriate measuring tools are required, which capture the heat transfer process at the prevailing extreme conditions. As the heat transfer coefficient h_{fl} of the impinging flame jet cannot be directly measured, only an indirect measurement, by using Eq. (3.1), is possible,

$$h_{fl} = \frac{q_{sens}}{(T_{fl} - T_{s,sens})} \quad (3.1)$$

with the heat flux q_{sens} , the surface temperature $T_{s,sens}$ and the fluid temperature T_{fl} . Whereas the measurement of flame temperatures and surface temperatures is relatively simple, the determination of the heat flux at the prevailing conditions implies certain difficulties. Therefore, in the following, two different measurement techniques are presented, how the heat flux during thermal spallation can be measured.

3.3.1 Heat flux sensors based on the thermopile principle and their calibration

One option to measure heat flux is the utilization of commercially available heat flux sensors. In this thesis, a Wuntronic high-temperature heat flux sensor is used, which is based on the thermopile principle. A heat flux sensor has the advantages of robustness, availability and fast operational readiness. However, only single point evaluations are possible, *e.g.* in the stagnation point of the flame, and usually no spatial distribution can be resolved. Additionally, the sensor does not measure directly on the rock surface. Instead a transfer of the data from the sensor to the rock is required.

The thermopile sensor used consists of in-series connected thermocouples to amplify the output from a given temperature difference. The thermocouples measure the temperature differential across a thin layer and by applying a one-dimensional heat flux balance through this layer, the heat flux can be estimated from the voltage created by the thermocouples (see Fig. 3.4) [84, 85]. The heat flux sensor used in this thesis

is integrated in a housing, which is supplied with a water cooling circuit to regulate the surface temperature of the sensor.

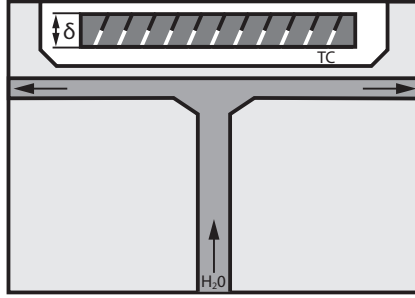


Figure 3.4: Illustration of the applied sensor measurement system, with a thermopile sensor embedded in a housing with water cooling.

During operation, the sensor generates a voltage U which is directly proportional to the heat flux $q_{sens} = U/S$, where S is the sensitivity of the sensor. As the applied sensor is only calibrated by the manufacturer for low temperature ranges, an additional convective calibration was accomplished, using a convection calibration setup [51, 86, 87] and a reference sensor (Vatell HFM-8E/H). The calibration of the applied sensor is accomplished by measuring the sensitivity S of the sensor for different surface temperatures $T_{s,sens}$. Thereby, the calibration procedure suggested by Meier *et al.* [87] was applied. The calibration of the sensor resulted in a constant sensitivity of $S = 0.404 \mu V/(W/m^{-2}) \pm 15\%$ for surface temperatures of the sensor in the range of $\vartheta_{s,sens} = 225^{\circ}C - 460^{\circ}C$. As no increasing or decreasing trend was visible over the investigated temperature range, the same sensitivity value was used for temperatures exceeding $460^{\circ}C$.

With the sensitivity of the heat flux sensor q_{sens} known, the heat transfer coefficient during the flame impingement studies h_{fl} can be calculated by Eq. (3.2).

$$h_{fl} = \frac{q_{sens}}{(T_{fl} - T_{s,sens})} = \frac{U}{S(T_{fl} - T_{s,sens})} \quad (3.2)$$

The surface temperature of the sensor $T_{s,sens}$ is determined using infrared pyrometers, as introduced in Chapter 3.1.1, and by coating the target with a reference paint (Pyromark 2500) with a known emissivity [88]. The flame temperature T_{fl} is measured with standard K-type thermocouples. For this purposes, thermocouples with three different diameters ($d = 0.5\text{ mm}$, 1.0 mm , 1.5 mm) were used and the results were prolonged for a thermocouple with zero diameter, in order to compensate errors, due to radiation and conduction along the thermocouple, as suggested by Pitts *et al.* [89].

The heat transfer coefficient on the surface of the rock samples and on the sensor surface can assumed to be identical, if the fluid-side conditions and the thermophysical properties of the impinging fluid in the boundary layer are similar. As the geometry of sensor plate and rock are similar and the same flow rates and SODs where adjusted, the fluid-side conditions of the two experiments can be considered as comparable. In order to avoid high differences in the physical properties between the two experiments, the sensor's surface temperature was kept similar to the values of the rock.

3.3.2 Non-intrusive heat flux measurement technique²

As the previously discussed measurement principles are based on a single-point evaluation of the heat flux and a transfer of the results from the sensor to the rock is required, a measurement technique is proposed, which can estimate spatially and temporally resolved heat flux distributions directly on the rock surface. The method estimates the heat flux by measuring the temperature distribution on the surface of the object with an infrared camera and by applying inverse techniques to transfer the temperature field to an in time and space highly resolved heat flux distribution. Thereby, heat conduction in all dimensions is considered and fast transient processes can be investigated. The method facilitates the use of inverse techniques in complex transient and multidimensional heat transfer problems.

²This section is based on Kant *et al.*, International Journal of Heat and Mass Transfer [60]

In the following sections, first, the principles of the method presented and the mathematical description are presented. Next, solving procedures are discussed and finally, the heat flux distribution of an aser beam, impinging on the front face of a metallic cylinder, will be experimentally determined. The applicability of the method is demonstrated, as the amount of heat absorbed by the body can be precisely calculated.

3.3.2.1 Principles of the method

The method is based on the measurement of an spartially and temporally resolved temperature field on the surface of an object. The heat flux distribution will then be estimated from this temperature field with the use of inverse techniques based on Duhamel's theorem (Fig. 3.5). Thus, the approach of solving inverse problems with two-dimensional sensitivity matrices, previously published by Beck [90], is expanded to a three-dimensional consideration. Therefore, the surface is discretized in heat flux elements and temperature observers. The required sensitivity values to solve the linear equation systems are calculated by utilizing a rectangular heat flux pulse on the surface of a semi-infinite body. In order to minimize the required computing time, a special solving algorithm is used, which reduces the required evaluation time significantly and allows the method to be used for online evaluations.

The required temperature field can be obtained with readings from an infrared camera, measurements with temperature sensitive paints or data from a thermocouple array integrated on the surface of the object. It has to be emphasized that none of these temperature measurement techniques are unproblematic and that they are affected by different error sources, which will lead to inaccurate heat flux estimates [91]. Additionally, temperature measurement always lag behind the real-time temperature distribution, which will distort the estimated heat flux distribution linearly to the magnitude of the time constant of the measuring device. In principle, the ability of the method to resolve heat transfer processes in space and time is not limited by the method but by the applied measurement principle itself.

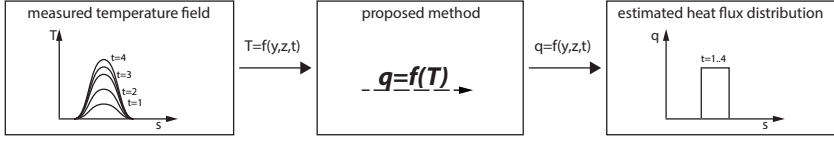


Figure 3.5: Illustration of the sequential sequence of the proposed evaluation procedure to estimate the heat flux distribution from a temperature field.

3.3.2.2 Mathematical formulation of the method

In order to apply this method, the surface of the object is discretized in space and time into a finite number of rectangular heat flux elements. Additionally, the surface is divided into an array of temperature observers, which represent the individual temperature readings from the required temperature field input.

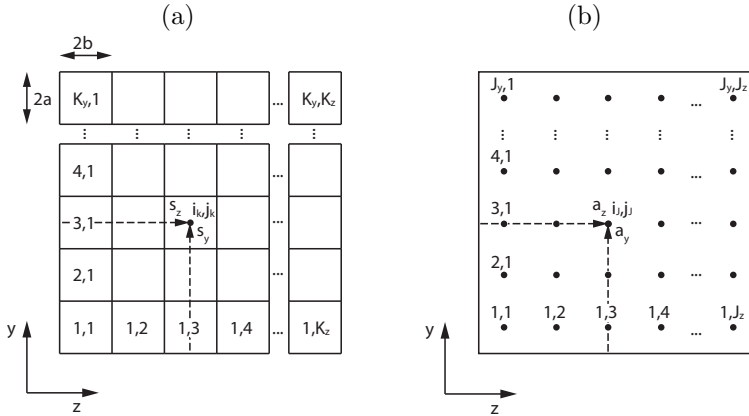


Figure 3.6: Discretization of the investigated surface in (a) $K_y \cdot K_z$ heat flux elements and (b) $J_y \cdot J_z$ temperature observers.

Fig. 3.6 (a) shows the discretization of the surface in total $K_y \cdot K_z$ heat flux elements, whereas K_y represents the number of elements in y -direction and K_z the number of elements in z -direction. Each element is rectangular shaped with edge lengths of $2 \cdot a$ and $2 \cdot b$. The local index of

a single element is defined as (i, j) , representing the local element numbers in y-direction and z-direction. The location of this local element is described by the vector $s = (s_y, s_z)$. A similar notation is defined for the temperature observer array (Fig. 3.6 (b)). Thereby, a temperature observer is always located in the middle of the associated heat flux element. In order to solve the inverse problem, the number of temperature observers has to be always greater or equal than the number of heat flux elements.

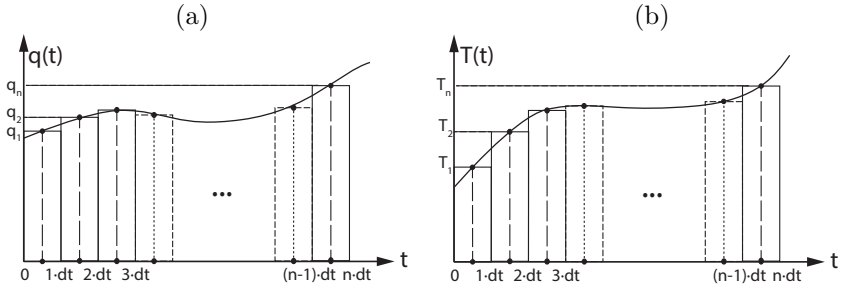


Figure 3.7: Discretization in time of (a) the rectangular heat flux pulses and (b) the temperature readings

Additionally, every heat flux element and every temperature reading is discretized in time in the manner shown in Fig. 3.7. The heat flux at times $t = 0.5 \cdot dt, 1.5 \cdot dt, \dots, (n - 0.5) \cdot dt$ are used to represent the heat fluxes between the associated times of $\Delta t = 0 - 1 \cdot dt, 1 \cdot dt - 2 \cdot dt, \dots, (n-1) \cdot dt - n \cdot dt$. The corresponding heat fluxes at the local element (i, j) for different time steps are denoted as $q_{i,j,1}, q_{i,j,2}, \dots, q_{i,j,n}$ and the temperatures similar as $T_{i,j,1}, T_{i,j,2}, \dots, T_{i,j,n}$. Concluding, the notation of a heat flux element at position i in y-direction and position j in z-direction at a specific time step r is defined as $q_{i,j,r}$. The associated observer at the same time step is similarly defined as $T_{i,j,r}$.

The proposed numerical technique is based on Duhamel's theorem. The derivation of this theorem can be widely found in literature [90, 92, 93]. It is based on the principle of superposition and connects the temperature linearly with the heat flux at any point in space and time. The theorem can be written as:

$$T = X \cdot q + T_0 \quad (3.3)$$

where \mathbf{T} is the temperature field, containing the temperature information for all observers at every time step, \mathbf{X} the so called sensitivity matrix, \mathbf{q} the heat flux values for all heat flux elements at every time step and \mathbf{T}_0 the temperature field at the initial conditions ($t < 0$). The sensitivity values inside the sensitivity matrix \mathbf{X} are defined as the first derivative of the temperature response v at a specific temperature observer location (i_T, j_T) and time t_T , with respect to a heat flux unit pulse at another specific location (i_q, j_q) and time t_q (Eq. (3.4)) [90].

$$X_{i_T, j_T, i_q, j_q} = \left. \frac{\partial v(i_T, j_T, t_T)}{\partial q(i_q, j_q, t_q)} \right|_{q=1 \text{ W/m}^2} \quad (3.4)$$

If Eq. (3.3) is solved for \mathbf{q} , the heat flux distribution can be estimated, if the temperature field, the initial conditions and the sensitivity matrix are known (Eq. (3.5)).

$$\mathbf{q} = \text{inv}(\mathbf{X}) \cdot (\mathbf{T} - \mathbf{T}_0) \quad (3.5)$$

Thereby, the heat flux vector \mathbf{q} , the sensitivity matrix \mathbf{X} and the temperature vector \mathbf{T} are multidimensional matrices, which contain the information of the quantities in space and time. A complete description of their internal structure and functionalities can be found in Appendix A or Kant *et al.* [60]. The multidimensional problem, which was formulated by Eq. (3.5), can be reduced to a 2D mathematical description by combining the time and space components of the individual matrices. Exemplary, the sensitivity matrix for this description is shown in Eq. (3.6), for a system with $K_y = 1$, $K_z = 2$ heat flux elements and observers and four time steps.

$$X = \begin{pmatrix} X_{1,1,1} & X_{1,2,1} & 0 & 0 & 0 & 0 & 0 & 0 \\ X_{1,2,1} & X_{1,1,1} & 0 & 0 & 0 & 0 & 0 & 0 \\ X_{1,1,2} & X_{1,2,2} & X_{1,1,1} & X_{1,2,1} & 0 & 0 & 0 & 0 \\ X_{1,2,2} & X_{1,1,2} & X_{1,2,1} & X_{1,1,1} & 0 & 0 & 0 & 0 \\ X_{1,1,3} & X_{1,2,3} & X_{1,1,2} & X_{1,2,2} & X_{1,1,1} & X_{1,2,1} & 0 & 0 \\ X_{1,2,3} & X_{1,1,3} & X_{1,2,2} & X_{1,1,2} & X_{1,2,1} & X_{1,1,1} & 0 & 0 \\ X_{1,1,4} & X_{1,2,4} & X_{1,1,3} & X_{1,2,3} & X_{1,1,2} & X_{1,2,2} & X_{1,1,1} & X_{1,2,1} \\ X_{1,2,4} & X_{1,1,4} & X_{1,2,3} & X_{1,1,3} & X_{1,2,2} & X_{1,1,2} & X_{1,2,1} & X_{1,1,1} \end{pmatrix} \quad (3.6)$$

3.3.2.3 Determination of the sensitivity coefficients

In order to determine the matrix described in Eq. (3.6), the sensitivity values of each element in the matrix have to be calculated according to Eq. (3.4). The required sensitivity values can be derived by for example using finite-element schemes or an algebraic function describing the temperature rise at a specific observer, due to a specific heat flux pulse at another position and time [90, 93]. In the present work the determination based on an algebraic function is chosen and a heat flux unit pulse of the size $\Delta y = -a..a$, $\Delta z = -b..b$, occurring at the time step of $\Delta t_q = (n - 1)\Delta t.. \Delta t$ and at the location number (i_q, j_q) is connected with a temperature observer at the location number (i_T, j_T) for times $t_T \geq t_q$. Thereby, the heat flux element and the temperature observer are located on the surface of a semi-infinite object with the dimensions $x > 0, -\infty < y < \infty, -\infty < z < \infty$. In order to derive the response function of such a unit pulse, first the temperature progression of a heat flux step located at the center of the coordinate system and occurring only on the surface of the described object for times $t \geq 0$ is derived (Fig. 3.8).

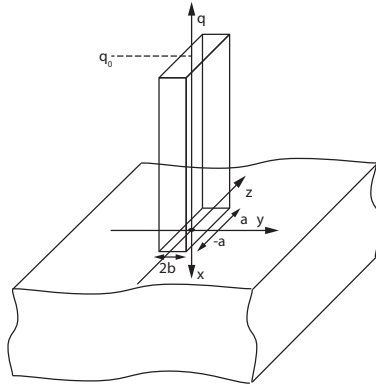


Figure 3.8: Illustration of the heat flux model, which is used to calculate the sensitivity values.

Thereafter, the resulting temperature progression is discretized according to the mesh definitions shown in Fig. 3.6 and Fig. 3.7. A com-

plete description of the derivation is left out and can be found in Kant *et al.* [94]. The resulting temperature distribution for the described heat flux unit pulse is shown in Eq. (3.7),

$$v_{step} = \int_{t'=0}^t \frac{q\kappa}{4\lambda(\pi\kappa(t-t'))^{1/2}} \left(\operatorname{erf}\left(\frac{a(1-|i_q-i_T|)}{\sqrt{4\kappa(t-t')}}\right) + \operatorname{erf}\left(\frac{a(1+|i_q-i_T|)}{\sqrt{4\kappa(t-t')}}\right) \right) \left(\operatorname{erf}\left(\frac{b(1-|j_q-j_T|)}{\sqrt{4\kappa(t-t')}}\right) + \operatorname{erf}\left(\frac{b(1+|j_q-j_T|)}{\sqrt{4\kappa(t-t')}}\right) \right) dt' \quad (3.7)$$

where q is the unit heat flux pulse, T_0 the initial temperature distribution, λ the thermal conductivity and κ the thermal diffusivity of the object. The integral in Eq. (3.7) can be calculated by using standard fast numerical integration tools as for example the adaptive Gauss-Kronrod quadrature. Finally, by applying the definition of sensitivity values described in Eq. (3.4) and using the superposition principle between two heat flux steps, one of size $q = 1 \text{ W/m}^2$ and time $t = 0..n\Delta t$ and the other one of size $q = -1 \text{ W/m}^2$ and time $t = 0..(n-1)\Delta t$, the sensitivity value for a local heat flux pulse can finally be stated as shown in Eq. (3.8).

$$X_{y_T, z_T, y_q, z_q} = v_{step}(t=n\Delta t) - v_{step}(t=(n-1)\Delta t) \quad (3.8)$$

This final equation for the sensitivity values is then integrated in the sensitivity matrix (Eq. (3.6)). Finally, the heat flux distribution is derived by inverting the theorem of Duhamel (Eq. (3.3)) and solving the inverse of the sensitivity matrix.

As stated above, the sensitivity values described by Eq. (3.8) are based on a semi-infinite body. The applicability of this assumption is possible for various heat transfer problems and has been discussed by different authors [84, 95, 96]. If temperature measurements on the surface of the object are not possible, the above derived equation for the sensitivity values can be easily adapted to temperature measurements in a certain distance from the surface. Thereby, it has to be mentioned, that stabilization procedures might be needed for a stable heat flux output.

3.3.2.4 Evaluation algorithm and solving possibilities

As the sensitivity matrices can easily reach sizes which are difficult to handle with standard computing equipment (e.g. $9 \cdot 10^6$ matrix-elements for 30x30 observers and 100 time steps), appropriate ways to store the matrix, handle it during the evaluation and to solve the linear equation system have to be found. As a complete solving of the matrix at once consumes considerable computing time, a so called blockwise-forward-substitution solving process is used: for the solution of the heat flux distribution at an arbitrary chosen time step r , the heat flux components $q_{i,j,1}, q_{i,j,2}, \dots, q_{i,j,r-1}$ are considered to be previously estimated and the heat flux components $q_{i,j,r+1}, q_{i,j,r+2}, \dots, q_{i,j,n}$ are considered to be zero, as they cannot effect the temperature at the actual time step r . Eq. (3.3) thus changes to the so called standard form of Duhamel's theorem (see Eq. (3.9)) [90],

$$\mathbf{T}_{J_y, J_z, r} = \mathbf{X}_{J_y, J_z, r} \cdot \mathbf{q}_{K_y, K_z, r} + \hat{\mathbf{T}}_{J_y, J_z, r-1}|_{q_{r-n}=0} + T_0 \quad (3.9)$$

where $\hat{\mathbf{T}}_{J_y, J_z, r-1}|_{q_{r-n}=0}$ can be considered as the temperature propagation at the time step r , due to the prior appearing heat flux components and when the heat flux components $q_{i,j,r} - q_{i,j,n}$ are set to zero. This residual temperature propagation can be calculated according to Eq. (3.10) [90].

$$\hat{\mathbf{T}}_{J_y, J_z, r-1}|_{q_{r-n}=0} = \sum_{s=0}^{(r-1)} \mathbf{q}_{J_y, J_z, s+1} \cdot \mathbf{X}_{J_y, J_z, r-s} \quad (3.10)$$

The blockwise-forward-substitution algorithm can be regarded as an blockwise solving procedure of the matrix, which solves the matrix for one time step by using all results from the previous time steps. As this solving method uses only the last row of the combined time and space sensitivity matrix (exemplary shown in Eq. (3.6)), only this data set has to be calculated and stored. This reduces the required memory and computing time significantly and online evaluations of the heat flux distribution are possible, if adequate mesh sizes and time steps are chosen and if the required maximal measurement time is known beforehand. To highlight the functionalities of the solver, the required sensitivity matrix

of an example with (1, 2) elements/observers and 4 time steps with the initial temperature field set to zero is shown in Eq. (3.11).

$$X_{bfs} = \begin{pmatrix} X_{1,1,4} & X_{1,2,4} & X_{1,1,3} & X_{1,2,3} & \cdots \\ X_{1,2,4} & X_{1,1,4} & X_{1,2,3} & X_{1,1,3} & \cdots \\ & \cdots & X_{1,1,2} & X_{1,2,2} & X_{1,1,1} & X_{1,2,1} \\ & \cdots & X_{1,2,2} & X_{1,1,2} & X_{1,2,1} & X_{1,1,1} \end{pmatrix} \quad (3.11)$$

By using Eq. (3.11) and the associated temperature vector, the heat flux distribution for the first time step of this example can be calculated as:

$$\begin{pmatrix} q_{1,1,1} \\ q_{1,2,1} \end{pmatrix} = \text{inv} \begin{pmatrix} X_{1,1,1} & X_{1,2,1} \\ X_{1,2,1} & X_{1,1,1} \end{pmatrix} \times \begin{pmatrix} T_{1,1,1} \\ T_{1,2,1} \end{pmatrix} \quad (3.12)$$

For the second time step, the estimated heat flux values can then be calculated according to Eq. (3.13).

$$\begin{pmatrix} q_{1,1,2} \\ q_{1,2,2} \end{pmatrix} = \text{inv} \begin{pmatrix} X_{1,1,1} & X_{1,2,1} \\ X_{1,2,1} & X_{1,1,1} \end{pmatrix} \times \left[\begin{pmatrix} T_{1,1,2} \\ T_{1,2,2} \end{pmatrix} - \begin{pmatrix} X_{1,1,2} & X_{1,2,2} \\ X_{1,2,2} & X_{1,1,2} \end{pmatrix} \times \begin{pmatrix} q_{1,1,1} \\ q_{1,2,1} \end{pmatrix} \right] \quad (3.13)$$

3.3.2.5 Experimental application of the method

In order to demonstrate the applicability of the evaluation procedure, an experimental study has been performed. A laser beam with the power of $P_{laser} = 1.35 \text{ W}$ and a beam diameter of $d_{beam} = 1.3 \text{ mm}$ impinges on the front face of a metallic cylinder (material: steel 1.4571, diameter $d = 80.15 \text{ mm}$, length: $l = 100 \text{ mm}$). The surface of the cylinder is coated with a high temperature paint (Pyromark 2500 [88]) with an absorbance of $\alpha = 0.91$ at the operating wavelength of the laser. The laser, which can be triggered with a mechanical shutter system, applies an idealized heat flux peak to the surface of the coated cylinder. The temperature field is measured with an infrared camera (Optris PI 450) with a resolution of 382x288 pixels, a maximal measuring frequency of 80Hz and an accuracy of $\pm 2\%$ or $\pm 2^\circ \text{C}$ (depending on the operating

range). In order to reduce the data, the information from 2x2 pixels was summarized for one temperature observer and the measuring area was restricted to the area of interest. The size of the single heat flux elements were set equal to the 2x2 pixels used for the temperature information. The recording time step was set to 0.37 s. Fig. 3.9 shows a cross section through the centerline of the applied measuring mesh, with the measured temperature field (a) and the estimated heat flux distributions (b) for all time steps.

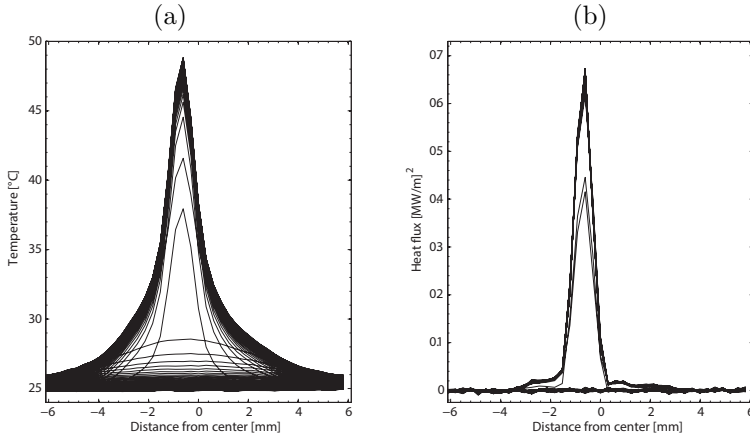


Figure 3.9: Cut through the centerline of (a) the measured temperature distribution and (b) the calculated heat flux distribution. All evaluated time steps are plotted. Parameters: $K_y = 40$, $K_z = 40$, $a = b = 1.53 \cdot 10^{-4} \text{ m}$, $n = 130$, $\Delta t = 0.37 \text{ s}$, $\kappa = 3.75 \cdot 10^{-6} \text{ m}^2/\text{s}$, $\lambda = 15 \text{ W}/(\text{m K})$

Due to radial conduction of heat along the surface, the shapes of the temperature and the heat flux distributions are considerably different. The method successfully reduces the wide temperature distribution to a much narrower heat flux distribution from the impinging laser beam. Fig. 3.10 shows the total power transferred through the surface, which was calculated by summation of all heat flux elements at a specific time step. The expected theoretical laser power can be calculated by multiplying the adjusted power of the laser beam P_{laser} with the absorbance of the surface α .

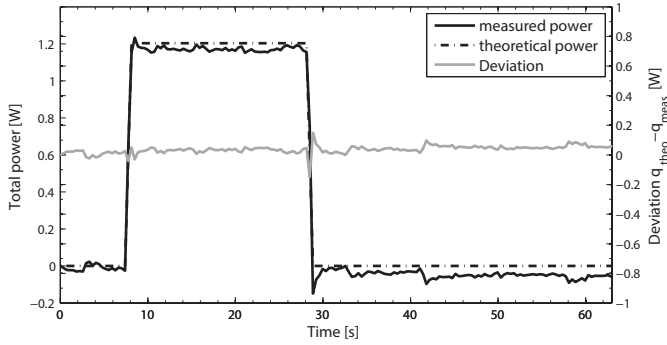


Figure 3.10: Total registered power calculated by summation of all heat flux elements. The same parameters as in Fig. 3.9 have been used.

It can be seen, that the estimated total power fits well with the theoretically expected value from the laser. Additionally, the rapid changes at the beginning and the end of the heat flux pulse are well reproduced with only minor overshooting visible and a slight increase of the deviation between theoretical power and measured power. Concluding, this experimental application shows that the method can be applied to actual heat transfer problems. The method accurately estimates the expected heat flux value and precisely reproduces the shape of the highly transient heat flux pulse.

3.3.2.6 Conclusions

An evaluation method is proposed, which can be used to determine transient heat flux distributions of diverse heat transfer problems. The required input parameter are temperature measurements over space and time on the surface of an object. Heat conduction in all space directions is considered, which enables the method to reproduce multidimensional heat flux distributions. Additionally, the method has a fast and stable response to rapid heat flux changes in time and space and shows a good stability towards fluctuations in the input signal. In principle the resolution possibilities of the method are only limited by the resolution of the temperature data. The method can be easily applied and used for versatile heat transfer problems, as all required equations are discussed and a

possible evaluation algorithm is presented. In order to show the application possibilities of the evaluation procedure, the method was applied to estimate the heat flux distribution of an impinging laser beam. Thereby, the results show good agreement with the theoretically expected values. The expected power of an applied rectangular heat flux signal could be accurately reproduced.

3.4 Conclusion of this chapter

In this chapter of the thesis, the main experimental setups and the reference rock material used for most of the following investigations were introduced. Additionally, two methods were discussed, how the heat transfer coefficient, a crucial parameter for an efficient use of the spallation technology, can be experimentally estimated.

CHAPTER 4

A comprehensive model for thermal spallation drilling

In order to assess the applicability and the economical feasibility of thermal spallation drilling without extensive full-scale experiments, a comprehensive analytical modeling approach is required. This model has to be capable to predict the required operating conditions of a thermal spallation drill head to drill a certain formation with a desired drilling velocity without any further calibration measurements. Only if such a model is available, an economical assessment of the technology, evaluating if thermal spallation drilling can reduce the drilling costs, is possible. Further, the design of spallation drill heads can be based on the physics of the process and not only on experimental observations.

Therefore, in the following chapter of this thesis, two interlinked models are presented. The first model is based on a fracture mechanical consideration and can be used to predict the operating conditions, which are required to drill a certain rock formation. Additionally, the model allows to map different rocks according to their ability to spall. The second model is based on an analytical heat transfer approach and estimates the drilling velocity, which can be reached by using thermal spallation drilling, as a function of the drill head operating conditions and the prevailing rock formation. This model can also be used to design spallation drill heads with respect to the applied combustion reaction and the jet velocities created.

Before the modeling approaches are introduced, the general process principles of thermal spallation drilling will be discussed. In general, the operating conditions occurring during the spallation process can be divided into the required rock-side and fluid-side operating conditions. Thereby, the fluid-side conditions are a combination of the heat transfer coefficient h_{fi} between rock surface and impinging fluid jet and the spallation temperature T_{SP} induced on the rock surface by the flame [50, 69, 70]. The spallation temperature T_{SP} is defined as the local surface temperature in the failure plane of the spall, measured directly after it detached from the surface [47, 60]. Therewith, this variable couples rock-side and fluid-side conditions, as the temperature, which is required to induce spalling, is a function of different properties of the rock and its internal structure. In conclusion, for a specific rock type appropriate flame operating conditions have to be found in order to initiate thermal spallation.

Generally, the surface temperature has to be kept below the melting point, which determines the upper limit T_M of the range of conditions

where spallation is applicable (see Fig. 4.1). If the melting temperature is exceeded, spallation will stop, as only insufficient thermal stresses can be induced [97, 98]. This originates from the effect that Young's modulus will decrease and fracture toughness will significantly increase close to the melting temperature [99].

Similar to the upper limit, a lower limit exists for the appearance of the spallation process. These minimal required boundary conditions are characterized by the lowest spallation temperature $T_{SP,min}$ and heat transfer coefficient $h_{fl,min}$ where spallation can be successfully initiated. If this temperature level is not exceeded, the thermal stresses are insufficient for thermal cracking and the rock does not spall. Additionally, if the heat transfer coefficient is too low, thermal cracking is not limited to the localized heating zone, but global cracking of the rock sample will occur, which will impede spalling, as the rock can expand into these cracks, preventing sufficiently high thermal stresses from being created.

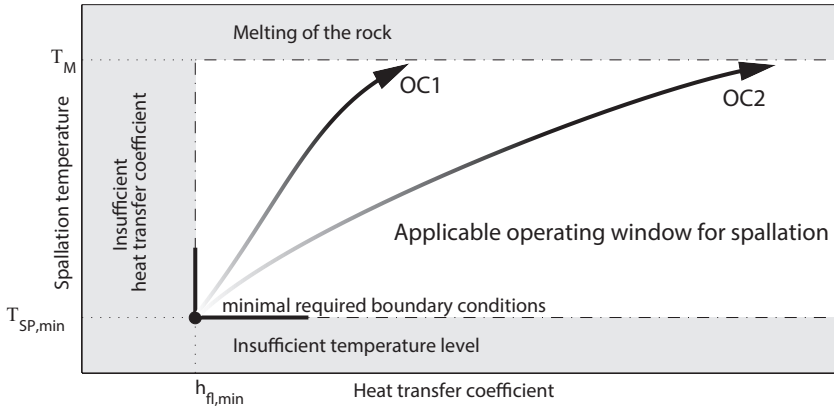


Figure 4.1: Illustration of the applicable operating window where thermal spallation drilling can be used, with specific operating curves (OC) of exemplary heating processes highlighted.

The minimal required boundary conditions specify the size of the operating window where spallation can be utilized (see Fig. 4.1). They are significantly a function of the rock properties. If the rock properties are unfavorable for spalling, higher spallation temperatures $T_{SP,min}$ are

required to initiate spalling, which will reduce the size of the operating window. If the required spalling temperature exceeds the melting temperature, the rock is unspallable.

The different heating concepts (flame, laser, plasma) have different operating curves (OC, see Fig. 4.1), all of which are inside the operating window. In general, by increasing the heat transfer coefficient, the spallation frequency will increase, which leads to a faster drilling process [70]. High heat transfer coefficients at moderate flame temperatures below the melting temperature of the rock will lead to the fastest drilling velocities. Nevertheless, the highest drilling velocity is usually not the optimal drilling velocity from an economical point of view.

Different modeling approaches have been reported in literature, describing these general characteristics of the spallation process [49, 50, 100]. Nevertheless, none of these available models sufficiently consider the coupled process of thermal stress induction and fracture-based mechanics in rocks by additionally providing straightforward application possibilities without the need for additional calibration experiments. Therefore, in this chapter of the thesis, an interlinked model based on linear fracture mechanics and the transient temperature distribution inside the rock structure is presented. In order to derive the model, first the postulated operating window concept, determined by the minimal required boundary conditions, will be experimentally validated. Thereafter, the first model will be discussed, which can be used to evaluate the critical conditions required to initiate thermal rock fracturing and to map rocks, according to their ability to spall. Followed by the introduction of a second model, which is based on the prior discussed model and estimates the maximal possible rate of penetration (ROP), as a function of the specific operating conditions (rock- and fluid-side). These two models form an important basis to evaluate the applicability of the spallation technology in real drilling applications and can be used to design spallation drilling tools, according to the optimal heat transfer coefficient and flame temperature.

4.1 Preliminary study: experimentally derived operating conditions

In order to preliminary verify the principle of the applicable operating window, the appearing boundary conditions are first experimentally determined. Therefore, firstly, the minimal required boundary conditions, determining the size of the operating window, are obtained in spallation experiments performed on granitic rock samples. In this study also important experimental aspects, how boundary conditions during spallation drilling can be quantified, are discussed. Thereafter, the complete operating curve of a flame-jet operated with a mixture of methane, air and oxygen is experimentally assessed, to verify the proposed operating window and operating curve principle.

4.1.1 Minimal required boundary conditions¹

As discussed above, the minimal required boundary conditions define the lower limit of the applicable operating window for spallation (see Fig. 4.1). In this thesis, the minimal required boundary conditions were defined as the conditions where at least a single spall could be detected by the measuring devices. Under this lower limit, the required heat transfer coefficients and surface temperatures are not reached, the rock will heat up too slowly, no steep temperature gradient is created inside the rock, which will inhibit the spallation process, as only insufficient thermal stresses are created. In the following, these minimal required boundary conditions will be experimentally derived for two exemplary selected granitic rock types.

¹This section is based on Kant et al., International Journal of Rock Mechanics and Mining Science [94]

4.1.1.1 Experimental procedure and rock material

As experimental setup the s-ASDP setup (Chapter 3.1) is used in its air configuration. The flame of the burner impinges orthogonally onto the 250mm x 250mm x 150mm large, air dried rock samples. The minimal required boundary conditions were derived by adjusting constant burner flows ($\dot{V}_{CH_4} = 0.3 \text{ Nm}^3/\text{h}$, $\dot{V}_{air} = 2.7 \text{ Nm}^3/\text{h}$, based on the normal conditions of 0°C and $1013.25 \text{ hPa}(a)$) and by increasing the stand-off distance (SOD) in between the different conducted experiments (see Table 4.1). During the single spallation experiments, the SOD was kept constant.

Table 4.1: Conducted experiments for the different rock types.

SOD [mm]	Gotthard Granite	Bethel Granite
50	✓	✓
80	✓	✓
110	✓	✓
130	✓	✓
140	X	✓
150	X	✓
160	X	X

In the experiments marked with ✓ (see Table 4.1) spallation could be observed. In contrary, experiments marked with X no spallation could be detected anymore. The table shows that spallation will stop for higher SODs, whereupon differences in the rock types can already be observed, as Bethel spalled for higher SODs than Gotthard granite. For the further investigation of the boundary conditions, the evaluation of the appearing boundary conditions was limited to the most interesting SODs.

Two granitic rock types were used in this study, commercial named as Gotthard granite (G) from Gurnellen, Switzerland and Bethel White granite (B) from Bethel, Vermont, USA. Thin sections of these rocks are shown in Fig. 4.2. Both rocks consist mainly of quartz, K-feldspar and plagioclase with minor amounts of biotite and muscovite. Both samples have variable grain sizes, ranging with feldspar up to ca 4mm.

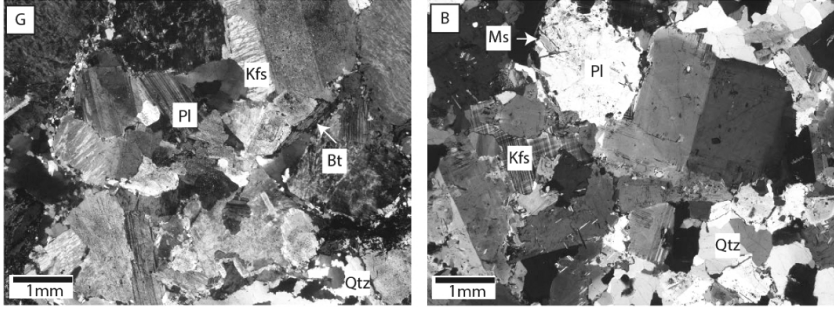


Figure 4.2: Thin sections of Gotthard (G) and Bethel (B) granite under cross polarized light. The rocks are mainly composed of quartz (Qtz), K-feldspar (Kfs), plagioclase (Pl) and minor amounts of biotite (Bt) and muscovite (Ms).

The spallation temperature was measured by using high-speed pyrometers (Chapter 3.1), which allow to resolve the disintegration of the single spalls in time and space. In order to quantify the heat transfer phenomena, the rock samples were replaced by the calibrated Wuntronic sensor (Chapter 3.3.1). The heat transfer coefficient h_{fl} [$W/(m^2K)$] was determined by measuring the heat flux q_{sens} [W/m^2] in the stagnation point of the impinging flame jet with an industrial heat flux sensor along with the fluid temperature T_{fl} and the surface temperature of the sensor $T_{s,sens}$ (Eq. (4.1) and Chapter 3.3.1).

$$h_{fl} = \frac{q_{sens}}{T_{fl} - T_{s,sens}} \quad (4.1)$$

4.1.1.2 Methodology for the surface temperature measurements

In order to accurately measure the surface temperature, the emissivity of the investigated rock samples was determined, according to the reference emissivity material method described in ISO 18434-1:2008 [101]. Pyromark 2500 [88]) was used as the required reference paint. The emissivity of the rock types were measured in the temperature range of $T_s = 400 - 675^\circ C$ and resulted in emissivity values of $\varepsilon_{Gotthard} = 0.549 \pm 12\%$ and $\varepsilon_{Bethel} = 0.434 \pm 17\%$. It has to be considered that the reported values only account for the operating wavelength ($\lambda = 2.3\mu m$) and the

applied angle ($\phi = 30^\circ$, see Fig. 3.1) of the installed pyrometers.

As spallation is a high-speed transient process, a reliable measurement procedure is necessary to accurately determine the surface temperatures during the process. Therefore, the influence of the uncertainty of the emissivity measurement on the surface temperature measurement was investigated and the error induced by the impinging flame was identified (see Fig 4.3). Further information about this error assessment can be found in Kant *et al.* [60]. Additionally, the systematic accuracy of the pyrometer is considered, which is given by the manufacturer of the pyrometer and can be calculated according to Eq. (4.2),

$$\Delta T_{sys} = \pm(0.3 \cdot 10^{-3} \cdot T_{obj} + 2^\circ C) \quad (4.2)$$

where ΔT_{err} is the systematic error of the devices in $[\circ C]$ and T_{obj} the surface temperature of the object in $[\circ C]$.

Combining the different error estimations, the total uncertainty of the surface temperature measurement can be derived (Fig. 4.3). As the relative uncertainty accounts for only 5-6%, in the temperature range interesting for spallation, accurate surface temperature measurements are possible with the described measuring principle. Additionally, the absolute uncertainty function presents a minimum at a surface temperature of approx. $T_{SP} = 500^\circ C$, which is near the temperature were spallation occurs (Section 4.1.1.4).

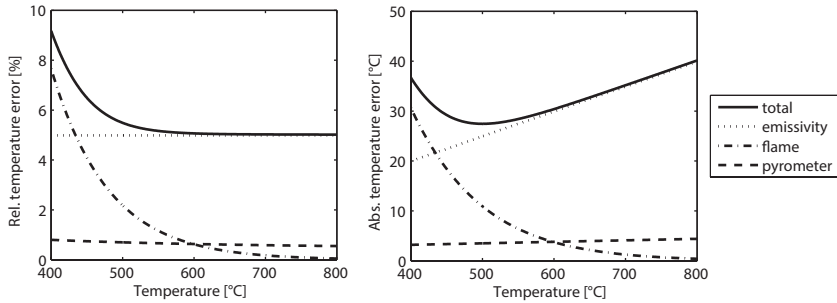


Figure 4.3: Relative and absolute uncertainty of the temperature measurement; total: total error; emissivity: error due to the uncertainty in the emissivity measurements. Flame: error due to the influence of the flame; pyrometer: accuracy of the pyrometer.

4.1.1.3 Processing of the raw data

Fig. 4.4 (a) shows a typical surface temperature over time plot of the experimental raw data. The temperature rises within a few seconds to about 600°C and spallation starts, indicated by a rapid temperature drop and followed by a heating period until the next spall detaches. Additionally, spalls can significantly overheat, if they are not removed by the momentum of the impinging flame jet and surface temperatures of about $T_{SP} = 1000^{\circ}\text{C}$ can be reached (see Fig. 4.4 (a) at $t \approx 90\text{s}$). When the spall finally detaches from the surface, the temperature drops back to the level before the spall overheated.

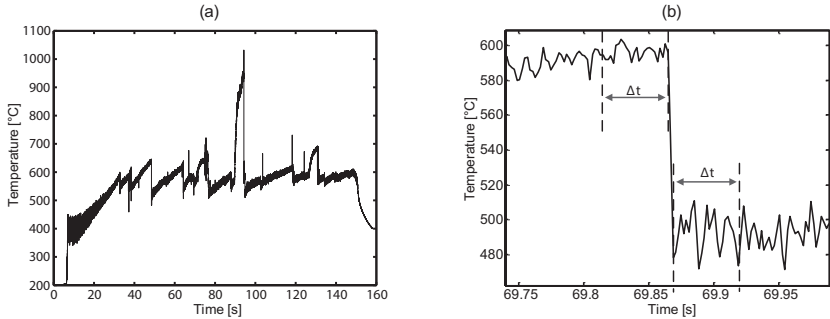


Figure 4.4: (a) Typical figure of the acquired raw data of the temperature measurement during spallation; (b) Detachment of a single spall

In Fig. 4.4 (b) it can be seen that the applied measurement principle is able to resolve the detachment of a single spall. Fig. 4.4 (b) shows that the spallation process induces a temperature difference of approx. $\Delta T = 100^{\circ}\text{C}$ in a few milliseconds. In order to exactly determine the temperature before and after the detachment of a spall, the temperature values are averaged over a time period of $\Delta t = 50\text{ms}$. Thus, the influence of fluctuations induced by the flame is minimized.

4.1.1.4 Spallation temperature measurements

As stated above, two different rocks were investigated in this report: Gotthard Granite (Switzerland) and Bethel Granite (USA). For all ex-

periments the post-processing priorly discussed was applied. The experimental setup introduced above was used and for every SOD and rock type investigated three different experiments with different rock samples were conducted.

Fig. 4.5 shows the mean spallation temperatures \bar{T}_{SP} averaged over all spalls detected during the individual experiments. Thereby, the error bars do not indicate the measurement error, but show the deviation in-between all detected spalls. This is significantly higher than the measuring error, which accounts for only 5-6% of the spallation temperature, as described in Section 4.1.1.2.

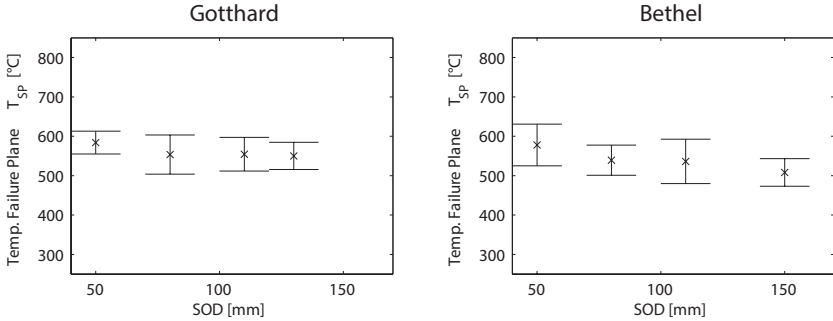


Figure 4.5: Summary of the observed mean spallation temperatures at different SODs for Gotthard and Bethel Granite

It can be seen that the mean spallation temperature ranges between 500°C and 600°C , whereas no significant change between the different investigated SODs could be observed. This suggests that heat transfer coefficient and spallation temperature can be considered as variables with a decoupled influence on the spallation effect.

4.1.1.5 Stagnation point heat transfer coefficient measurements

Fig. 4.6 shows the determined heat transfer coefficient h_{fl} for the different experiments. The heat flux q_{sens} was measured with the calibrated heat flux sensor (Chapter 3.3.1) in the stagnation point of the impinging flame jet. The stagnation point is the center point of the impingement,

where the middle stream line hits the impingement plate and the local velocity is zero. Before every measurement, a probe was inserted to centralize the system around this point and the sensor was moved in a plane orthogonally to the burner to assure that the heat flux profile is symmetrical around the selected stagnation point. The flame temperature was measured for every SOD with the principles discussed in Section 3.3.1 and resulted in temperatures between 1450°C and 1100°C .

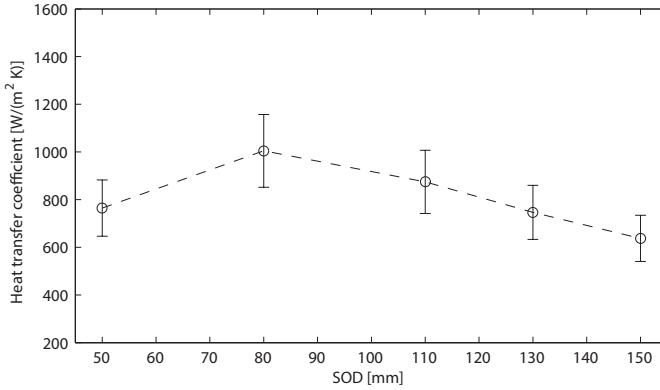


Figure 4.6: Results of the heat transfer coefficient in the stagnation point of the flame jet for different SODs

According to Fig. 4.6, a maximal heat transfer coefficient of around $h_{fl} = 1000\text{W}/(\text{m}^2\text{K})$ at a SOD of 80mm was reached during the impingement experiments. Thereafter, the heat transfer coefficient declines for increasing and decreasing SODs. This characteristic maximum at a specific SOD was already observed in other investigations using impinging isothermal gas and flame jets [102].

4.1.1.6 Boundary conditions

If the reported mean spallation temperatures \overline{T}_{SP} and the corresponding stagnation point heat transfer coefficients h_{fl} are combined, the minimal required boundary conditions for the successful initiation of the spallation process can be found (see Fig. 4.7).

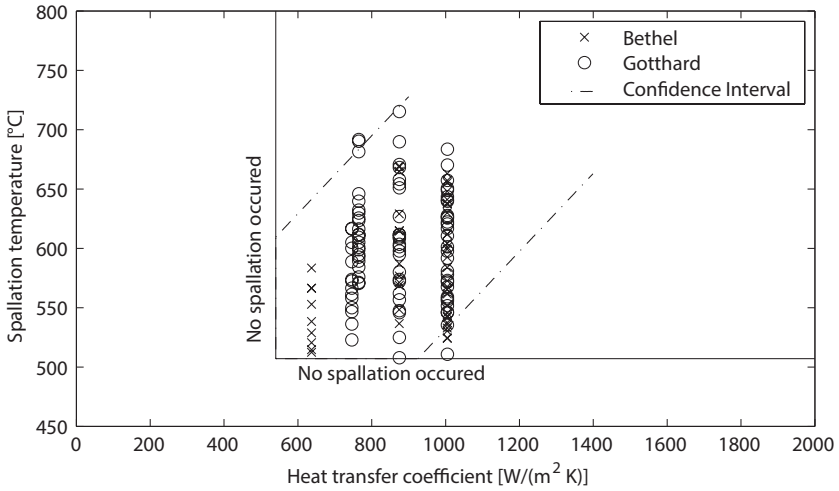


Figure 4.7: Summary of the reported minimal required boundary conditions

Fig. 4.7 shows the different measured boundary conditions for the conducted experiments. According to the acquired data, spalls can be detected for spallation temperatures exceeding $T_{SP,min} = 500^{\circ}C$ and heat transfer coefficients higher than $h_{fl,min} = 500W/(m^2K)$. The combination of these two values can be regarded as the minimal required boundary conditions. If the required heat transfer coefficients are not reached, the rock will heat up too slowly, no steep temperature gradient is created inside the rock and only undesired global cracks are created. Additionally, if the surface temperature is not above the stated limit, the locally induced thermal stresses are insufficient for spall formation. It can be concluded that, due to the detected sharp limitations of the spallation process with respect to the two investigated variables (spallation temperature and heat transfer coefficient), the concept of minimal required boundary conditions could be experimentally confirmed. Influences of the physical properties of the rock on these characteristic conditions could already be observed (Fig. 4.7 and Table 4.1) and will be further investigated in the course of this chapter.

4.1.2 Complete operating curve

In order to further verify the concept of the operating window where spallation can be used, the complete operating curve of a burner system, as depicted in Fig. 4.1, was experimentally evaluated. The operating curve was measured from the minimal required boundary conditions until melting of the rock structure occurred. This step indicates, whether the minimal required boundary conditions are also applicable to other granitic rocks and if the melting temperature limit postulated above is true.

4.1.2.1 Measurement principles and experimental setup

In principle the same measurement procedure as discussed above are applied for this further validation step. As the burner used in Section 4.1.1 cannot create the required temperatures to melt the rock, the s-ASDP drilling setup was used in its oxygen configuration (Chapter 3.1.2). Rock cores with a diameter of 85 mm and a length of 150 mm of Central Aare Granite (Chapter 3.2) were used for this evaluation.

In order to enhance the spallation process and to prevent global cracking of the rock samples, the uniaxial confinement system proposed by Hoeser *et al.* [63, 103] was applied. In this system, the rock core is placed between two metal flanges. The mechanical load is applied with four screws pressing the flanges together and inducing a confining stress in the bulk specimen (see Fig. 4.8). The flame impinges on the rock through a circular hole in the flanges.

For the temperature measurement, the same pyrometer and evaluation techniques as discussed previously were applied. The error estimation was repeated to account for the different characteristics of the other burner system. Similar trends were observed and implemented in the error estimation. The emissivity of Central Aare Granite was measured with the priorly discussed method, resulting in a constant emissivity of $\varepsilon = 0.515 \pm 0.075$. As the heat flux sensor does not withstand the high temperatures prevailing in this experimental set, the non-intrusive measurement technique developed in Chapter 3.3.2 of this thesis was used. The required sensitivity values were derived with a COMSOL modeling approach, where a heat flux step constant in space and time

and with a size of $q = 1W/m^2$ was applied over the circular hole in the flange. The required temperature was measured with the pyrometers discussed. As the Central Aare granite is highly heterogeneous, a metal block with the same dimensions as the rock samples was used for the heat flux measurements. All experiments were conducted with a constant flow rate of $m_{CH_4} = 0.8 m^3/h$, $m_{O_2} = 1.3 m^3/h$, $m_{Air} = 1.6 m^3/h$ and the SOD between nozzle exit and rock surface was varied to adjust to different operating conditions.

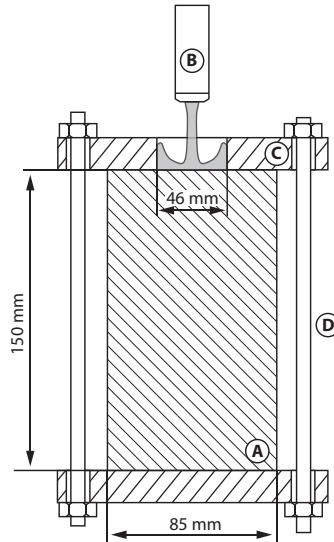


Figure 4.8: Illustration of the confinement system used in the experimental validation. A) rock sample, B) burner, C) metal flange, D) M16 thread with nuts to confine the rock.

4.1.2.2 Operating window and operating curve

The experiments were started with a large SOD between rock surface and nozzle. In-between the following experiments, the SOD was decreased, thus increasing flame temperature and heat transfer coefficient, until significant melting of the produced spalls could be observed. Fig. 4.9 shows the combined results of the appearing operating conditions, measured during this experimental set. The error bars in Fig. 4.9 indicate again the variation of the different detected spalls. It can be seen that the boundary conditions are first close to the minimal required boundary conditions of the Gotthard and Bethel granites. Then, the operating curve increases, first in a linear manner until a leveling-off can be observed at high temperatures of $900 - 1000^{\circ}\text{C}$, due to melting of the rock. The spallation temperature could not be further increased with higher flame temperatures or higher heat transfer coefficients and therefore the postulated melting temperature limit has been experimentally verified. The measured operating points form together the operating curve of the s-ASDP setup in its oxygen-configuration.

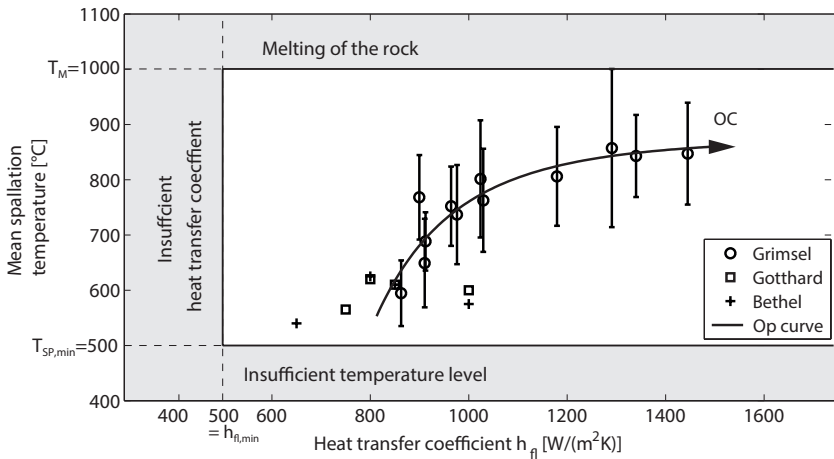


Figure 4.9: Operating window of thermal spallation drilling with granitic rocks and operating curve of the s-ASDP setup in its oxygen-configuration.

4.1.2.3 Comparison with literature data

In order to further verify the process principles, the reported data is compared in Fig. 4.10 with data of Rauenzahn [70] and Wilkinson [69]. As both authors used the heat flux instead of the heat transfer coefficient, the values reported above were converted into heat flux readings.

Regarding Fig. 4.10 it can be seen that the different data sets scatter over a wide range of operating conditions, caused by differences in the heating systems, the uncertainties of the measuring principle and the variety of the rock samples used. The data reported here and by Wilkinson lay in the proposed operating window. The temperature values of Rauenzahn are slightly outside the window. As already discussed by various authors (*e. g.* Wilkinson [69]) the measurement method used by Rauenzahn was more of a qualitative manner and seems to underestimate the actual temperatures.

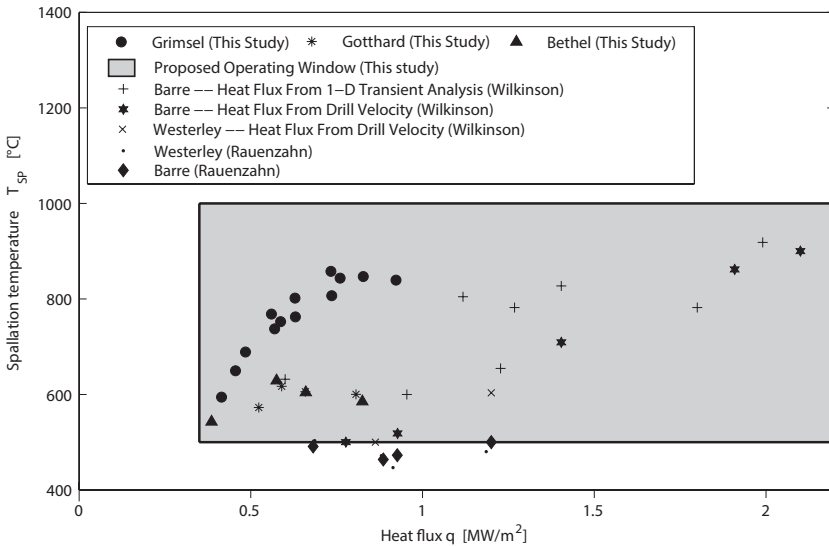


Figure 4.10: Comparison of the measured spallation temperatures and heat fluxes with literature data, Weibull Data for Barre Granite from Wilkinson and Tester [69], assuming physical properties at 573K (Fig. adapted from Wilkinson and Tester [69]).

4.1.3 Conclusions

The experimental evaluation supports the choice of the postulated operating windows in which the spallation process can be used and the corresponding operating curve of the heating systems. The minimal required boundary condition acquired from two granitic rocks could be also transferred to another granitic rock. Nevertheless, other rock types as sandstones or basalts will have other minimal required boundary conditions and melting temperatures and therefore a different operating window. As an experimental evaluation of all rock types is hardly feasible, an appropriate modeling approach is required, capable of estimating the spallability of various rocks.

4.2 Theory on the spallability of rocks²

In the following, a modeling approach is introduced, to estimate the operating conditions required to initiate spalling of certain rock formations and to map rocks according to their ability to spall.

If rocks are in general divided according to the Dunham classification in matrix-supported, clast-supported and crystalline rocks [104], the influence of the rock properties and its structure on the spallability can be already, without model, described in a qualitatively manner (Fig. 4.11). In rocks with a matrix-supported structure, the mineral components as quartz, plagioclase or micas are embedded in a relatively weak matrix composed of *e.g.* clay or silt [105]. If this rock structure is exposed to a steep temperature gradient, high thermal expansions are induced but only insufficient thermal stresses are created, as the hard components can expand into the rather soft matrix. If the matrix content decreases and a clast-supported structure is present, the minerals are in closer contact with each other and are therefore more restraint during their expansion. This induces higher thermal stresses, which will lead to spalling of the rock surface. Finally, if a crystalline interlocking structure is present and the minerals are in direct contact, high stresses are created and the spallation efficiency reaches its optimum.

²This section is based on Kant et al., Journal of Geophysical Research: Solid Earth [47]

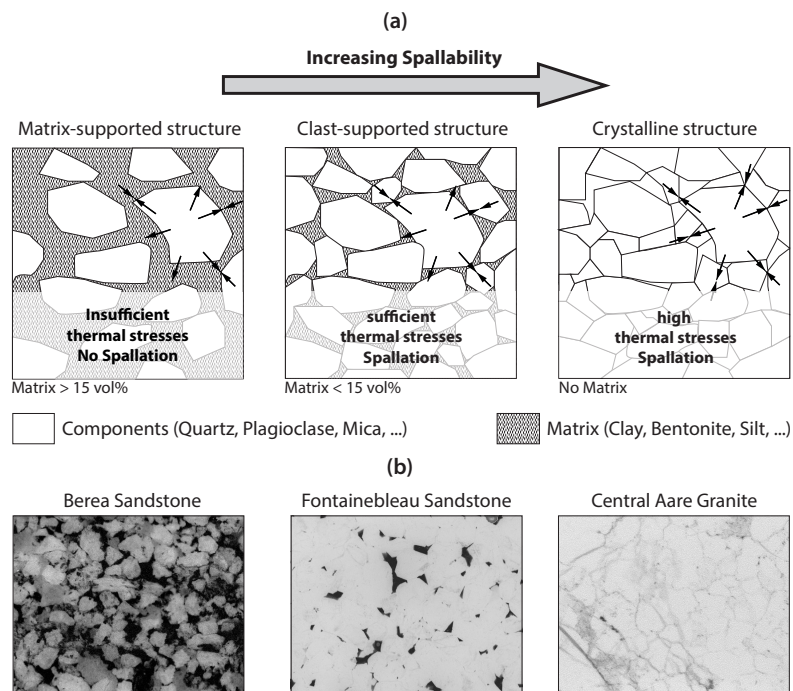


Figure 4.11: (a) Illustration of the influence of the rock structure on the spallation process; arrows indicate thermal stresses due to thermal expansion of the exemplary selected mineral and counter pressures due to adjacent hard minerals (Fig. adapted from Kant *et al.* [25]). (b) Grey-scale, inverted pictures of petrographic thin sections of some representative rock types, thin sections impregnated and pictures captured under UV light.

4.2.1 Principles of the model

Thermal crack creation and propagation of rocks is an intensively studied research area [106–110] and different modeling approaches have been developed to describe the required rock- and fluid-side parameters to induce thermal spalling of rocks [49, 50, 100]. Nevertheless, none of these available models sufficiently consider the coupled process of thermal stress induction and fracture based mechanics in rocks by additionally providing straightforward application possibilities without the need for additional calibration experiments. Therefore, in this chapter, a model is presented, which is based on linear fracture mechanics, the stress intensity concept and the transient temperature distribution inside the rock structure. The discussed model can be used to evaluate the critical conditions required to initiate thermal rock fracturing and to determine, if a certain rock formation can be spalled. The criterion is based on the models of Zhao *et al.* [111] and Lu *et al.* [108], which have been adapted to spalling of rocks and extended to include influences, due to prevailing confining pressures.

In this chapter, first the principles of the model, the mathematical formulation and approximations to simplify are presented. Thereafter, the general characteristics of the model are evaluated with a sensitivity study and other parameters, influencing spalling of rocks, are discussed. As a last step, the proposed model is compared with spallation experiments conducted on Central Aare granite. The applicability of this model is demonstrated by experimental surface temperature measurements when spallation occurs, which are in reasonable agreement with the model.

4.2.2 Derivation of the spalling criterion

The spalling model is based on concept of thermal fracture mechanics. If the stress intensity factor at the tip of a surface crack exceeds the fracture toughness of the material, crack growth occurs, which will lead to spallation. The stress intensity factor is induced by thermal stresses, due to the transient temperature distribution inside the body and external mechanical stresses.

The analyzed domain consists of a plane strain edge crack of length a embedded in a half space (see Fig. 4.12). The surface of this half space

is exposed to a convective boundary condition with the heat transfer coefficient h and the fluid temperature T_{fl} . Additionally, a general constant pressure state described by a pressure component parallel (p) to the crack homogeneously acts on the investigated crack.

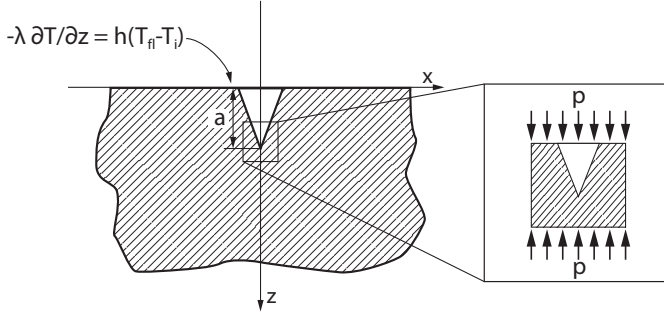


Figure 4.12: Half-space with an embedded crack, a convective boundary condition on the surface $z = 0$ and a vertical pressure state described by p

The presented crack geometry was selected as a reasonable approximation for the crack geometry with the highest propensity to grow. Therefore, it propagates first at similar geometries and loading situations. A validation later discussed in the manuscript (Section 4.2.4) shows the suitability of this approach.

4.2.2.1 Transient temperature distribution

As a first step to derive the stress intensity factor at the tip of the crack, the transient temperature distribution inside the domain is discussed. The description of the temperature field in the half space, due to a constant convective boundary condition, can be found in various literature sources [112–114] and is presented in Eq. (4.3),

$$\Theta = \Theta_{fl} \left\{ \operatorname{erfc} \left[\frac{z}{\sqrt{4\kappa t}} \right] - \exp \left(\frac{hz}{\lambda} + \kappa t \frac{h^2}{\lambda^2} \right) \cdot \operatorname{erfc} \left(\frac{z}{\sqrt{4\kappa t}} + \frac{h}{\lambda} \sqrt{\kappa t} \right) \right\} \quad (4.3)$$

where $\Theta = (T - T_i)$ is the difference between the evaluated temperature and the initial temperature, $\Theta_{fl} = (T_{fl} - T_i)$ the difference between the fluid temperature and the initial temperature, z the distance from the surface, κ the thermal diffusivity, t the time, h the heat transfer coefficient and λ the heat conductivity of the solid. A potential influence of the crack on the temperature distribution is neglected and the boundary condition is assumed to be constant around the crack. Additionally, the physical properties are assumed to be constant over the considered temperature range. In order to abbreviate this equation, several dimensionless variables are introduced: the dimensionless time τ , the Biot-number Bi based on the crack length and the dimensionless distance ξ (see Eq. (4.4)).

$$\tau = \frac{\kappa t}{a^2}, \quad Bi = \frac{h \cdot a}{\lambda}, \quad \xi = \frac{z}{a} \quad (4.4)$$

With these dimensionless numbers, the temperature distribution can be abbreviated to Eq. (4.5).

$$\Theta = \Theta_{fl} \left\{ \operatorname{erfc} \left[\frac{\xi}{\sqrt{4\tau}} \right] - \exp(Bi \xi + \tau Bi^2) \cdot \operatorname{erfc} \left(\frac{\xi}{\sqrt{4\tau}} + Bi \sqrt{\tau} \right) \right\} \quad (4.5)$$

In Conclusion, the temperature distribution is a function of the fluid temperature and the introduced dimensionless factors and can be written as $\Theta = \Theta_{fl} \cdot f_T(\tau, Bi, \xi)$.

4.2.2.2 General stress state and stress-intensity concept

The general stress-state around the crack is approximated with a plane-strain consideration [115, 116] by following the principles of linear fracture mechanics. The general constitutive relation for this stress state is shown in Eq. (4.6) [116],

$$\begin{aligned}\sigma_{xx} &= \frac{E}{(1-2\nu)(1+\nu)} ((1-\nu)\epsilon_{xx} + \nu\epsilon_{zz}) - \frac{E\alpha\Theta}{(1-2\nu)} \\ \sigma_{zz} &= \frac{E}{(1-2\nu)(1+\nu)} ((1-\nu)\epsilon_{zz} + \nu\epsilon_{xx}) - \frac{E\alpha\Theta}{(1-2\nu)} + p \\ \sigma_{xz} &= \frac{E}{1+\nu}\epsilon_{xz}\end{aligned}\quad (4.6)$$

where E is the Young's modulus, ϵ_{ij} the individual strain components, σ_{ij} the individual stress components, ν the Poisson's ratio, α the coefficient of linear thermal expansion, p is the pressure component (positive values point towards the investigated element, see Fig. 4.12) and Θ again the difference between the evaluated temperature and the initial temperature. It is assumed that the cold rock material around the crack acts as a confinement ($\epsilon_{xx} = \epsilon_{yy} = 0$) and on surface there is no additional stress other than due to the vertical pressure component p ($\sigma_{zz} = 0$). The confinement condition can be ensured by sufficient large rock samples or by additional confinement pressure, acting on the samples. These assumptions allows a simple stress consideration, with the resulting normal stresses in the x-direction, which are responsible for the crack formation presented in Eq. (4.7).

$$\sigma_{xx} = -\frac{E\alpha}{(1-\nu)}\Theta - p\frac{\nu}{(1-\nu)} \quad (4.7)$$

The stress intensity factor, acting on the tip of the presented plane strain edge crack of length a , due to an inhomogeneous stress field, can be calculated according to Tada *et. al* [117], as shown in Eq. (4.8).

$$K_I = 2\sqrt{\frac{a}{\pi}} \int_0^1 -\sigma_{xx} \frac{1.3 - 0.3\xi^{5/4}}{\sqrt{1-\xi^2}} d\xi = 2\sqrt{\frac{a}{\pi}} \int_0^1 -\sigma_{xx} f_K(\xi) d\xi \quad (4.8)$$

With the formulation for the stress state inside the half-space (Eq. (4.7)) and the transient temperature distribution discussed in Eq. (4.5), the stress intensity factor at the crack tip can be further described as shown in Eq. (4.9).

$$K_I = 2\sqrt{\frac{a}{\pi}} \left(\frac{E\alpha\Theta_{fl}}{(1-\nu)} \int_0^1 f_T(\tau, \text{Bi}, \xi) \cdot f_K(\xi) d\xi + \int_0^1 \left(p \frac{\nu}{(1-\nu)} \right) \cdot f_K(\xi) d\xi \right) \quad (4.9)$$

4.2.2.3 Definition of the Spallability number

The crack turns unstable if the stress intensity factor exceeds the fracture toughness of the rock ($K_I \geq K_{IC}$) [118, 119]. If this limit is exceeded, the crack will propagate through the solid towards the closest stress drain, which could be another crack or the surface of the half-space. If the crack reaches the surface of the domain, a so-called spall is formed, which will lead to the characteristic disintegration of the surface [48, 60]. A dimensionless number called Spallability is introduced to describe this critical condition where crack formation is initiated. This Spallability number is defined as $Sp = K_I/K_{IC}$ and with the derived formulation for the stress intensity factor (Eq. (4.9)) the Spallability number can be written, as shown in Eq. (4.10). If the critical value of $Sp = 1$ is reached or exceeded, the conditions for crack formation are fulfilled and the crack will propagate through the solid.

$$Sp = 2\sqrt{\frac{a}{\pi}} \left(\frac{E\alpha\Theta_{fl}}{K_{IC}(1-\nu)} \int_0^1 f_T(\tau, \text{Bi}, \xi) \cdot f_K(\xi) d\xi + \frac{1}{K_{IC}} \int_0^1 \left(p \frac{\nu}{(1-\nu)} \right) \cdot f_K(\xi) d\xi \right) \geq 1 \quad (4.10)$$

With all introduced abbreviations written explicitly, the Spallability

number can be calculated according to Eq. (4.11).

$$\begin{aligned}
 Sp = 2\sqrt{\frac{a}{\pi}} & \left(\frac{E\alpha\Theta_{fl}}{K_{IC}(1-\nu)} \int_0^1 \left\{ \operatorname{erfc} \left[\frac{z}{\sqrt{4\kappa t}} \right] - \exp \left(\frac{hz}{\lambda} + \kappa t \frac{h^2}{\lambda^2} \right) \right. \right. \\
 & \cdot \operatorname{erfc} \left(\frac{z}{\sqrt{4\kappa t}} + \frac{h}{\lambda} \sqrt{\kappa t} \right) \left. \right\} \cdot \frac{1.3 - 0.3\xi^{5/4}}{\sqrt{1-\xi^2}} d\xi \\
 & + \frac{1}{K_{IC}} \int_0^1 \left(p \frac{\nu}{(1-\nu)} \right) \cdot \frac{1.3 - 0.3\xi^{5/4}}{\sqrt{1-\xi^2}} d\xi \Big) \geq 1 \quad (4.11)
 \end{aligned}$$

This equation can be used to assess the operating conditions (flame temperatures and heat transfer coefficients) required to initiate spalling of a certain rock formation and the time frame until the onset of spallation appears. The derived equations are only valid, if the assumptions used to derive this model are not violated. The most important assumptions, which have been used, are: (i) the physical properties can be evaluated at the temperature and stress state where the spall is formed and are constant along the crack length and around the crack, (ii) the stress state can be described by the presented simplified plane strain model, (iii) the temperature distribution is not significantly influenced by preexisting cracks and (iv) the used formulation for the crack intensity factor describes sufficiently the fracture mechanism.

4.2.2.4 Simplifications for the derived Spallability number

The Spallability number defined in Eq. (4.10) contains several terms, which are difficult to evaluate. Therefore, Eq. (4.10) will be simplified to enable convenient access to the derived Spallability criterion. The first integral can be approximated to sufficient accuracy (for $Bi < 10$), as shown in Eq. (4.12) and Fig. 4.13,

$$\int_0^1 f_T(\tau, Bi, \xi) \cdot f_K(\xi) d\xi \approx \left(1 - \frac{1}{1 + Bi} \right) f_3(\tau) \quad (4.12)$$

where $f_3(\tau)$ is a term, considering the transient change of the integral. As the Biot-number is based on the crack length, this simplification does not imply a practical restriction. The time when the crack is initiated is irrelevant for the problem investigated. Therefore, the time dependence

is neglected and the function $f_3(\tau)$ is simplified to a constant value representing the maximum value of this function for any dimensionless time τ (see Eq. (4.13) and Fig. 4.13).

$$A^* = \max(f_3(\tau)), \forall \tau > 0 \quad (4.13)$$

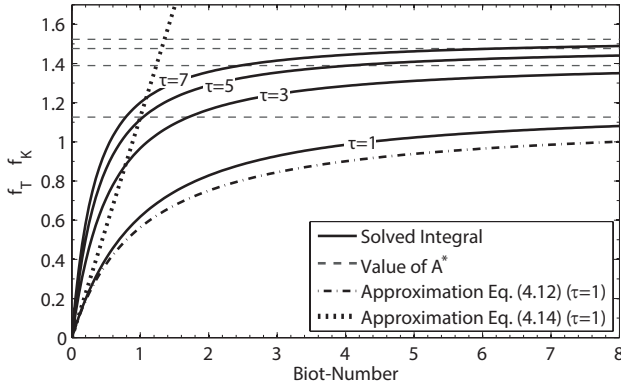


Figure 4.13: Comparison of the exact integral solution and the proposed approximation over a range of Biot-numbers and dimensionless times

For even lower Biot-Numbers ($Bi < 0.5$), Eq. (4.12) can be further simplified as shown in Eq. (4.14)

$$\int_0^1 f_T(\tau, Bi, \xi) \cdot f_K(\xi) d\xi \approx A^* \cdot Bi \quad (4.14)$$

If the pressure component is assumed to be independent of the crack length, the second integral of Eq. (4.10) can be directly numerically calculated (see Eq. (4.15)).

$$\int_0^1 f_K d\xi = \int_0^1 \frac{1.3 - 0.3\xi^{5/4}}{\sqrt{1 - \xi^2}} d\xi = 1.763 \quad (4.15)$$

Together with Eq. (4.14), the reduced Spallability number can be approximated as shown in Eq. (4.16).

$$Sp_{red} = \underbrace{2A^* \sqrt{\frac{a^3}{\pi}} \frac{E\alpha}{K_{IC}(1-\nu)\lambda}}_{Sp_{rock}} \cdot \underbrace{(T_{fl} - T_i) \cdot h}_{Sp_{fluid}} + \underbrace{\frac{2 \cdot 1.763}{K_{IC}} \sqrt{\frac{a}{\pi}} \left(p \frac{\nu}{(1-\nu)} \right)}_{Sp_{conf}} \quad (4.16)$$

The reduced formulation for the Spallability number of rocks can be divided into three parts. The first part (Sp_{rock}) is a function of rock properties, the second part (Sp_{fluid}) is only a function of heat transfer properties and the last term (Sp_{conf}) considers the influence of affective mean stresses on the crack tip. So in theory rocks can be spalled, if the fluid properties are adjusted to account for the properties of the rock and the current pressure state. A low rock Spallability Sp_{rock} can be compensated with high fluid operating conditions Sp_{fluid} , in order to exceed the critical Spallability number of $Sp = 1$. Hence, Eq. (4.16) can be used to map rocks according to their ability to spall. The only limit in this consideration is, that the melting temperature should not be exceeded, as already partial melting will significantly inhibit thermal crack formation [97, 98].

4.2.3 Sensitivity analysis and characteristics of the derived spallation criterion

A concise sensitivity analysis describes the impact of the different properties involved on the Spallability criterion and show the general characteristics of the model. The reduced Spallability number (Eq. (4.16)) is used, to asses the impact of every input property, when consecutively increased to 10% and 20% from the reference value. In order to normalize the influence, some properties were summarized to reference parameters (see Fig. 4.14). The values of all these reference parameters were set to one.

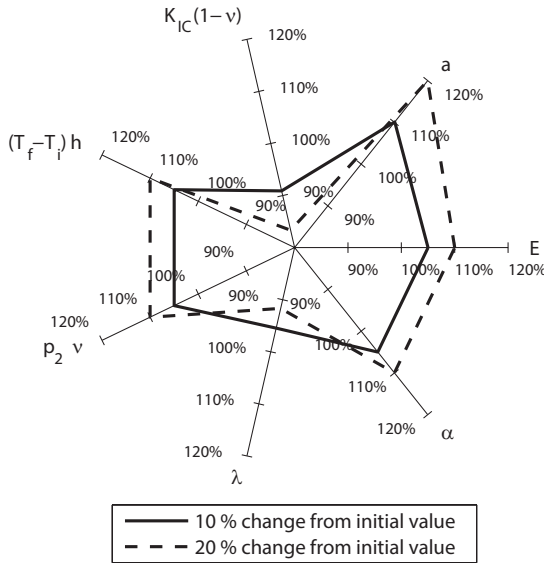


Figure 4.14: Sensitivity of the Spallability number on the required input parameters with $A^* = 1.763$; all other parameters are set to one

Fig. 4.14 shows the result of this sensitivity study. It can be seen that several parameters (E , α , $(T_{fl} - T_i) \cdot h$, $1/\lambda$) have a similar linear influence on the Spallability number. Nevertheless, the crack length has a considerably higher influence. Furthermore, increasing pressures parallel to the crack will increase the spallability and therefore significantly enhance the spallation process.

Additionally, the sensitivity analysis is consistent with already observed and reported influences of rock properties on the ability to spall. In order to initiate thermal spalling, the following rock properties are important: low thermal conductivities [48, 120], high Young's moduli (also described as hard rocks) [48, 50, 71], high uniaxial loads [50, 63], high thermal expansion coefficients [48, 50] and a low fracture toughness (brittle rocks) [50, 71].

Various other effects could potentially influence spalling and thermal

cracking, which are not considered in the derived spallation criterion. A significant increase of the thermal expansion coefficient during phase changes, as *e.g.* the α - β quartz transition, appearing at 573°C [121] at ambient conditions, will create additional mechanical stresses on preexisting cracks. If the affected minerals are confined by other rock material, the expansion will create further stresses on the rock structure, which enhances spalling [122].

On the other hand, as already discussed in the previous chapters, several effects exist which counter the spallation effect. If the rock is heated above the brittle-to-ductile temperature, the rock will react with plastic deformation to the thermal stresses rather than spalling [123]. Additionally, if the rock is heated above the melting temperature, only insufficient thermal stresses can be created [97, 98]. Both effects originate from the effect that the rock will accommodate strain plastically [99]. Therefore, the lowest melting temperature of all minerals present in the rock structure determines the upper temperature limit where spallation can appear [50, 60]. Additionally, weak mineral components (as *e.g.* in matrix supported rocks) or global fractures embedded in the rock structure will impede spalling of rocks, as the rock can expand into these components, preventing sufficiently high thermal stresses from being created.

4.2.4 Validation with Central Aare granite

In order to validate the proposed spallability model, the temperature jump, which the material has to be exposed to, in order to initiate thermal crack formation, was determined experimentally and compared with the values suggested by the model.

4.2.4.1 Experimental procedure and rock material

The spallation experiments were conducted with the s-ASDP setup in its air configuration (Chapter 3.1). During the experiment, the surface temperature is measured with a pyrometer, as introduced in Chapter 4.1.1.1. An uniaxial load p orthogonally to the front surface was applied to the rock cores during the spallation experiments with the confining system proposed by Hoerer *et al.* [63, 103] (see Chapter 4.1.2.1). Cores with a diameter of 85 mm and a length of 150 mm made out of Central Aare granite (Chapter 3.2) were selected as a suitable material for the validation. In Table 4.2 the required physical properties of the rock are summarized. Further information about the rock and its composition can be found in Chapter 3.2 of this thesis.

Table 4.2: Physical properties of Central Aare granite used for calculating the maximal possible temperature jump; data obtained from literature; all values have been evaluated at room temperature; (A): [77–79], (B): [78–80], (C): [81], (D):[82],(E): [79, 83]

Physical properties	Values	Ref.
Young's modulus	$E = 30 - 40 \text{ GPa}$	(A)
Poisson's ratio	$\nu = 0.19 - 0.33$	(B)
Fracture toughness	$K_{IC} = 1.5 \text{ MPa m}^{0.5}$	(C)
Crack length	$a = 20 \text{ }\mu\text{m}$	(D)
Coeff. of thermal exp.	$\alpha = (7.8 - 8.2) \cdot 10^{-6} \text{ 1/K}$	(E)
Initial temperature	$T_i = 20^\circ\text{C}$	(-)

4.2.4.2 Theoretically expected values according to the presented model

The theoretically required temperature jump to initiate thermal spalling can be calculated with the proposed model, as shown in Eq. (4.17). The temperature along the crack length is assumed to be constant.

$$\Theta = (T_{SP} - T_i) = \frac{(1 - \nu)}{E\alpha} \left[K_{IC} \sqrt{\frac{\pi}{4a}} \left(\int_0^1 f_K(\xi) d\xi \right)^{-1} - p \frac{\nu}{(1 - \nu)} \right] \quad (4.17)$$

For the calculation of the spalling temperature, the largest cracks initially present were selected, as they will have the lowest temperature required for thermal crack formation. Shorter cracks require higher surface temperatures before spalling appears and *vice versa* if higher temperatures are applied, more cracks can be activated and the spalling frequency will increase. The temperature difference was calculated with all possible combinations of the physical properties listed in Table 3.1 and summarized to a mean value with the according standard deviation (see Table 4.3). The model suggests that, without any additional uniaxial load, spalling of the rock surface should appear at temperatures between $390^\circ C$ and $560^\circ C$.

Table 4.3: Theoretically expected temperature jump of Central Aare Granite subject to various uniaxial compressive stresses p

Confining pressure p	θ mean value	θ range
0 MPa	$475^\circ C$	$390 - 560^\circ C$
27 MPa	$450^\circ C$	$365 - 535^\circ C$
48 MPa	$430^\circ C$	$340 - 510^\circ C$

4.2.4.3 Experimental results and comparison with the model

The spallation experiments were conducted with three different external uniaxial confining stresses ($p = 0 \text{ MPa}$, $p = 27 \text{ MPa}$, $p = 48 \text{ MPa}$). As critical temperature for spalling, the temperature in the failure plane directly after the spall has detached from the surface was selected [50, 60, 69]. The evaluation algorithm discussed in Chapter 4.1.1.3 was applied to the temperature raw data from the pyrometer.

If no uniaxial confining stress is applied, temperatures in the crack plane of the rock ranged between 553°C and 694°C (see Fig. 4.15). These values are in reasonable agreement with the theoretically derived values of the spalling model, which estimates, as discussed above, temperatures between 390°C and 560°C . With increasing uniaxial confining load, the measured spalling temperatures decrease, as less additional thermal stresses are required to initiate spalling. This trend can be also observed in the theoretical values suggested by the model.

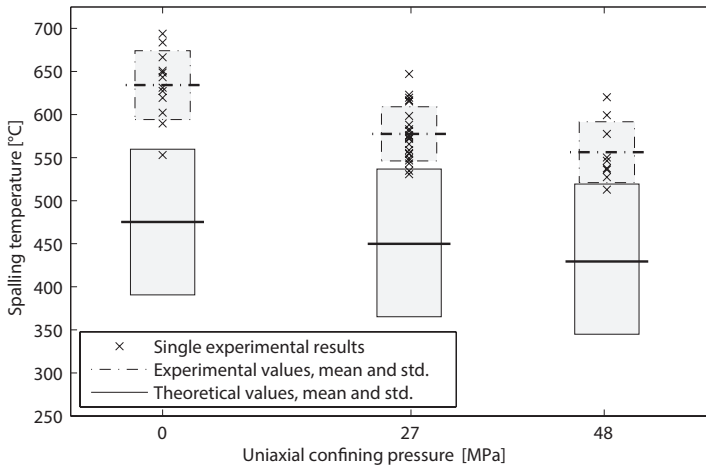


Figure 4.15: Temperature jump required to initiate spalling of Central Aare granite for different confining pressures p , calculated with the presented model and experimental data of the spalling temperature shortly after the onset of spallation

There is a systematic bias towards higher observed spallation onset temperatures when compared to the model. In non of the experiments the first initiated spall was detected by the measurement method, as the spall did not detached in the localized measurement area of the pyrometer. After the first spall detaches from the surface, the surface temperature continues to rise. With higher temperatures, cracks of shorter lengths can be initiated (see Eq. (4.17)) and spalls will be detected also at this higher temperature level. Therefore, the observed experimental temperature (Fig. 4.15) are higher than the values predicted by the model, which only considers the onset of spallation, if the largest crack length is used for the calculation. Additionally, the model values have been calculated with physical properties at room temperature. As physical properties of rocks vary significantly with increasing temperature and pressure, further inaccuracies are introduced to the evaluation. Still, the values calculated with the presented model are in reasonable agreement with the experimental values observed on Central Aare granite. Additionally, the selected crack geometry and other assumptions seem to be able to describe thermal spalling of rocks in a fit-for-purpose manner.

4.2.5 Rock spallability criterion

In order to be able to discuss the applicability of thermal spallation drilling in deep drilling operations, a criterion is required which can characterize rock types according to their ability to spall. Thus, the Rock-Spallability number introduced in Eq. 4.16 will be used to develop such a criterium. As the crack length a is locally, highly varying, this parameter is left out of the consideration, which leads to Eq. 4.18.

$$Sp_{rock,red} = \frac{E\alpha}{K_{IC}(1-\nu)\lambda} \quad (4.18)$$

In order to assess, if this simplified equation is suitable to characterize rocks according to their ability to spall, rock cores with a diameter of 85mm from seven different rock types have been selected for experimental validation. The used rock types are Fontainebleau sandstone (F), Rorschach sandstone (CH), Berea Sandstone (US), Central Aare granite (CH), Westerley granite (US), Sioux quartzite (US) and Äspö diorite (S). The rock properties required to calculate Eq. 4.18 are taken from

literature and are summarized in Table A.1 in Appendix B. In order to assess experimentally the spallability of the different rock samples, the s-ASDP setup (Chapter 3.1) is used and each rock sample is exposed without confinement to a flame jet with about 1300°C . Figure 4.16 shows the results of the experiments together with the Rock-Spallability number, calculated with Eq. 4.18 and the properties listed in Table A.1 in Appendix B. Rock types where spalling could be observed are marked in green and rocks which didn't spall are marked in red. It can be seen that, if a certain value of the Spallability number is underrun, no spalling can be observed and the rock type is unspallable. This leads to the conclusion that the discussed reduced Rock-Spallability number can sufficiently characterize spalling behaviours of rocks and a rock-spallability of about $Sp_{rock,red} = 1.25 \cdot 10^{-4} \text{ W K m}^{0.5}$ is required to initiate spalling.

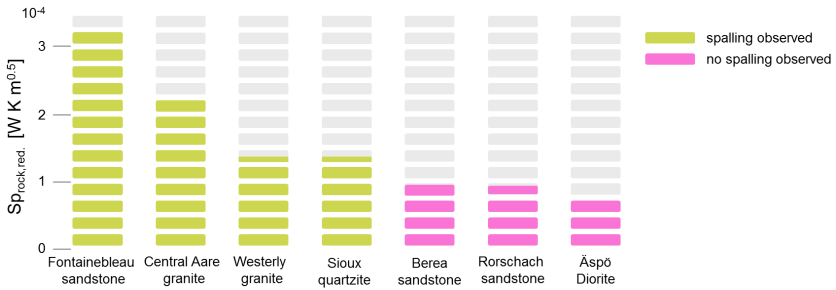


Figure 4.16: Results of the spallability validation. Experiment conducted at ambient conditions without external confining pressure. Rock-spallability calculated with Eq. 4.18

4.2.6 Conclusions

A model to estimate spalling and thermal cracking behaviors of rocks with a focus on thermal spallation drilling is presented. The model is based on linear fracture mechanics and the stress intensity concept. It couples rapid heat transfer with induced thermal stresses and fracture based mechanics in rocks.

The model allows the determination of the operating conditions required to initiate thermal rock spalling. Extensive efforts to experimentally de-

termine the operating window are no longer necessary. Additionally, a Spallability number is presented allowing a straightforward application of the derived equations to various conditions and a classification of rocks according to their ability to spall. This number is divided into terms representing the physical properties of the rock, the heat transfer properties of the fluid and the influence of confining pressures. The model follows already reported influences on the spallability of rocks. For thermal spalling the following rock properties are favorable: low thermal conductivities [48, 120], high Young's moduli [48, 50, 71], high deviatoric stresses [50, 63], high thermal expansion coefficients [48, 50] and low fracture toughness values [50, 71].

An experimental validation of the model with a typical granitic rock was conducted. The model was in reasonable agreement with the experimental data. The measured temperature jump required to initiate surface spalling could be reproduced by the model.

4.3 Model for the maximum drilling velocity³

The model discussed in the previous chapter is useful to assess the flame operating conditions, required to initiate the spallation process. Additionally, a determination, if a certain rock formation is spallable, is possible. Having determined the operating window for any rock, the next step is to evaluate the operating point, where spallation drilling can achieve the optimal drilling velocity. The drilling velocity or rate of penetration (ROP) is an important cost driver, as it directly determines the time required for the drilling process and thus the overall cost of the well. Low penetration rates in hard basement rocks together with high wear rates of the drill bits currently pose severe challenges to deep drilling operations with conventional drilling tools (see Chapter 2.4). Even with low penetration rates, a high power input from the top-drive is required, rendering a process with a low energy efficiency. All these factors lead to high cost for drilling a deep well in hard rocks. The focus is here on

³This section is based on Kant et al., Proceedings, 41st Workshop on Geothermal Reservoir Engineering [26]

cost expressed in USD/m; only to a lesser degree to the well unit costs (USD/MWh). Therefore, in order to facilitate spallation drilling as an alternative technology, one of the following two possible options have to be fulfilled:

- spallation drilling can reach significant higher penetration rates when compared to conventional drilling at slightly higher drilling costs.
- similar penetration rates can be reached at significant lower drilling cost (due to lower wear-rates and less power input)

In order to investigate, if one of these options can be realized, first, a model for estimating the drilling velocity will be derived and validated with experimental data. Then the model will be used to establish design guidelines for spallation drilling tools with respect to the optimal flame temperatures and fluid velocities, required to reach a certain drilling velocity using a specific burner-rock combination.

4.3.1 Quasi-steady state model

The model assumes that the velocity is only limited by the diffusion process of heat through the rock and not by the rock fracturing process itself. This assumption seems to be appropriate, as the fracturing process occurs in a millisecond and micrometer range [60, 69, 70]. The model is based on a one-dimensional system: the surface of a semi-infinite body $x > 0$ is exposed to a convective boundary condition with the heat transfer coefficient h and the fluid temperature T_{fl} . The surface $x = 0$ moves along the x-coordinate with a constant velocity u (see Fig. 4.17). Therewith, the position of the surface in time can be described as $x = ut$.

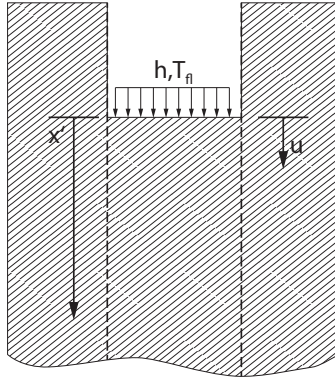


Figure 4.17: Semi-infinite body with a moving convective heat source at $x = 0$.

This heat conduction problem can be mathematically described as shown in Eq. (4.19)-(4.21),

$$\frac{\partial^2 T}{\partial x^2} = \frac{1}{\kappa} \left(\frac{\partial T}{\partial t} + u \frac{\partial T}{\partial x} \right) \quad (4.19)$$

$$T = T_i, \quad t = 0, \quad x = S \quad (4.20)$$

$$\frac{dT}{dx} = h'(T - T_{fl}), \quad t > 0, \quad x = 0 \quad (4.21)$$

with the thermal diffusivity κ , the initial temperature T_i , the relative heat transfer coefficient $h' = h/\lambda$ and S the size of the investigated domain.

In order to solve this problem, the boundary system is transformed to a quasi-steady state system:

$$x = x' + u t \quad (4.22)$$

With this formulation, the equation system (Eq. (4.19)-(4.21)) can be written as:

$$\frac{\partial^2 T}{\partial x'^2} = -\frac{u}{\kappa} \frac{\partial T}{\partial x'} \quad (4.23)$$

$$T = T_i, \quad t = 0, \quad x' = S \quad (4.24)$$

$$\frac{\partial T}{\partial x'} = h'(T - T_{fl}), \quad t > 0, \quad x' = 0 \quad (4.25)$$

The differential equation (Eq. (4.23)) can be directly solved by using its characteristic equation (see Eq. (4.26)).

$$T = A \cdot e^{-\frac{u}{\kappa} x'} + C \cdot e^0 \quad (4.26)$$

The integration constants A and B are determined from the boundary conditions described in the formulation of the quasi-steady system. Eq. (4.24) directly leads to $C = T_i$ and by applying the convective boundary condition described by Eq. (4.25), the integration constant A can be determined as:

$$A = \frac{h'(T_{fl} - T_i)}{\frac{u}{\kappa} + h'} \quad (4.27)$$

The temperature distribution, due to a moving surface exposed to a convective boundary conditions, is then expressed as shown in Eq. (4.28).

$$T = \frac{h'(T_{fl} - T_i)}{\frac{u}{\kappa} + h'} e^{-\frac{u}{\kappa} x'} + T_i \quad (4.28)$$

Fig. 4.18 illustrates this temperature distribution for three different velocities of the moving surface $x = 0$. It can be seen, that with increasing velocity the slope of the profile inclines and the surface temperature at $x = 0$ decreases.

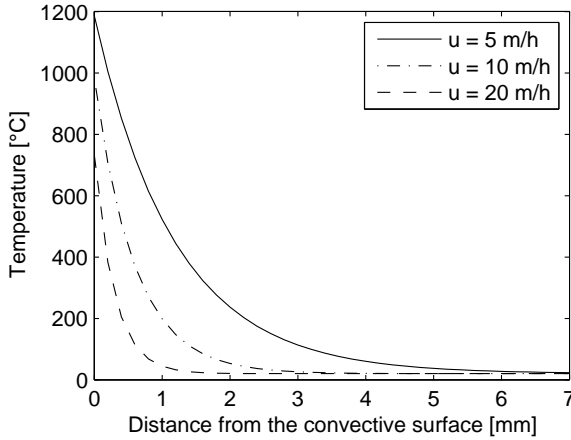


Figure 4.18: Temperature distribution due to a moving convective heat source at three different velocities; $h = 10 \text{ kW}/(\text{m}^2 \text{ K})$, $T_{fl} = 1500^\circ\text{C}$, $T_i = 20^\circ\text{C}$, $\lambda = 3.2 \text{ W}/(\text{m}^2 \cdot \text{K})$, $\kappa = 1.65 \text{ mm}^2/\text{s}$

As spallation requires a specific temperature level in the surface layer of the rock (see Chapter 4.1.1) [50, 60, 69], one expects that if a certain drilling velocity is exceeded, the temperature in the surface layer will not be sufficient to reach the for spallation required temperature level.

4.3.2 Implementation of the spallation limits

In order to fully determine and to enable the derivation of the drilling velocity from Eq. (4.28), suitable values for the temperature T and the point x' where the temperature is evaluated have to be found. Therefore, the two main aspects of spallation drilling, as discussed in the introduction of this chapter, are considered: on the one hand the surface temperature has to be higher than the temperature required to initiate spallation T_{SP} and on the other hand the surface must be below the melting temperature T_M of the rock [50, 69, 94]. The spallation temperature T_{SP} has to be reached in the failure plane of the spall $x' = \Delta x$ (Chapter 4.1) and can be calculated with the previously introduced model (Eq. 4.17).

Then using Eq. (4.28), with all required parameters defined, the drilling velocity equation can be written as shown in Eq. (4.29).

$$\Theta_{SP} = T_{SP} - T_i = \frac{h'(T_{fl} - T_i)}{\frac{u}{\kappa} + h'} \exp\left(-\frac{u}{k}\Delta x\right) \quad (4.29)$$

This equation cannot be solved analytically for the drilling velocity. Instead, numerical approaches (*e.g.* with MATLAB) are required. As discussed above, spallation is suppressed, if the melting temperature $\Theta_M = (T_M - T_i)$ is reached or exceeded at the surface $x' = 0$. Then by using Eq. (4.28), the resulting equation can be solved for the maximal heat transfer coefficient, which can be applied before melting of the rock surface occurs (Eq. (4.30)).

$$h' = \frac{\Theta_M u}{\kappa(T_{fl} - T_i - \Theta_M)} \quad (4.30)$$

Eq. (4.30) is combined with the derived equation for the drilling velocity (Eq. (4.29)). The resulting equation can be simplified and after some algebra, the maximum drilling velocity which can be reached before melting occurs is shown in Eq. (4.31).

$$u_M = \frac{\kappa}{\Delta x} \ln\left(\frac{\Theta_M}{\Theta_{SP}}\right) \quad (4.31)$$

This equation is only a function of rock properties, as melting temperature and spallation temperature are material parameters (compare Chapter 4.2). Therewith, it can be concluded that the maximum possible drilling velocity does not depend on any burner configuration but only on the formation to be drilled. If the drilling velocity described by Eq. (4.29) reaches the limit described by Eq. (4.31), the surface starts to melt and the drilling velocity decreases to zero, as the spallation process stops [60]. In conclusion, the final statement for the drilling velocity can be described as shown in Eq. (4.32).

$$u = \begin{cases} \text{solve} \left(\Theta_{SP} = \frac{\frac{h}{\lambda}(T_{fl} - T_i)}{\frac{u}{\kappa} + \frac{h}{\lambda}} \exp\left(-\frac{u}{\kappa}\Delta x\right), \text{ for } u \right) & \text{if } u < u_M \\ \approx 0 & \text{if } u \geq u_M \end{cases} \quad (4.32)$$

4.3.3 Validation with experimental data

The equation for the drilling velocity in terms of heat transfer coefficient is shown in Fig. 4.19 together with experimental data collected and published by Hoesser [63]. Central Aare granite was used as the rock formation for the experiments and the model and the thermal properties at 500°C were selected for the evaluation [76]. The distance $x' = \Delta x$ between surface and failure plane was set equal to the average spall size obtained in the experiments reported by Hoesser [63]. The values derived in Chapter 4.2.4 were used as spallation temperature.

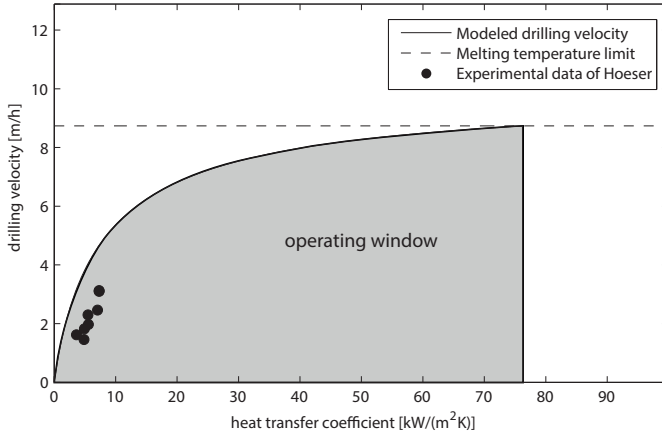


Figure 4.19: Drilling velocity model with experimental data from Hoesser [63]; model parameter: $\Theta_{SP} = 550^{\circ}\text{C}$, $\Theta_m = 1100^{\circ}\text{C}$, $T_{fl} = 1200^{\circ}\text{C}$, $\lambda = 2\text{W}/(\text{m}^2 \cdot \text{K})$, $\kappa = 0.7 \cdot 10^{-3}\text{m}^2/\text{s}$, $\Delta x = 200\mu\text{m}$

Fig. 4.19 suggests that the drilling velocity estimated with the model increases in a logarithmic manner. After a steep increase of the drilling velocity at rather low heat transfer coefficients, the velocity curve levels off and only increases moderately, until the melting temperature limit (Eq. (4.31)) is reached. The experimental data obtained by Hoesser [63] fit the models operating window. The measured drilling velocity is slightly slower than the model's estimation, which can be explained by non-ideal heat transfer, uncertainties in the measurements, inaccuracies

in the selected model parameters and most importantly by the fixed location of the heat source (the burner system) with respect to the drilling front. The latter leads to a decrease of the velocity with increasing experimental time. Nevertheless, the experimental process is quite close to the optimal suggested drilling velocity. Fig. 4.19 also shows that a ROP of about 9 m/h can be reached with the selected flame operating conditions and the rock formation until the melting limit is reached at heat transfer coefficients of about $77 \text{ kW}/(\text{m}^2 \text{ K})$. These limits depend on the properties of the rock. In different rock structures than the discussed one here, higher or lower ROPs might be reached.

4.3.4 Design of spallation drill bits

In the following chapter, methods will be described how the drilling velocity model can be used to design spallation drilling tools with respect to the optimal fluid temperature and jet velocity of a spallation drill bit from a projected rate of penetration (ROP). A careful selection of these parameters is required to achieve an optimal ROP and an efficient drilling process.

4.3.4.1 Fluid temperature

The selection of appropriate combustion temperatures for spallation is a demanding task, as the temperature is usually directly linked to the combustion reaction.

As flame temperatures can only be slightly adapted by varying the air to fuel ratio [124–126], a careful selection of the reaction is an important step for a successful design of a spallation drill head. Too high flame temperatures will lead fast to melting of the rock structure, which stops the spallation process. However, too low flame temperatures will not create the required surface temperatures for high ROPs at adequate heat transfer coefficients. The drilling velocity model can be used to evaluate the maximum possible ROP and the required heat transfer coefficient, if flame jets with different flame temperatures are used for drilling the same rock formation. Fig. 4.20 shows the results of the model for two drill heads operated with an hydrogen-oxygen and a methane-air mixture drilling a granitic formation.

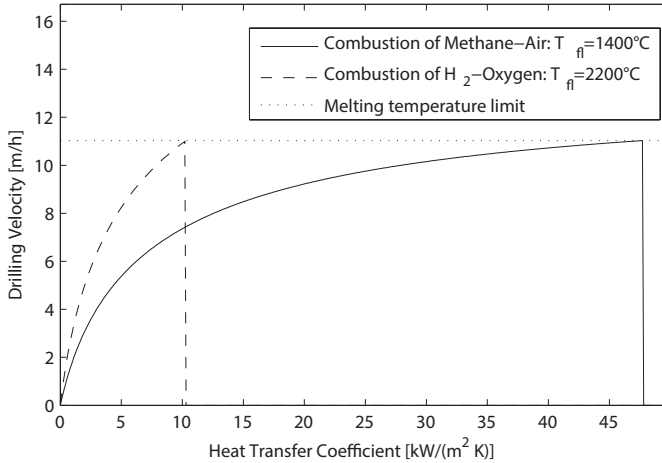


Figure 4.20: Possible operating window for two different spallation drill heads; one operated with a methane-air flame with an assumed flame temperature of 1400°C and the other one operated with an hydrogen-oxygen flame with an assumed flame temperature of 2200°C ; both drilling an exemplary granitic rock, common parameters: $\Delta x = 200\mu\text{m}$, $\lambda = 2\text{ W/(m K)}$, $\kappa = 0.7\text{ mm}^2/\text{s}$, $\Theta_{SP} = 500^{\circ}\text{C}$, $\Theta_m = 1200^{\circ}\text{C}$

It can be seen that the drill head operated with hydrogen-oxygen reaches faster higher ROPs, but has a smaller operating window. If this operating window is exceeded, due to sub-optimal spall removal, sub-optimal drill head feed or instabilities in the combustion process, the rock will partially melt, which considerably affects the drilling performance. But, the methane-air flame shows a significantly lower gradient. Therewith, the system is easier to control and operate. Considering also the significantly higher costs of oxygen compared to air, it can be seen that air-based systems can be favored over oxygen-based, if the required heat can be transferred to the rock and is not lost by entrainment of cold drilling fluid into the hot jet.

4.3.4.2 Jet velocities and mass flows

Combustion chambers are not designed for a specific heat transfer coefficient, but rather for a certain mass flow of fuel and oxidizers, leading to flame jets with a specific velocity at the exit of the nozzle. This flame jet then induces a heat transfer coefficient, when it impinges on a surface (Fig. 4.21).

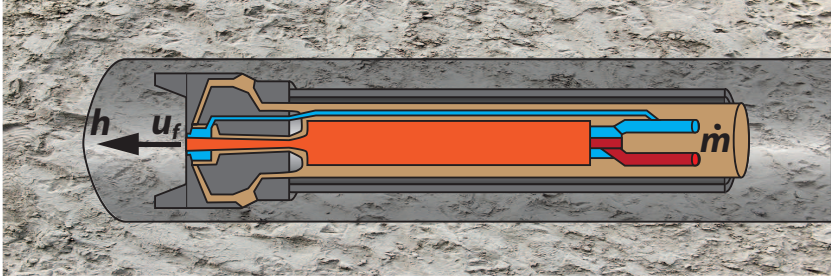


Figure 4.21: Illustration of a spallation drill head with the different flow characteristics highlighted.

The connection between jet velocity and heat transfer coefficient is covered by Nusselt correlations, which are available for numerous geometries, fluids (Prandtl-number) and velocities (Reynolds number). In the following, the described model is expanded with an exemplary selected Nusselt-correlation in order to enable an appropriate selection of the required jet velocities at the nozzle to achieve the target ROP. As a possible correlation, the equation proposed by Martin [127] (Eq.(4.33)) is used, which is valid for $120000 < Re < 400000$, $2.5 < r/D < 7.5$ and $2 < H/D < 12$,

$$Nu_{avg} = 0.151 Re^{0.775} Pr^{0.42} D/R \frac{1 - 1.1 D/R}{1 + 0.1(H/D - 6)D/R} \quad (4.33)$$

where Pr is the Prandtl number, Re the Reynolds number, D/R the ratio between nozzle diameter and borehole radius and H/D is the ratio between stand-off distance and nozzle diameter. Other correlations valid for different geometries or operating conditions might be more suitable in other scenarios. With the definition of the Nusselt number $Nu =$

$h D/\lambda_f$, the correlation between the heat transfer coefficient and the jet velocity v_f can be expressed as shown in Eq. (4.34),

$$h = 0.151 \frac{\lambda_f}{D} \left(\frac{u_f \cdot D}{\nu_f} \right)^{0.775} \left(\frac{\eta c_p}{\lambda_f} \right)^{0.42} \frac{D/R(1 - 1.1 D/R)}{1 + 0.1(H/D - 6)D/R} \quad (4.34)$$

where λ_f is the thermal conductivity of the impinging fluid, u_f its velocity and ν its viscosity. This relationship can now be integrated into the drilling velocity model (Eq. (4.32)) and jet velocities, required to achieve a target ROP, can be estimated. Fig. 4.22 shows the drilling velocity over a wide range of jet velocities for drilling in a granitic rock with an methane-air drill head.

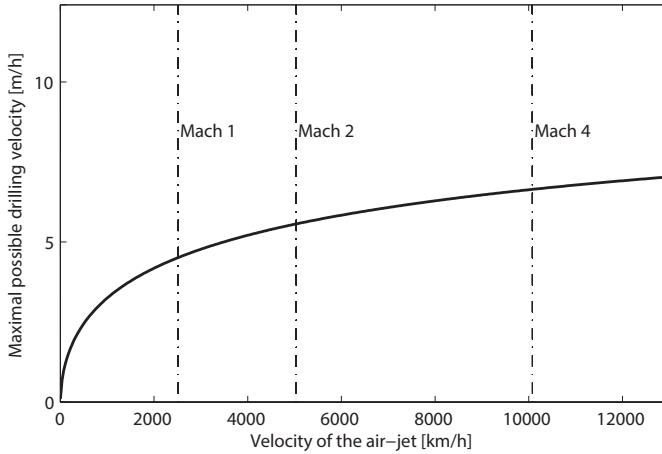


Figure 4.22: Possible drilling velocity over a range of jet velocities, with different Mach-numbers calculated for air at 1000°C highlighted for comparison, parameter: $H/D = 5$, $D = 5 \text{ mm}$, $Pr = 0.74$ [128], $\nu = 18 \cdot 10^{-7} \text{ m}^2/\text{s}$, $V = 1300^\circ\text{C}$, $\Delta x = 200 \text{ }\mu\text{m}$, $\lambda = 2 \text{ W}/(\text{m K})$, $\kappa = 1.7 \text{ mm}^2/\text{s}$, $\Theta_{SP} = 500^\circ\text{C}$, $\Theta_m = 1200^\circ\text{C}$

As Fig. 4.22 shows, in order to achieve high ROPs, extreme high jet velocities (well above supersonic speed) are required. Nevertheless, the ROP which can be achieved with moderate jet velocities ($v < \text{Mach}2$) is already sufficient for drilling operations in hard rock formations. Furthermore, the required mass flow, which has to be feed to the combustion

chamber in order to establish a jet with the required velocity u_f , can be calculated as expressed in Eq. (4.35),

$$\dot{m} = \rho_f \pi u_f D^2 / 4 \quad (4.35)$$

where D is the diameter of the nozzle and ρ_f the density of the fluid. With the required feed to achieve a certain ROP in a specific rock formation known, thermal spallation systems can be designed: combustion chamber volumes can be estimated, the diameter of the feed pipes in the drill string can be assessed and the power of the fuel and oxidizer pumps at the drill rig can be determined. This makes an improved cost estimation to evaluate the competitiveness of the technology possible, which will be discussed in the next chapter of this thesis.

4.3.4.3 Conclusions

The drilling velocity, which can be reached under realistic conditions, is an important parameter for the evaluation of the applicability and competitiveness of the spallation technology. The spallation process was simplified modeled with an analytical approach based on the transient head conduction, due to a moving convective point source. The model is based on a specific spallation temperature, which is required to initiate thermal crack formation. According to the model, the drilling velocity increases with logarithmicly until it reaches the process-limiting melting temperature. If the surface partially melts, the drilling process will stop. The model is in agreement with experimental data published by Hoerster [63].

The model can also be used to design and evaluate thermal drill heads with respect to the adjusted flame temperature and jet velocity.

4.4 Conclusions of this chapter

This chapter of the thesis shows that the operating window for spallation is determined by the melting temperature of the rock and the lowest surface temperature in connection with the lowest heat transfer coefficient where thermal spallation can be induced. As an experimental validation of these operating points for various different rocks is impractical to achieve, a model for thermal spallation drilling was introduced, composing of two different interlinked sub-models. The first model can be used to estimate the operating conditions required to initiate spalling of rocks and to map rocks according to their ability to spall. It shows that the thermal crack growth required to induce spallation is a function of the thermal gradient inside the rock and the overall temperature rise. The second sub-model assesses the maximum drilling velocity for a certain rock formation. Together they can be used to design spallation tools with respect to the fluid temperature and the optimal jet velocities or mass flows. Additionally, a general cost-benefit assessment of the spallation technology is possible with these models and will be performed in the next chapter of this thesis.

CHAPTER 5

Thermal spallation drilling in deep drilling operations

Thermal spallation drilling has been used for more than 50 years to excavate hard rock formations [48, 56, 58, 62, 66]. Nevertheless, although thermal spallation drilling seems to be a reasonable option for deep drilling operations, the technology has not been applied in any deep drilling project so far. This chapter aims to discuss some of the main challenges for thermal spallation drilling in deep drilling projects.

As a first test of a favorable cost-benefit analysis of the technology for such projects, a case study is conducted. This case study compares the required investment to drill a well with thermal spallation drilling and with conventional drilling methods.

Thereafter, the differences between laboratory experiments and drilling operations in deep bore holes are discussed. The knowledge gained during laboratory experiments is transferred to conditions in a real well. The consequences of this transfer for the applicability of the technology are evaluated. Finally, supply solutions for the reactive fluids, required to establish the flame-jet, are assessed and their applicability is preliminarily discussed. The chapter closes with a recommendation of the application possibilities of thermal spallation drilling in deep wells.

5.1 Cost assessment of thermal spallation drilling¹

An assessment of the cost involved in using spallation drilling is an essential step to evaluate the competitiveness of this technology compared to conventional drilling methods. Only if spallation drilling can compete with conventional drilling methods, it has a reasonable chance to be used in for deep drilling operations. Therefore, the drilling velocity model introduced in Chapter 4.3 is extended in order to estimate the costs, involved in the drilling process as a function of the ROP and well design. As no deep well has been drilled with the spallation technology, the presented cost model has to be understood as an estimate to gauge the competitiveness of thermal spallation drilling in comparison to conventional drilling technologies.

¹This section is based on Kant et al., Proceedings, 41st Workshop on Geothermal Reservoir Engineering [26]

5.1.1 The cost model

The total cost C_t required to drill a specific well comprises of fixed costs C_f , which are independent of depth, time drilled or the progression of the project; time dependent costs C_t , occurring on a daily basis and variable costs C_v , which are a function of the drilled length of the well. The total cost can be calculated, if the individual costs, the required time and the design of the well is known, according to Eq. (5.1) [28, 129, 130],

$$C_t = \sum_{i=1}^I C_{f,i} + \sum_{j=1}^J C_{t,j} \cdot D_{\Sigma} + \sum_{k=1}^K C_{v,k} \cdot L_{\Sigma} \quad (5.1)$$

where $C_{f,i}$, $C_{t,j}$, $C_{v,k}$ are the various cost items mentioned above, D_{Σ} is the total number of days required to construct the projected well and L_{Σ} the total length of the well. The required days for the drilling project is expressed in Eq. (5.2) [28],

$$D_{\Sigma} = D_{prep} + D_d + D_{trip} + D_{cas} + D_{misc} = D_{res} + D_d \quad (5.2)$$

where D_{prep} are the days required before and after the drilling and completion process *e.g.* for rig movement, D_d are the days spent for drilling operations, D_{trip} the days required for tripping, D_{cas} the time spend for running the casing and cementing and D_{misc} days required for other tasks, *e.g.* BHA handling, work over or circulation. The days required for drilling processes can be estimated with the length of the different sections of the well and the corresponding average ROP (Eq. (5.3)) [131].

$$D_d = \sum_{m=1}^M L_m / ROP_m \quad (5.3)$$

Then, the overall costs required for the project can be estimated as shown in Eq. (5.4),

$$C_t = \sum_{i=1}^I C_{f,i} + \sum_{j=1}^J C_{t,j} \left(D_{res} + \sum_{m=1}^M L_m / ROP_m \right) + \sum_{n=1}^N C_{d,m} \sum_{m=1}^M L_m / ROP_m + \sum_{k=1}^K C_{v,k} \cdot L_{\Sigma} \quad (5.4)$$

where $C_{d,m}$ are the daily cost only for the spallation drilling process.

5.1.2 Assessment of the optimal ROP

The cost, specific to the spallation technology, principally are due to the oxygen and fuel compressors and the amount of fluids used. The cost can be divided into fixed costs for renting equipment, which are considered in the total daily costs $C_{t,j}$ and into specific costs $C_{d,m}$, depending on the amount and price of gas and oxidizer, and the energy consumption of the compressors. These specific costs can be assessed, if the required amount of fuel and oxidizer per day is known (see Eq.(5.5)).

$$C_{d,m} = \dot{m}_{fuel} \cdot \sum C_{fuel,spec} + \dot{m}_{oxy} \cdot \sum C_{oxy,spec} = C_{t,fuel} + C_{t,oxy} \quad (5.5)$$

In order to derive the mass flows of fuel and oxidizer, the drilling velocity model presented in Chapter 4.3 of the report can be used. The heat transfer coefficient h_{req} which is required to achieve the target ROP is calculated by solving Eq. (4.29) of the drilling velocity model for the heat transfer coefficient (see Eq. (5.6)).

$$h_{req} = \lambda_R \cdot \frac{\frac{ROP}{\kappa_r} \Theta_{SP}}{\Theta_{FL} \cdot \exp\left(-\frac{ROP}{\kappa} \cdot \Delta x\right) - \Theta_{SP}} \quad (5.6)$$

As already discussed in the Chapter 4.3, the required jet velocity u_f and the heat transfer coefficient h_{req} are connected with Nusselt-correlations and the definition of the Nusselt-number itself (see Eq. (4.34)). Therefore, the correlation proposed by Martin [127] is used

again and solved for the jet velocity u_f as shown in Eq.(5.7).

$$u_f = \frac{\nu_f}{d} \left(\frac{h_{req} d}{0.151 \lambda_f} Pr^{-0.42} \left(D/R \frac{1 - 1.1 D/R}{1 + 0.1(H/D - 6)D/R} \right)^{-1} \right)^{\frac{1}{0.585}} \quad (5.7)$$

Furthermore, the required mass flow to establish a jet with the required velocity can be again calculated as shown in Eq. (5.8).

$$\dot{m} = \rho_f \pi \frac{d^2 \cdot u_f}{4} \quad (5.8)$$

The relationship between days required for drilling and the total mass flow (and therewith the costs) is illustrated in Figure 5.1, as a function of a selected range of rate of penetrations.

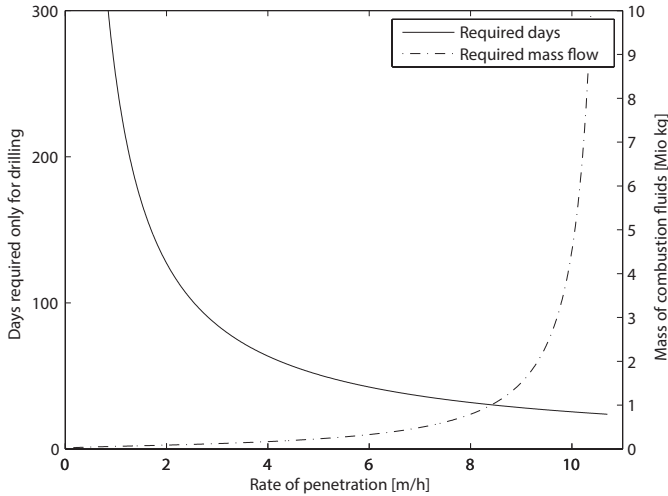


Figure 5.1: Exemplary illustration: days required for the drilling process and total mass of combustion fluids over the rate of penetration, $D_\Sigma = D_d = L/ROP$, $L = 6100m$, $H/D = 3.3$ $r/D = 7.4$, $D = 30\text{ mm}$, $Pr = 0.74$ [128], $\nu = 18 \cdot 10^{-7} m^2/s$ [128], $\lambda_f = 81 mW/(m K)$ [128], $\Theta_{FL} = 1300^\circ C$, $\Delta x = 200 \mu m$ [63], $\lambda_r = 1.8 W/(m K)$ [76], $\kappa_r = 0.7 mm^2/s$ [76], $\Theta_{SP} = 550^\circ C$ (see Chapter 4.1.1)

Obviously, there is an optimum or trade-off between the days required for drilling at low rate of penetrations and the mass flow exponential increase, if high rate of penetrations are selected. The optimal rate of penetration for a specific well can be evaluated, if values for the different introduced cost items are known. Further, if the combustion reaction is known, the individual mass flow components (fuel and oxidizer) can be calculated with the required fuel ratio Φ_{fuel} (Eq. (5.9)-(5.10)).

$$\dot{m}_{fuel} = \Phi_{fuel} \cdot \dot{m} \quad (5.9)$$

$$\dot{m}_{oxy} = (1 - \Phi_{fuel}) \cdot \dot{m} \quad (5.10)$$

Therewith, the specific costs for methane and oxygen can be calculated on a daily basis as shown in Eq. (5.11)-(5.12) with the mass flow in the units $[kg/d]$,

$$C_{t,fuel} = \Phi_{fuel} \cdot \dot{m} \cdot \sum C_{fuel,spec} \quad (5.11)$$

$$C_{t,oxy} = (1 - \Phi_{fuel}) \cdot \dot{m} \cdot \sum C_{oxy,spec} \quad (5.12)$$

where $\sum C_{fuel,spec}$ and $\sum C_{oxy,spec}$ are the sums of the specific fuel and oxidizer costs in USD/m^3 , composed of costs for the fluids themselves and flow specific pumping costs.

With this assessment the total costs can be expressed as shown in Eq. 5.13.

$$C_t = \sum_{i=1}^I C_{f,i} + \sum_{j=1}^J C_{t,j} \cdot \left(D_{res} + \sum_{m=1}^M L_m / ROP_m \right) + \sum_{m=1}^M (C_{t,fuel} + C_{t,oxy}) L_m / ROP_m + \sum_{k=1}^K C_{v,k} \cdot L_{\Sigma} \quad (5.13)$$

5.1.3 Case study with the derived cost model

In order to apply the cost model and to enable a comparison of the spallation technology with conventional drilling methods from a costs perspective, the well design and the connected cost reported by Polsky

et al. [28] have been selected and applied to the introduced model. This report was conducted together with ThermaSource, a major geothermal consulting and drilling provider. It discusses the required investment for a 6100m deep geothermal well with 5 different sections and a final production liner diameter of 7 inches (Fig. 5.2). The report is based on conventional drilling. Nevertheless the detailed costs structure of this report can be applied with some modifications to the spallation technology, as most of the equipment and processes are needed for both technologies. Further information about the design and the costs for this project with conventional drilling methods can be found in the mentioned report [28].

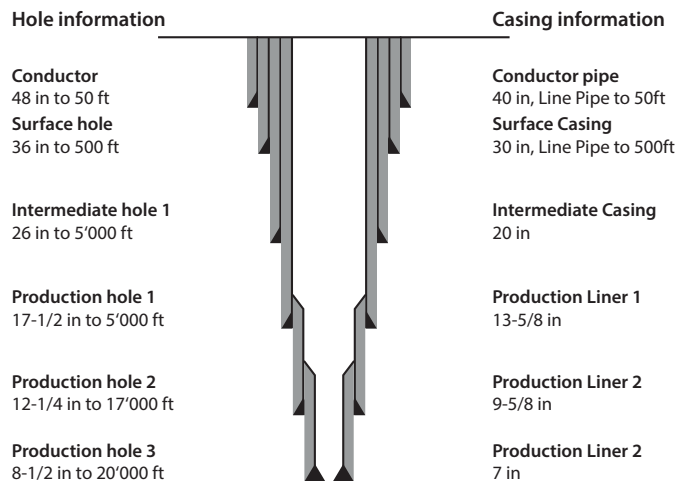


Figure 5.2: Design of the investigated well. Figure adapted from Polsky *et al.* [28]

In order to compare the cost structure presented by Polsky *et al.* [28] with the model introduced above, a spallation tool is used, driven with a stoichiometric methane-air mixture, a single nozzle with a constant diameter and producing a flame temperature of 1300°C. To simplify the model, it is assumed that this spallation drill head drills with a constant ROP from surface to the bottom of the well. Further, the same hard formation with constant rock properties is present from the surface to

the end of the well. The methane price was estimated using a five-year average of the natural gas prices in the US, air was assumed to be extracted from the surroundings at no costs. The compression costs were estimated from a suggestion published by the British Compressed Air Society [132]. The impact on cost, due to the required adaptations of the equipment from conventional drilling to spallation drilling, is considered and listed in detail in the cost tables (see Appendix C). Reduced values are assumed for the following positions:

- required fuel of the rig (not including the fuel for the combustion), due to lower WOB and torque (1000 gal/day instead of 2500 gal/day).
- number of bits required for a section, due to significant lower wear-rates (1 instead of 3-6 bits per section).
- days required for tripping operations, due to lower wear-rates (10 instead of 31.4).

Higher costs are assumed for the following positions:

- the day rate of the rig (30.000 USD/day instead of 28.000 USD/day)
- single drill bits (30% more)
- drill pipes (300 USD/day instead of 150 USD/day)
- BOP rental, top drive rental, monitoring system, safety and misc. (see table A.3).

New cost positions are introduced for:

- fuel compressors and storage (combined 3000 USD/day)
- fuel consumption ($0.25 \text{ USD}/m^3$)
- air compressors (2000 USD/day)
- costs for compression of the fluids ($0.05 \text{ USD}/m^3$ for each fluid)
- top drive modifications (1000 USD/day) and safety procedures (500 USD/day)

Table A.2-A.5 in Appendix C lists the single cost positions of the conducted drilling project, based on the data of Polsky *et al.* [28]. The fixed costs are expenses, which occur to establish the drill site, to move the rig, for equipment, insurance and contracting services (Table A.2). The daily rates are composed of costs for rig rent, tool rent (including special spallation equipment), labor expenses and other services (Table A.3). They will be significantly influenced by a fast and efficient drilling process. Table A.4 lists the variable costs which are a function of the well length as *e.g.* casing and cementing materials. These costs have not been modified from the values suggested by Polsky *et al.* [28]. Additionally, the assumed time schedule for the project is listed in Table A.5, also based on Polsky *et al.* [28]. For a better overview over this case study, the single cost components used in Eq. (5.13) are highlighted in Table 5.1.

Table 5.1: Summary of the different applied cost components (details can be found in Appendix C) and comparison with conventional drilling methods, according to Polsky *et al.* [28].

Cost component	This report	Polsky <i>et al.</i>
Fixed costs	5,273,900 USD	5,669,000 USD
$\sum C_{f,i}$		
Daily costs	82,850 USD/D	77,250 USD/D
$\sum C_{t,j}$		
Var. costs	4,294,400 USD	4,294,400 USD
$\sum C_{v,k} L_{\Sigma}$		
Spec. fuel costs	0.35 USD/ m^3	dna
$\sum C_{t,fuel,spec}$		
Spec. air costs	0.05 USD/ m^3	dna
$\sum C_{t,oxy,spec}$		
Req. days w/o drilling	60.2	81.6
D_{res}		

This cost structure is integrated into the presented cost model and the optimal ROP is analyzed (Fig. 5.3). It can be seen that on the one hand costs increase rapidly with low ROPs. As only insufficient progress is made in the drilling process, the day rates dominate the cost structure of the projects, which leads to a significant increase of the overall costs.

On the other hand, if too high ROPs are selected, the overall costs will rapidly increase. This effect is attributed to the excessive amount of methane and air required to achieve the demanded heat transfer coefficient. Between these two extreme values a minimum of the total costs of 19 Mio. USD at an ROP of about 6.5 m/h can be found, which is a reasonable value for thermal spallation drilling, as shown by Hoeser [63]. The calculated costs are 10% lower than the costs for the report of Polsky *et al.*, which were estimated to sum up to 21.3 Mio. USD [28]. Thereby, the cost reduction is mainly attributed to the time saved during the tripping processes (assumed with a third of the days as with conventional drilling) or non-productive time. The combustion fluid costs are responsible for only 2 Mio. USD at the optimal operating point, therefore being of only minor importance in the overall cost structure. This behaviour is also visible in the flat profile of the minimum in the cost analysis (Fig 5.3). Changes in the ROP, in the range between 2-9 m/h, due to *e.g.* other burner configurations, only have a small influence in the total investment for the drilling project. In conclusion, the model shows that major cost savings can be achieved with reduced tripping efforts, whereas high ROPs are ineffective. Therefore, the development of thermal spallation tools should focus on the postulated low wear rates of the heads, to achieve the required reduction of tripping times.

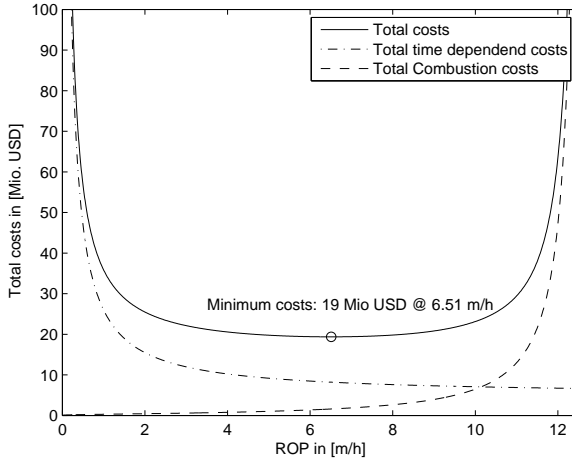


Figure 5.3: Total costs for the selected well drilled with spallation drilling for different ROPs, see Table 5.1 or Appendix C for the different cost components, other applied parameters: $D_y = D_d = L/ROP$, $L = 6100m$, $H/D = 3.3$ $r/D = 7.4$, $D = 30mm$, $Pr = 0.74$ [128], $\nu = 18 \cdot 10^{-7} m^2/s$ [128], $\lambda_f = 81 mW/(mK)$ [128], $\Theta_{FL} = 1300^\circ C$, $\Delta x = 200 \mu m$ [63], $\lambda_r = 1.8 W/(mK)$ [76], $\kappa_r = 0.7 mm^2/s$ [76], $\Theta_{SP} = 550^\circ C$ (Chapter 4.1.1)

It has to be highlighted that the presented model should be understood as a preliminary investigation. Many cost positions had to be estimated, as no experience or empirical values with spallation tools in such an environment are currently available. Additionally, significant simplifications have been used to derive cost structure: the applied model itself is simplified, the compressor costs do not account for the pressure drops along the drill string, which will occur at high ROPs. Additionally the cost structure for such high pressure equipment (over 600bars for a well of a length of 6000m) might change. Further, failure and problems during the use of the novel spallation tools are not considered and the diameter of the nozzle was considered as constant.

5.1.4 Conclusions

The presented drilling velocity model was expanded to be able to estimate the costs involved in a thermal spallation drilling project. The performed cost analysis shows that spallation drilling can be used at competitive cost compared to conventional technologies and a reduction of the overall cost is possible. The cost savings are mainly attributed to the assumed time savings during the tripping process, as the spallation technology might reduce the wear rate of the components. Other cost reductions as *e.g.* due to faster ROPs or reduced power input from the top drive do not significantly reduce the cost structure.

5.2 Drilling at great depths

So far in this report a modeling approach has been developed to evaluate whether certain rock formations can be successfully spalled. Additionally, another model is presented, estimating the maximal drilling velocity for a specific rock-burner combination. Further, spallation has the potential to reduce the drilling cost by 10-20%, a number of important issues seem to be clarified and the applicability and efficiency of thermal spallation drilling has been shown in laboratory environments at ETH Zurich [63] and in shallow drilling applications with depths up to 311m by other researches [55, 58]. A scale-up to a pilot field test at great depth can now be explored in a conceptional manner. In the following, the most important differences between drilling experiments in a laboratory environment and in real drilling applications are discussed, together with the consequences for the applicability of thermal spallation drilling.

5.2.1 Non-spallable rocks

Although basement formations are composed of mainly of hard and spallable rock sections, non-spallable inclusions or sections cannot be excluded. In order to investigate the influence of such rock types on spallation drilling, the stress field induced by a spallation drill head is evaluated. An exemplary selected spallation drill head is selected, excavating a 6.5 inch borehole and reaching a non-spallable inclusion (rock

properties of a typical sandstone) in the hard rock formation (rock properties of a typical granite). The rock structure was modeled in COMSOL Multiphysics, as a homogeneous block with a size of 1.5m x 1.5m with a fixed constrained applied to every outside edge (Fig 5.4 (a)). The flame was modeled with a constant temperature (600°C), acting on the end of the 6.5 inch borehole embedded in the middle of the rock block. The temperature at the edges of the domain was kept constant at 20°C . Fig. 5.4 (b) shows the resulting stress field for a steady-state simulation of the discussed domain. It can be seen that the stress field around the bottom of the borehole is asymmetric, as the stresses in the non-spallable section are considerably lower than in the hard formation (*e.g.* 33% lower at two selected points (see Fig. 5.4 (b))).

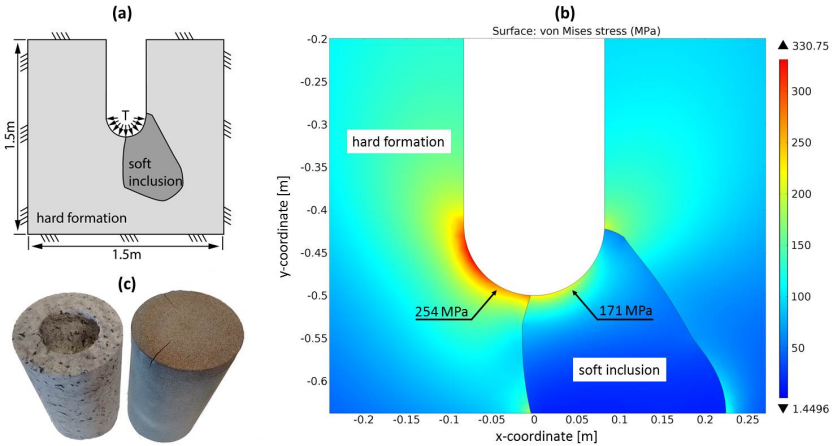


Figure 5.4: (a) Schematic of the modeled domain. (b) Illustration of the effect of a soft intrusion on the thermal stress field in a simulated bore hole, applied parameter: hard formation: $E = 45 \text{ GPa}$, $\nu = 0.25$, $\rho = 2500 \text{ kg/m}^3$, $\alpha = 8 \cdot 10^{-6}$, $\lambda = 3.2 \text{ W/(m K)}$, $c_p = 800 \text{ J/(kg K)}$, soft formation: $E = 10 \text{ GPa}$, $\nu = 0.18$, $\rho = 2400 \text{ kg/m}^3$, $\alpha = 8.29 \cdot 10^{-6}$, $\lambda = 2.6 \text{ W/(m K)}$, $c_p = 830 \text{ J/(kg K)}$. (c) Picture of spallable Central Aare granite and unspallable Rorschacher sandstone.

Already such small non-spallable intrusions can slow down the spallation process. As the stresses are higher in the hard rock formation, it will spall faster, exposing new rock material more quickly and finally de-

flecting the bore hole away from its desired trajectory. This leads on the small scale to bore hole irregularities, potentially causing stuck pipe and cementing issues and on the large scale to the loss of direction control. Additionally, if the unfavorable properties are not only present in a small inclusion but over a whole section, a spallation drill head would need to be exchanged with a mechanical drill head, which will drill the non-spallable sections with conventional rock excavation methods until the process could continue with spallation again. Unfortunately, lengths and frequencies of non-spallable sections are unknown. Therefore, this exchange does not represent an acceptable solution. In conclusion, soft non-spallable rock materials embedded in the basement formation imply a significant limitation for the application of thermal spallation in a deep drilling project. The practical relevance of this concise analysis is illustrated in Fig. 5.4 (c), which shows Central Aare granite and Rorschacher sandstone after ambient spallation experiments. Whereas in the granite sample a cavity could be excavated, only large fractures are visible on the surface of the sandstone, which originate from circumferential stresses, due to uneven heating of the surface with a localized flame jet.

5.2.2 Stress relieving fractures

Solid and compact rock samples used in the laboratory experiments are not representative of the structures of rocks at great depths. Natural fractures present in the formation will relieve the stresses and open flow paths (see Figure 5.5 (a)). These fractured zones are the target for geothermal reservoirs, as they usually have higher temperatures, higher fluid flows and can be further stimulated to increase the production rate [8]. In order to investigate the influence of these fractures on the spallation process, a similar thermo-mechanical analysis, as discussed above, was performed. The stress field induced by a spallation drill head excavating a 6.5 inch borehole is evaluated for a rock structure (same granitic formation as in Chapter 5.2.1) without fractures and a rock structure with a single large fracture with a simplified rectangular shape, an aperture of $500\text{ }\mu\text{m}$ [133] and a length of 20cm. The spallation process is again modeled by a temperature boundary condition of 600°C , acting on the end of the borehole embedded in the middle of the rock block (Fig.

5.5 (b)). If no fracture is present (Fig. 5.5 (c), solid line), a homogeneous and sufficient stress field can be induced by the temperature boundary condition. The fracture relieves the stresses ((Fig. 5.5 (c), dashed line) and a lower and inhomogeneous stress field is present close to the well bore. Only in the near field of the crack, the stresses are higher, due to stress intensity effects. As the thermal stresses are insufficient for spall creation, the spallation process will stop.

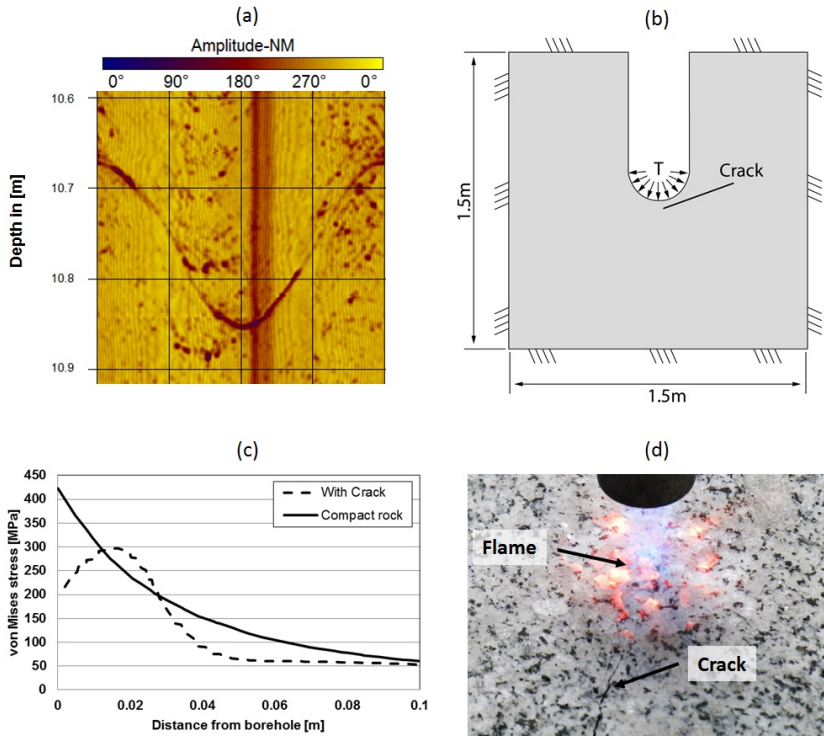


Figure 5.5: (a) Unwrapped amplitude plot of a crack from an acoustic televiewer log performed in the TSD-17.001 borehole in the Grimsel Test Site. (b) Illustration of the modeled domain. (c) Stresses along the vertical centerline of the domain, starting at the end of the bore hole. (d) Picture of a large crack, which led to the stop of the spallation process.

This can also be observed in ambient spallation processes (see Figure 5.5 (d)). If a rock is exposed to a flame jet, without any confinement, the rock will crack pervasively, relieving all the thermal stresses and the spallation process will stop already seconds after it has been initiated. The consequences on deep drilling operations are the same as for non-spallable intrusions and sections (Chapter 5.2.1): small cracks will lead to a deflection of the drill head away from its projected trajectory. Large cracks will lead to a stop of the spallation process and a change-over to a mechanical drill bit is unavoidable. In conclusion, fractures present in the rock structure imply an additional limitation of the spallation technology in deep drilling projects.

5.2.3 Significant intrusion of fluids

Entrainment of dense fluids into the flame front leads to significant heat losses of the flame-jet before the energy can be transferred to the rock [41, 51, 73, 134]. Due to the large density differences between cold fluid and the hot combustion products, the flame-jet will be compressed into a small, pin-shaped flame. A significant share of energy is lost to water and only insufficient heat is transferred to the rock surface (Fig. 5.6 (a) and (b)) [41]. In order to prevent this, dynamic sealing devices are used during thermal spallation drilling in an aqueous environment. They shield the combustion zone from entrainment and keep the fluids above the drill head. Nevertheless, if a certain amount of formation fluids intrudes from the formation into the bore hole end or the sealing devices fails, (*e.g.* due to irregular bore hole walls or breakouts [135]), the gas-like state in the treatment zone cannot be sustained anymore, an insufficient temperature is induced on the rock surface and the spallation process stops.

The influence of entrainment of spallation drilling can be visualized in a concise thermodynamic consideration. Assuming that the exhaust gases act like an ideal gas and the energy transfer between the fluids can be described by a perfect mixing process, a simplified energy balance for the heat transfer between the two fluids is possible (see Figure 5.6 (c)). The hot exhaust gases leave the nozzle with the combustion heat Q_{fl} , travel through the water-filled control zone, where they lose energy to

the water by entrainment \dot{Q}_{entr} and finally impinge on the target, where the rest of the heat is transferred by convection \dot{Q}_{target} .

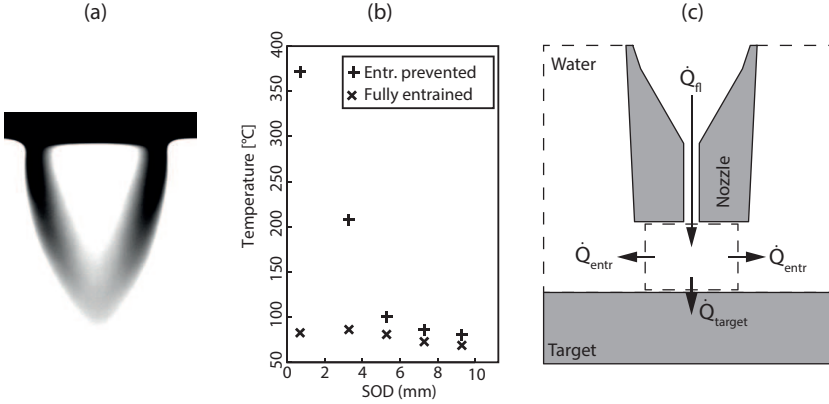


Figure 5.6: (a) Frosted Glass Oriented Schlieren (FGOS) picture of an entrained supercritical fluid jet (courtesy of M. Schuler [41]). (b) Axial temperature profile of a submerged methane air jet with entrainment prevented and completely entrained. (c) Energy balance between burner, target and cold dense water around the burner.

If the water completely entrains the flame-jet, the whole flame energy is lost to the water and no heat can be transported to the target $\dot{Q}_{target} = 0$. The flame will be cooled down from *e.g.* 1000°C to the boiling temperature of the water (100°C) and the water will be heated up from *e.g.* 20°C to also 100°C and completely evaporated (Fig 5.6 (b)). In this scenario, a simple energy flow equation, as depicted in Eq. (5.14), can be used to describe the entrainment issue,

$$\underbrace{\dot{m}_{fl} \bar{c}_{p,fl} \Delta T_{fl}}_{\dot{Q}_{fl}} = \underbrace{\dot{m}_{H_2O} (\bar{c}_{p,H_2O} \Delta T_{H_2O} + \Delta h_v)}_{\dot{Q}_{entr}} \quad (5.14)$$

where \dot{m}_{fl} is the mass flow of hot gases leaving the nozzle, $\bar{c}_{p,fl}$ the mean heat capacity of the gas and ΔT_{fl} the temperature difference. The same nomenclature applies for the water, whereas \dot{m}_{H_2O} is the required flow of water to completely cool down the flame-jet and Δh_v the enthalpy of evaporation. Using the temperature values mentioned above and taking

the physical properties of air at 1 bar, the required flow of water to completely cool down the hot gases can be calculated, as shown in Eq. (5.15).

$$\dot{m}_{H_2O} = \dot{m}_{fl} \frac{1.1 \text{ kJ}/(\text{kg K}) 900 \text{ K}}{(4.2 \text{ kJ}/(\text{kg K}) 80 \text{ K} + 2260 \text{ kJ}/\text{kg})} = 0.38 \dot{m}_{fl} \quad (5.15)$$

According to Eq. (5.15), about three times less mass of water has to entrain into the hot jet to completely cool down the gas to an insufficient temperature level of 100°C .

If a 20 kW oxygen-air flame ($\dot{m}_{CH_4} = 0.36 \text{ g/s}$, $\dot{m}_{O_2} = 1.44 \text{ g/s}$) is considered, a total water mass flow of only $\dot{m}_{H_2O} = 0.68 \text{ g/s}$ is required to cool down the flame-jet. This corresponds to a water volume of 0.68 mL of water, which has to penetrate the hot fluid jet per second. A few drops of water are enough to completely cool down the flame. In conclusion, as impinging fluid jets are characterized by excellent mass- and heat transfer properties [73, 134], intrusion of small amount of fluids into the bore hole is already sufficient for the spallation process to stop, which would lead to an interruption of the drilling process, with the same consequences as previously discussed.

5.3 Supply of the reactive fluids

Whereas the required fluids to establish the flame jet can be easily supplied to the burner in laboratory experiments, special solutions are required for deep drilling applications. In principle, three options are conceivable (Fig. 5.7): transport of the fluids via triple drill strings or a coiled tubing system [61, 62] from the top drive to the drill head, storage in tanks integrated in the BHA or down hole electrolysis of oxy-hydrogen from the drill mud. All options should aim to minimize the necessary adaptations from conventional drilling technologies, reducing the investment cost required to use the spallation technology and facilitating the work with these novel tools. On the one hand, transportation from surface allows for better control possibilities, but on the other hand, this mode requires also significant adaptations of equipment (*e.g.* the drill string and the top-drive). Storage of the fuel in the BHA only requires

modifications of the BHA itself, if communication via wireline or mud pulse telemetry were possible. Down hole electrolysis is the most difficult solution and requires high pressure equipment and thus this option is not discussed further. In this section of the thesis, the applicability of the first two options in deep drilling operations will be shortly evaluated.

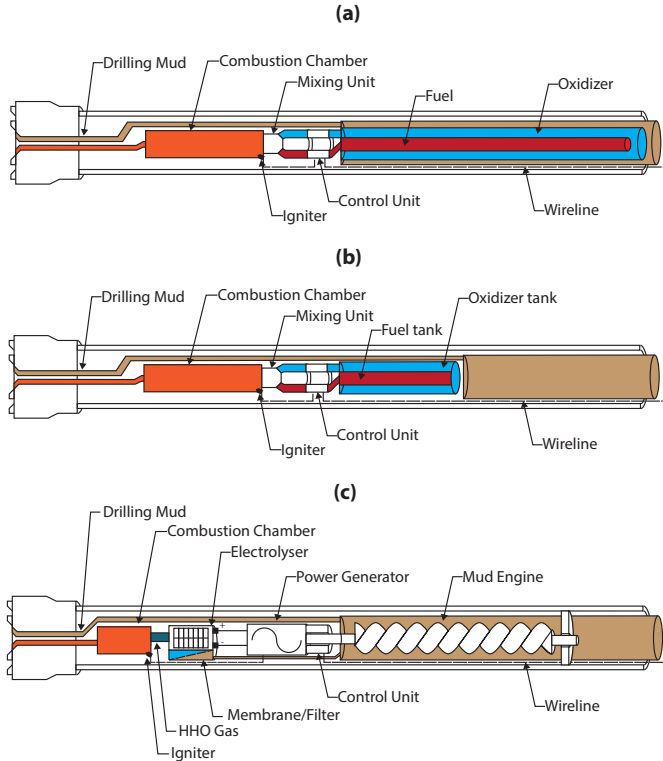


Figure 5.7: Possible supply concepts for a thermal spallation drilling head

5.3.1 Transport via drill string or coiled tubing

If the fluids are transported via the drill string by using double or triple drill pipes [61, 62], hundreds of these special drill pipes have to be con-

nected to each other to reach the bottom in several kilometers depth. Additionally, the supplied fluids are highly pressurized, as for deep bore holes (*e.g.* 5km) pressures of 500-1000 bar are typical [136, 137]. Due to the amount of required connections and the high pressure setting, a potential of leakage is present. Additionally, failure of the drill string, due to twistoff, parting or fatigue is a common problem in drilling operations [138–140]. Both cases would release large amounts of combustion gases into the well bore, which could flow back to the surface and ignite. Therefore, the use drill pipes for the supply of the fluids depicts a significant safety concern and seems to be an unsuitable option.

Another solution is to supply the fluids via a coiled tubing system, which does not has connection threads along its length. Therefore, this solution seems to be more applicable for thermal spallation drilling than the use of drill pipes. Nevertheless, even though coiled tubing systems are used since decades, it is still considered an immature new technology, as several issues remain, *e.g.* performance in deviated wells, effective cutting transport and limitations in the maximum depth [141–144].

5.3.2 Storage in the BHA

In order to store the fluids down hole, storage capacities have to be provided inside the BHA. As space is limited in the radial direction, due to the confined placement inside the bore hole, the tanks have to extend into the axial direction. Table 5.2 shows the resulting required tank length for an exemplary selected downhole combustion process of 50kW over 48h. The tanks are assumed to have a storage pressure of 500 bar and a half circle base area with a diameter of 12 1/2 inches. It can be seen that for all solutions long tanks are required, which have about the same length as a normal BHA (typically 50-100m long (or larger for special BHAs) [145–147]). If the fluids are stored liquefied, the energy density can be increased and the required tank can be reduced to half of the required length. In conclusion, already for a drilling operation over a 48h period, very long storage tanks are required. Nevertheless, in order to use the whole advantages of spallation drilling and to reduce the tripping efforts, longer consecutive drilling periods are necessary. This would lead to storage solutions, which are difficult to provide.

Table 5.2: Summary of different investigated reactions and the required down hole storage capacity to maintain a 50kW flame over 48h. Tanks have a half circle base area with a diameter of 12 1/2 inches

Fuel & oxidizer	Req. length fuel tank [m]	Req. length O_2 tank [m]
Methane, compr., 500bar	56	
Oxygen, compr., 500 bar		100
Methane, liquefied	37	
Oxygen, liquefied		55
Ethanol, liquid	36	
Oxygen, liquefied		53

5.4 Conclusions of this chapter

The presented cost study shows that thermal spallation drilling has the potential to reduce drilling costs. The most significant savings can be achieved by reducing tripping times. High drilling velocities do not improve the cost structure, as savings are compensated by increased costs for fuel and compression efforts. Thermal spallation drilling performs well under laboratory conditions, if homogeneous and favorable rock conditions are encountered. Nevertheless, significant limitations pose challenges to the applicability of spallation drilling in the field. Non-spallable rock sections, stress relieving fractures and intrusions of water into the borehole will stop the spallation process. The required temporal change to an mechanical bit is not only time-consuming, but also works against most of the discussed benefits of this technology. Additionally, the supply of the reactants implies further difficulties. This leads to the conclusion that spallation drilling is not applicable for drilling long wells in an unknown rock formation. Nevertheless, solutions to overcome these problems and alternative application possibilities exist, which will be discussed in the following two chapters of this thesis.

CHAPTER 6

The hybrid drilling project

The general applicability of thermal spallation drilling has been shown under laboratory conditions in Chapter 1-5 of this thesis and by Hoeser, Meier and Stathopoulos [51, 63, 103]. But solid and compact rocks used in these experiments cannot be guaranteed in field drilling applications over a long distance. As discussed in Chapter 5.2, non-spallable rock sections, highly fractured zones or intrusion of water into the combustion zone impede the spallation process, which would require an alternating excavation with conventional mechanical drilling tools. This exchange would vanish most of the discussed benefits of the technology. In order to solve this issue, a combination of spallation drilling and mechanical drilling seems to be appropriate for deep drilling operations. If a drill head works with a combination of both drilling principles, some of the limitations may be overcome.

In the following chapter, first the principles of such a combined drilling method are assessed together with its potential benefits. In order to show the general feasibility of a thermo-mechanical drilling system, a first study by means of thermal treatments is conducted and implementation possibilities are discussed. The applicability of a hybrid system is shown in a full-scale hybrid drilling system, designed in cooperation with the Geothermal Center in Bochum (GZB). The design aspects of this system are discussed and the drill head is preliminary tested, indicating the operational readiness of the system.

6.1 Combined drilling process¹

In a combined system, the hot fluid jet can be used to spall the rock or to thermally weaken the structure. If the rock properties are favorable for spallation, a combined system excavates the rock with the introduced thermal spallation process (Fig. 6.1 (a)-(c), (d1)-(e1)). If the rock cannot be spalled, due to unfavorable rock properties, the flame jet can be used to further weaken the rock. This thermal treatment leads to a decrease of the rock strength, due to severe crack creation (d2) [76]. The cracked surface can then be excavated with conventional mechanical cutters (e2), whereas less weight on bit and torque is needed, as the bit requires less

¹This section is based on Kant et al., 41st Workshop on Geothermal Reservoir Engineering, Stanford[148]

energy to break the already fractured rock.

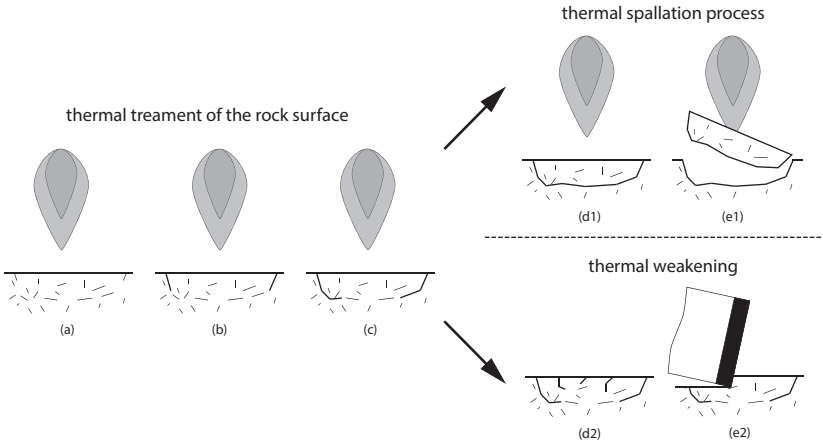


Figure 6.1: Principles of a thermo-mechanical drilling process. Common process: (a) initially present cracks, (b) crack initiation, (c) crack growth. Spallation: (d1) spall formation, (e1) spall ejection. Thermal weakening: (d2) further cracking of the surface, (e2) mechanical excavation of the cracked surface.

Fig. 6.2 shows an illustration of a design suggestion for a hybrid drilling system, combining thermal and mechanical drilling. The hot combustion gases are created in an internal combustion chamber. The flame jet is then directed to a flame slot on the front face of the drill head, where mechanical cutters are additionally placed. The combustion chamber and the remainder of the system is cooled with conventional drilling mud, keeping the temperature at an acceptable level. The flame assistance must be confined to a certain area to avoid thermal wear of the mechanical cutters. On the other hand an efficient heat transfer has to be provided and entrainment of cold drilling mud into the hot treatment zone [134] has to be limited to an acceptable level. The efficiency of an air shield around the flame for this purpose is discussed in Section 6.3. Additionally, a mechanical load concept has to be integrated, which transfers the load to the mechanical cutters and avoids load on the thermally stressed flame slot.

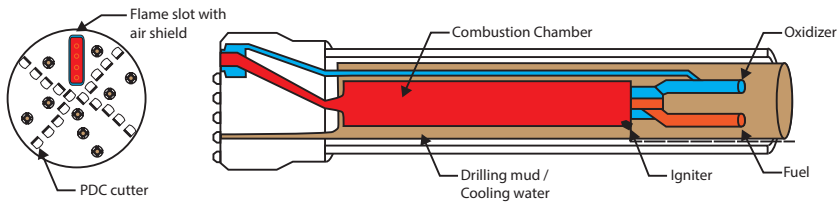


Figure 6.2: Illustration of a hybrid drilling system combining conventional rotary drilling and thermal spallation drilling

Besides the advantage that a combined process makes the spallation technology applicable in deep drilling projects, other benefits arise potentially by combining mechanical and thermal spallation drilling. Due to the generally reduced strength of the rock structure after a thermal flame treatment, less weight on bit is required, which enhances the efficiency of the drilling process and reduces the wear rate. The principles of such a rock weakening process are investigated in the next section of this chapter. Additionally, up to now, PDC cutters only perform in soft and medium hard formations. In extreme hard formations PDC cutters will overheat and wear out fast [34, 35]. In a combined system, the flame has the potential to sufficiently decrease the rock strength to a comparable value as the soft formation's strength. Therewith, a combined system could enable the application of PDC-cutters also in hard-rock formation, reducing the required tripping efforts, intensifying the drilling technology and improving the overall drilling efficiency.

6.2 Thermal rock weakening

In order to show in a first preliminary stage, the applicability of such a combined drilling process, results of two experimental sets, combining flame weakening and mechanical excavation, are reported in this section of the thesis.

6.2.1 Preliminary experiments

For the first investigation, a drilling machine, equipped with a diamond cutting tool, penetrated rock samples of Rorschach sandstone and Central Aare granite, which had undergone a thermal treatment in an oven or with a flame. These rock types were selected, as Central Aare granite has shown excellent spalling behaviors (Section 4.2), whereas Rorschach sandstone appears to be not spallable (Section 5.2). Rorschach sandstone is a calcite-cemented sandstone, with a fine and homogeneous grain-size distribution, ranging from 0.05mm to 0.5mm [149].

The drilling process was controlled by keeping the axial force on the drill constant, adjusting a constant rotational speed and drilling for a fixed time. The influence of the thermal treatment on the drilling process can then be monitored by the variation in the rate of penetration, calculated with the drilled time and the depth of the created hole. Before the different thermal treatments were performed, one initial hole was drilled in every sample to obtain a reference value.

For the oven treatments, a constant heating rate of $10^{\circ}\text{C}/\text{min}$ was adjusted and after the rock samples have reached the required temperature, the value was hold constant for 60 min to homogenize the temperature distribution inside the rock sample. Thereafter, the samples were removed from the oven and cooled down to room temperature for several hours.

Fig. 6.3 (a) shows the results of these oven treatments. Both materials follow the same trend: after an initial decrease in the rate of penetration, due to hardening reactions [150–152], the rate increases exponentially with temperature. If a certain temperature is reached, the induced thermal stresses are sufficient that the fracture toughness is locally exceeded and cracks are created [106–109]. These cracks weaken the rock structure and therewith facilitate the subsequent drilling process [153, 154].

Thereby, a performance increase was monitored for temperatures above 800°C for sandstone and 400°C for granite. Most probably, the α - β phase transition of quartz, appearing at 573°C [121], contributes to this performance improvement. For both materials, an increase in the rate of penetration of a factor of 4 at a temperature of 900°C and 1000°C could be observed. Fig. 6.3 (b) shows a sandstone sample several days after the experiment. It can be seen that the structure is disintegrated and the slightest contact leads to a collapse of the sample.

As a next step in the verification process of a combined system, a flame torch impinged orthogonally on the rock samples. After the rock surface was treated for a specific time, the burner was removed and the drilling process immediately started. It has to be highlighted that, due to the weak flame, the reported treatment times do not represent a realistic value for a future application of a combined drilling system. Fig. 6.3 (b) shows the results of this experiment, with a similar trend as the oven treatments. After a certain treatment time is exceeded, the rate of penetration increases with temperature. But, whereas the sandstone still shows an initial decrease of the drilling performance, no hardening effect is visible for the granite samples. The fast heating rate of the flame treatment could successfully suppress the slow hardening reactions of the granite [149]. Recent research of Rossi *et al.* [149] showed that also the hardening reaction of sandstones can be suppressed with higher heating rates, exceeding $5^{\circ}\text{C}/\text{s}$.

This truly simple experiment shows that the flame has the potential to decrease the strength of rock materials and a combined thermo-mechanical drilling system could potentially lead to higher penetration rates and less required weight on bit also in non-spallable rock sections.

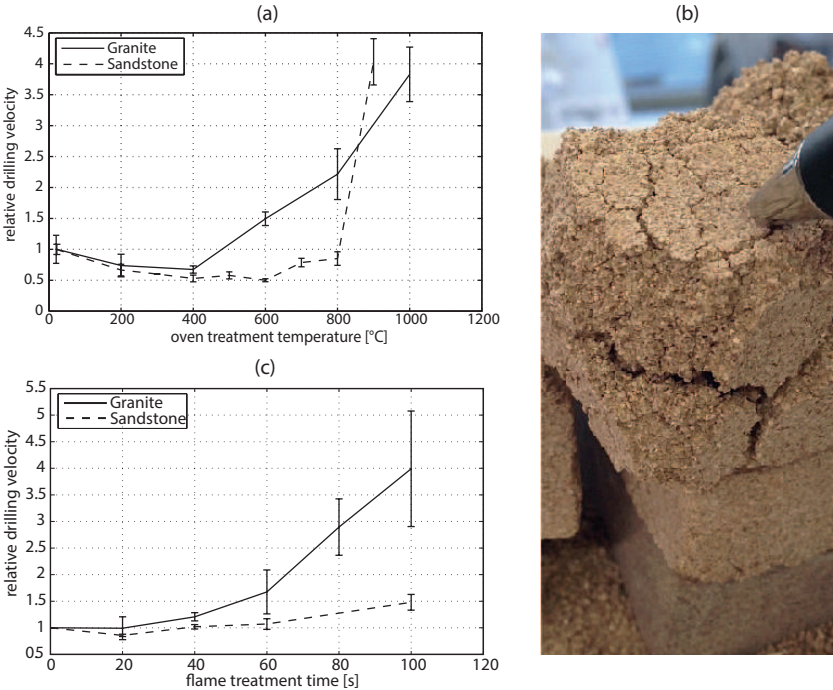


Figure 6.3: (a)Relative drilling velocity as a function of the oven temperature. (b) Disintegrated sandstone samples, several days after heating to 900°C. (c) Relative drilling velocity as a function of the time, which the samples are exposed to the flame.

6.2.2 Strength analysis²

In order to further investigate the effects of thermal rock weakening of rock materials, a second study was performed. For the flame treatments, a methane-air burner with a flame temperature of approx. 1300°C was used to locally heat up the rock surface to about 400°C . Here, the rock samples were translated relative to the flame burner, which is placed perpendicularly to the sample moving direction [149]. During the treatments, the surface temperature of the samples was measured with an infrared pyrometer (see Chapter 4.1.1.2) focused on the stagnation point of the flame. The samples were cooled down after the flame treatments under ambient conditions. The oven treatment were similarly performed, as discussed in the section above. Central Aare granite and Rorschach sandstone were used again for this investigation. Before and after the experiments, the rock samples were tested with the scratch test method developed and performed by the company EPSLOG [155, 156]. This test uses a PDC-cutter to export material, creating a 10 mm-wide groove with different cutting depths, while measuring the applied forces on the tool. With the measured forces the strength of the material can be calculated [156, 157]. This techniques also allows a high resolution mapping of the actual material structure and the strength variation along the excavated groove. Since the effect of flame treatments on the material strength must be assessed at the rock surface, conventional strength testing techniques such as the UCS test would not be able to describe the occurring localized phenomena in detail. Further, this experimental method shows a certain consistency with the investigated drilling technique.

Fig. 6.4 shows the strength variation along the groove before and after an oven treatment. Thereby, the rock cores were scratched before the test (baseline), thermally treated and scratched again in the same groove (after the oven treatment). It can be seen that after the treatment the color of the material has changed, due to alteration processes *e.g.* oxidation of the minerals [158]. Additionally, the strength after the treatment could be considerably reduced.

²This section is based on Kant et al., 41st Workshop on Geothermal Reservoir Engineering, Stanford [148]

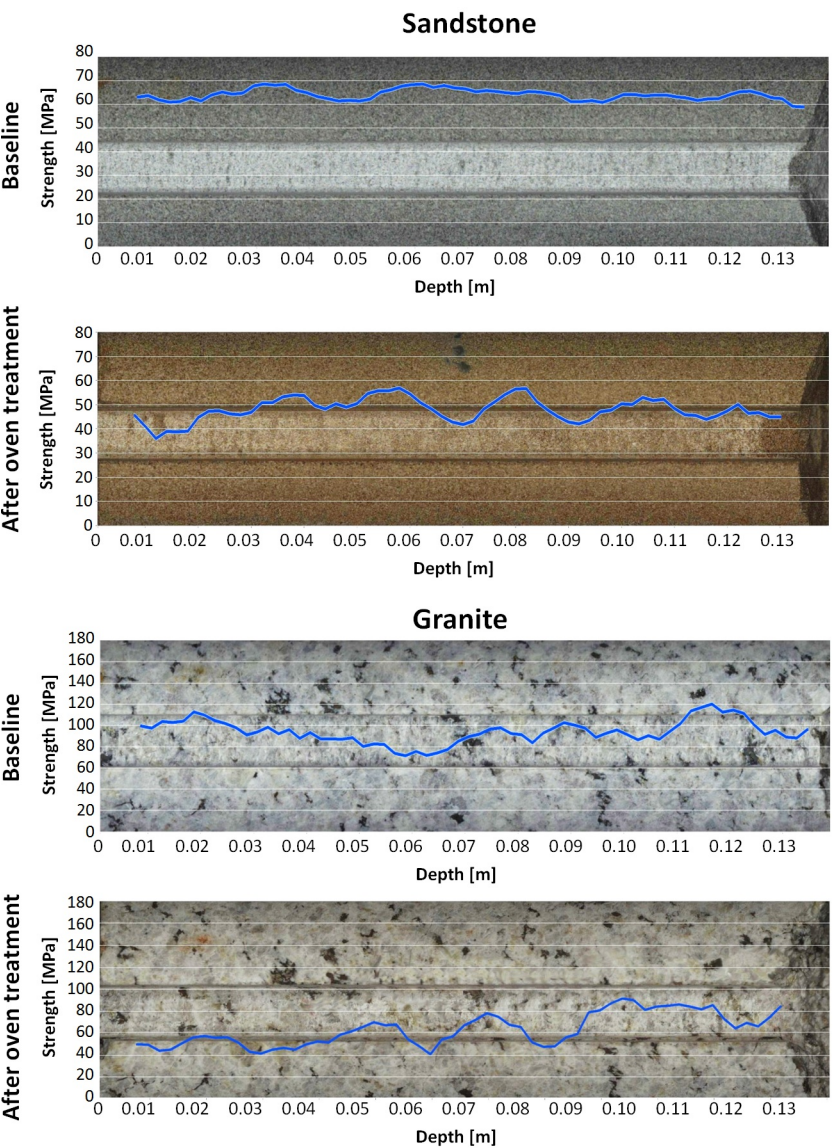


Figure 6.4: Variation of the strength along the length of the scratched samples. Top: Sandstone samples before and after the oven treatment. Bottom: Granite samples before and after the oven treatment. Note the different scales of the granite and the sandstone profiles and the color changes of the rock materials after high temperature thermal treatments.

Further treatments were performed with temperatures ranging from 20°C up to 800°C for sandstone and granite samples. The results of these experiments are shown in Fig. 6.5 (a). Here, the strength reduction is plotted against the reached treatment temperature at the sample surface. The strength of the untreated material, obtained by the scratching procedure explained above, was 105 MPa and 64 MPa for granite and sandstone samples, respectively. The reported strength values are the mean values together with their standard deviation of the window-based filtered data shown exemplary for the oven treatment in Fig. 6.4.

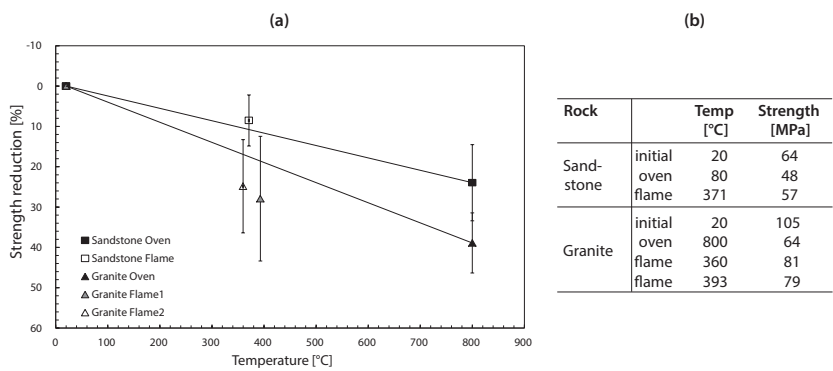


Figure 6.5: (a) Summary of the investigated rock samples: strength reduction of the rocks due to a thermal treatment (analyzed by scratching the rock samples with a PDC cutter. Data presented in [25]. (b) Strength values before and after the thermal treatment.

As it can be seen in Fig. 6.5, the priorly discussed effect of thermal treatments on the rock strength could be confirmed. For the high temperature range, at around 800°C , the oven treated samples show a reduction of strength by about 25% for sandstone and 40% for granite. This is in agreement with the strength variation during high temperature oven treatments reported by Zhang *et al.* [159] and Tian *et al.* [160]. Referring to the flame treatments at about 400°C , the sandstone and granite samples also showed a marked weakening after the treatment: the granite samples lost about 40% of their strength and the sandstone samples 10%.

The absolute strength values of this analysis are listed in Table 6.5 (b). It can be seen that the strength of the granite sample after the oven treatment could be successfully reduced to nearly the strength of untreated sandstone. This indicates the potential of such a combined process for drilling applications in hard, abrasive rock formations.

6.2.3 Footprint in the thermal properties³

The effective crack creation, due to thermal heating, can also be observed in the thermal properties of the rock structure. The thermal properties of Central Aare granite were measured with the laser flash analysis [161] performed by a Netzsch LFA 467. Further information about the measurement procedure, the experimental results and a comparison with theoretical models can be found in Kant *et al.* [76]. If rock samples are heated up (Fig. 6.6, marker ○), thermal diffusivity, heat capacity and calculated thermal conductivity are strongly affected by temperature. As already reported in various studies (*e.g.* Clauser *et al.* [99, 162, 163]), during heating, thermal diffusivity and calculated thermal conductivity decrease non-linearly with temperature, while heat capacity increases non-linearly. Upon cooling, while the heat capacity follows the same trend as for the heating phase and there is no permanent change in heat capacity upon the rock's return to room temperature, both diffusivity and calculated conductivity follow a different path with decreasing temperature and display permanent changes at room temperature (Fig. 6.6, marker ♦). Crack formation, due to the high thermal loading, was evaluated as the reason for this effect [106–110]. If the rock samples are exposed to further heating and cooling cycles after the initial heating phase, no further irreversible changes of the properties are observed.

³This section is based on Kant *et al.*, Geophysical Research Letters [76]

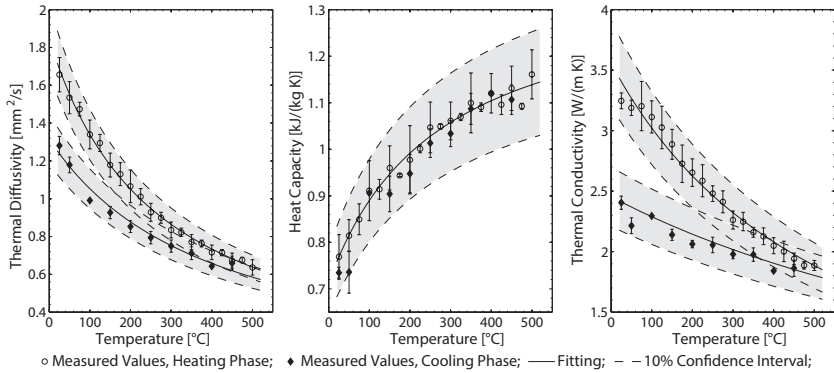


Figure 6.6: Thermal properties of Central Aare granite for the initial heating cycling; averaged values with the proposed correlations and 10% confidence interval of these correlations; errorbars indicate the standard deviations between all investigated rock samples at the specific temperature

In order to confirm that thermal cracking causes the observed irreversible decay of the thermal properties, petrographic thin sections of untreated and thermally treated samples are analyzed. The internal structure of Central Aare granite at baseline conditions shows only a few initial cracks (Fig. 6.7 (a)). If the specimens are heated to 500°C , the differential thermal expansion of the compositional elements leads to thermal cracking along the crystal boundaries (Fig. 6.7 (b)). An optical evaluation of the crack density, according to the procedure suggested by Nasser [164], showed a significant increase from initially 1.6 mm/mm^2 to 5.8 mm/mm^2 after heating to 500°C , whereupon virtually all cracks can be found along the grain boundaries. Cracks with a length between $50\text{ }\mu\text{m}$ and about $500\text{ }\mu\text{m}$ (mean length of $130\text{ }\mu\text{m}$) act as thermal resistances. As the heat transfer is impeded by these resistances, thermal conductivity and thermal diffusivity of the bulk material decrease after the first thermal cycle, leading to the irreversible decay shown in Fig. 6.6. Further heating/cooling cycles are ineffective for additional degradation of the thermal properties, as the material can now expand into the cracked grain boundaries and the thermal stresses are insufficient to cause further cracking.

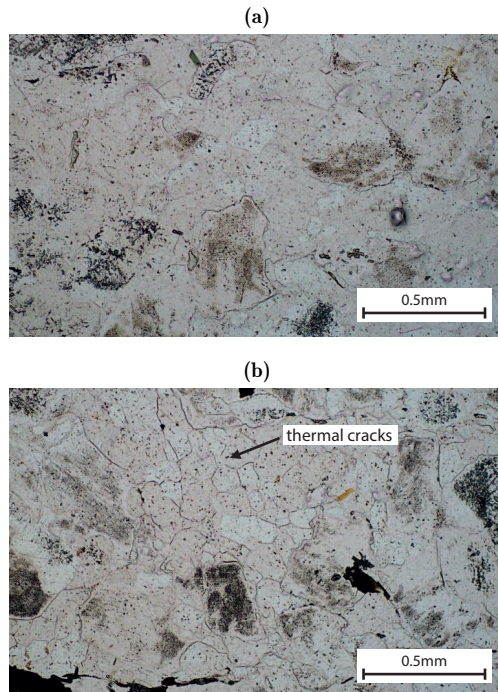


Figure 6.7: P lain-polarized pictures of thin section of the rock material at (a) initial conditions and (b) and after heating to 500°C with thermally initiated cracks at the grain boundaries.

6.3 Air shield protection

Entrainment of the cold dense water into the hot flame jet has already been identified as a major problem for spallation drilling in an aqueous environment [55, 73, 134, 165]. Already small amounts of water, penetrating into the hot fluid jet, are sufficient to completely cool down the flame jet (see Chapter 5.2.3 for a closer analysis).

So far this problem has been solved by blowing out the water from the spallation zone and keeping it with special sealing systems above the drill head. Unfortunately, this solution is not feasible for hybrid drilling. As

the mechanical cutters have to be cooled with the drilling fluid to avoid thermal wear-out, drilling mud is required as a coolant at the bottom of the head. Hence, the flame assistance has to be at the same time confined to a certain region to not overheat the mechanical cutters, but also providing an efficient heat transfer in order to achieve the required temperatures on the rock surface. A possible solution, proposed in this manuscript, is the application of an air-shield, which reduces the contact area between hot combustion gas and cold water. This air shield consists of cold compressed air, exiting with a high pressure and flow rate around the flame nozzle. The air shield is designed to provide a complete curtain of air around the jet in the center, which should create a buffer zone around the flame-jet. The buffer zone decreases the shear stresses on the hot jet, lowering the mixing between the different fluids. In order to investigate the feasibility of such an air shield, an experimental study is conducted in the following section.

6.3.1 Experimental setup and procedure

For the conducted experiments the s-ASDP setup in its oxygen configuration (Chapter 3.1) was used. The whole burner assembly is submerged with a linear actuator in a water tank. This water tank is continuously flushed with water to guarantee constant water temperatures (Fig. 6.8 (a)). An air shield mounted to the combustion chamber (Fig. 6.8 (b)) protects the hot jet from the cold surrounding water. The air flow rate to the air shield can be controlled manually with a rotameter. The flame jet impinges on a target plate made out of stainless steel with an array of thermocouples integrated into the surface of the target. After successful ignition, the required flow rates were adjusted and the burner was moved with the linear actuator to the desired SOD.

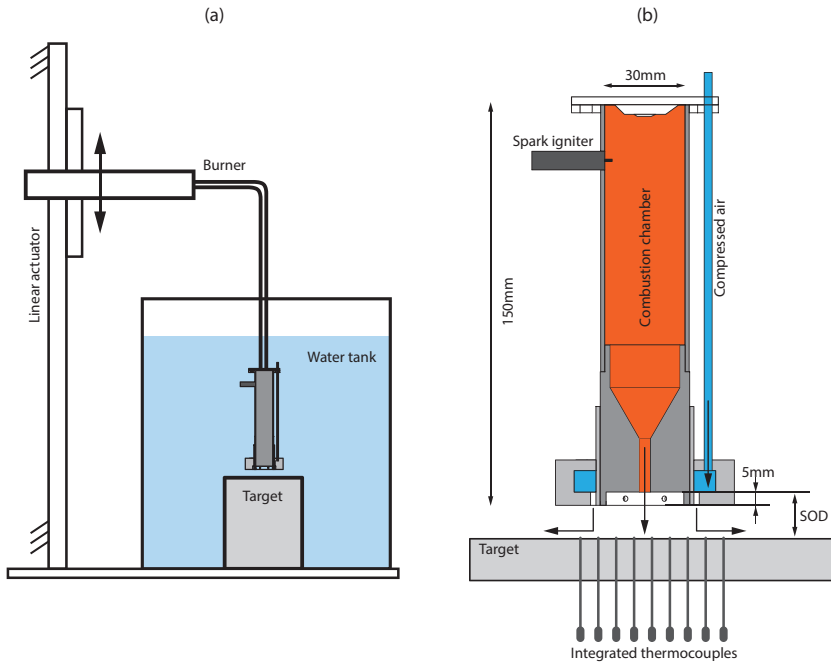


Figure 6.8: Illustration of the used experimental setup

6.3.2 Experimental results

The general influence of entrainment on the temperature of the metal target and the principle feasibility of the air shield can be seen in Fig. 6.9 (a), which shows the temperature average of the center thermocouple, as a function of the flow rate of the air-shield. Thereby, the SOD between nozzle exit and target is kept constant at 10 mm. For low flow rates of the air-shield supply, the temperature at the thermocouple stays constant at around 80°C , which shows that all heat is lost, due to entrainment, and low temperatures, which are insufficient for spallation, are detected by the thermocouple. If the flow rate is increased, at a certain point at about 140 L/min, the water can be completely removed from the area under the burner and the air shields sufficiently protects the hot air jet,

indicated by a rapid temperature rise to about 450°C .

A similar behaviour can be seen for the radial profile of the temperature along the target at an SOD of 6 mm (Fig. 6.9 (b)): for low flow rates of the air shield, the water penetrates the hot air jet and no sufficient heat input can be monitored. If the air shield exceeds a certain flow rate, the air can protect the flame-jet and high temperatures, together with a sufficiently wide treatment zone, can be observed. If the flow rate is further increased, temperature level and size of the treatment zone are even more improved.

It can be concluded that without an air-shield no sufficient heat flow can be delivered to the target and already small SODs are sufficient that water can completely entrain into the flame-jet. The air shield protects the flame jet, prevents entrainment successfully and high temperatures (500°C) can be induced on the surface of the target.

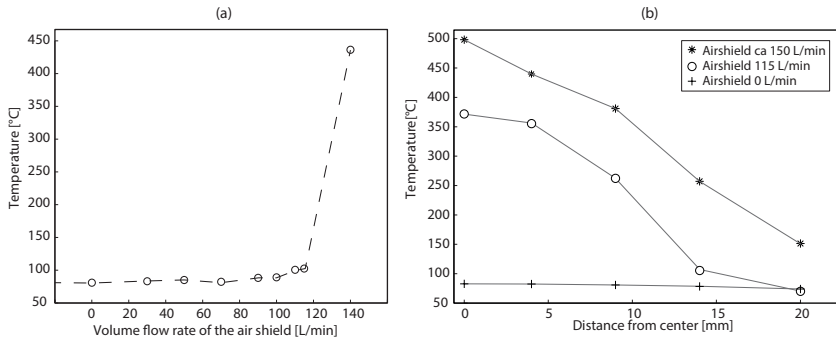


Figure 6.9: (a) Comparison of the influence of the air shield on the temperature in the center of the target. Constant burner flows of $1 \text{ m}^3\text{n/h}$ methane, $1.7 \text{ m}^3\text{n/h}$ oxygen and $1.6 \text{ m}^3\text{n/h}$ air. SOD kept constant at 10 mm. (b) Comparison of the influence of the air shield on the radial temperature profile. Same burner flows as in (a). SOD kept constant at 6 mm.

The heat transfer can be further improved, if the flame temperature is increased. This is illustrated in Fig. 6.10, where the total mass flow was kept constant and the ratio between O_2 and air admixture was varied. It can be seen that with more O_2 content in the combustion mixture, the temperature on the target is increased from 250°C to 550°C .

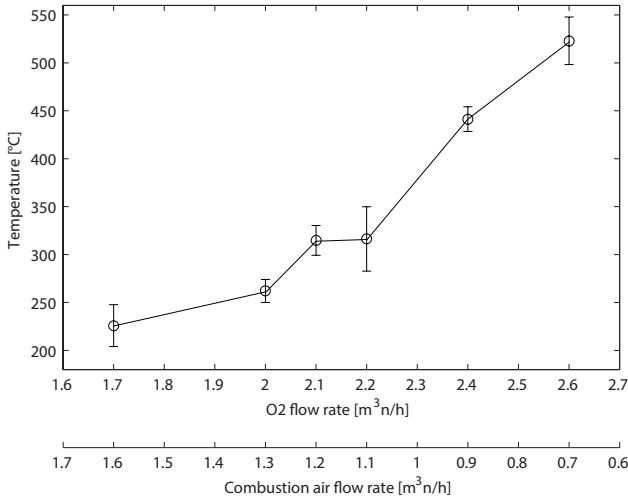


Figure 6.10: Comparison of the measured temperature with an air shield flow of 115 L/min. O2 and combustion air flow rates are changed and the total volume flow rate is kept constant at $4.3 \text{ m}^3/\text{n/h}$. The methane flow rate is constant at $1 \text{ m}^3/\text{n/h}$. SOD=10 mm.

Concluding, with this concise experimental investigation, it is shown that an air-shield can prevent entrainment of water into the hot combustion zone, the heat of an submerged drill head can be transferred to the target and sufficient temperatures can be induced. Therefore, the air-shield is a suitable solution to enable the application of a hybrid drilling system in a water filled bore hole, as it confines the heat to a certain area to avoid thermal wear of the mechanical cutters and provides an efficient heat transfer to the rock surface. Additionally, high O2 flow rates will further increase the heat transfer performance. Therefore, even though oxygen-based systems are less economically viable than air-based systems, they might be more appropriate for a first application of a hybrid drilling system.

6.4 First conclusions

Different experiments were conducted to investigate the general feasibility of a combined thermo-mechanical drilling system. The possibility to weaken the rock structure with thermal loads, if the rock is not spallable, was shown in two experimental investigations. These experiments showed that the rate of penetration can be significantly increased and the rock strength decreased to 40% of its initial value, if the rock is thermally treated with a flame or in an oven. Concluding, a combination of mechanical and thermal spallation drilling seems to be an appropriate approach, which could enable the use of the spallation technology also in non-spallable rock sections. Thereby, an air shield protection around the combustion zone overcomes the general problem of cold fluids entraining and cooling down the flame-jet.

6.5 Field test in cooperation with GZB Bochum

As the principle feasibility of a combined thermo-mechanical drilling system was shown and the postulated benefits could be preliminary confirmed, further steps in the development of a hybrid system were conducted. In order to show the applicability and operational readiness, a first field test was planned in cooperation with the International Geothermal Center in Bochum (GZB), Germany. Thereby, two different thermal load concepts were selected: a laser system working with a high power laser jet, whose development is led by GZB, and a flame system operating with a high power methane-oxygen flame, where ETH Zurich leads the development. The drill tests will be performed with the Bo.Rex (Bochum Research and Exploration Drilling Rig) of the GZB, which is a mobile dual top drive drill rig with a weight of 40t (see Fig. 6.11 (a) & (b)) [166]. The size of the drill head was defined by the project partner as 140mm in diameter for both test systems and the mechanical cutting process will be accomplished by a special mechanical drill bit face designed by GZB, with a similar layout for both experiments. The overall goal of this field test is to show the general feasibility of such a com-

bined system, to proof the postulated benefits in a realistic environment and to compare both drilling systems (laser and flame). As the underground in Bochum consists of Ruhrkarbon, a formation with changing layers of sandstone and mudstone, where a combined system is not able to show its benefits, large (2.5m x 0.5m x 0.5m) granite blocks (see Fig. 6.11) of Central Aare Granite were transported from the Grimsel Pass to Bochum. These rock blocks will be used for the drilling tests, due to the discussed benefits of this rock structure (Chapter 3.2). It has to be said in advance, that the described field test could not be finished during the progress of this thesis, due to complications in the development and manufacturing of some parts and the corresponding delay of several months. Nevertheless, important design aspects for such a combined drilling system could be gathered and therefore, the current status of the project is discussed in the following section.

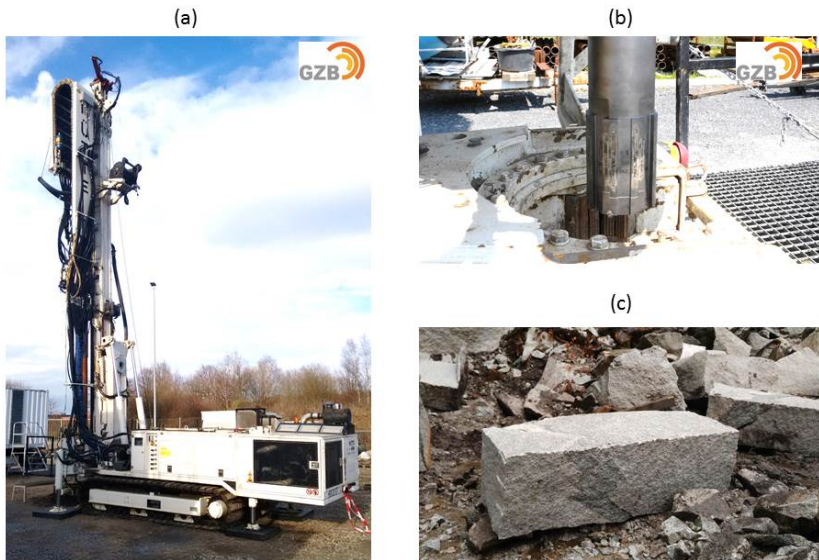


Figure 6.11: (a) Picture of the Bo.Rex drill rig, used for the discussed field test. (b) Picture of the drill head used for the laser jet project. Both pictures by courtesy of GZB Bochum. (c) Picture of one of the used rock blocks with a size of about 2.5m x 0.5m x 0.5m

6.5.1 Design of the system

The hybrid drilling system used for this field test was designed and developed by GZB Bochum to keep the required modifications from the drilling platform Bo.Rex at a minimum and to allow the integration of both, the laser cartridge and the flame system, enabling a later comparison of the two heating principles. The overall schematic of the 11 m long drilling system used for this field test is illustrated in Fig. 6.12. At the front of the system, the hybrid drill bit transfers the thermal and mechanical load to the rock surface. It consists of a bit face, where the mechanical cutters are placed and the thermal load impinges on the rock, followed by the drill bit, which transmits the mechanical load to the rock's surface, keeping the delicate flame system (or laser cartridge) inside the bit free of load. The following 3.5m long drill pipe transfers the force and rotation from the top drive system, which is connected at the drill pipe's outer diameter, to the drill bit. After the top drive, the 1st swivel is mounted, supplying the required flow of oxygen, air and drilling mud. Thereafter, an equalizer rod follows at the end of which the 2nd swivel is placed, supplying the methane flow and providing electrical connections for the igniter and various measurement devices.

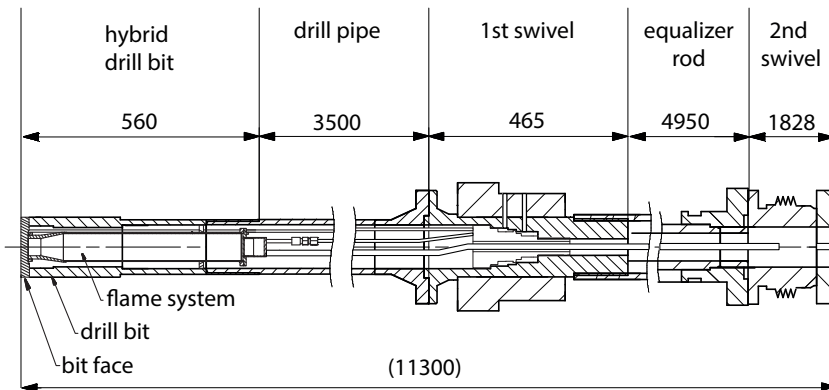


Figure 6.12: Schematic illustration of the used drill system with the most important components and the main dimensions highlighted

6.5.1.1 Hybrid drill bit

In order to create an efficient flame jet, a special hybrid drill head was developed. Thereby, the design process focused on a robust and simple design, which can withstand the high forces, severe temperatures and vibrations, prevailing in such a drilling environment. Additionally, special attention was paid to the modular construction of the system, which enables a replacement of single components in case of failure. Fig. 6.13 shows the resulting system.

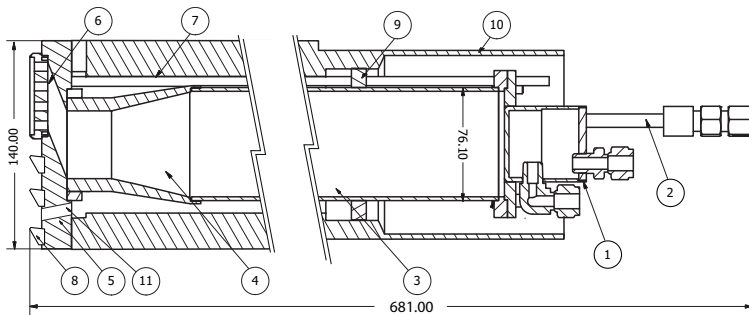


Figure 6.13: Drawing of the hybrid drill head with its main dimensions. (1) Burner, (2) igniter tube, (3) combustion chamber, (4) nozzle, (5) drill bit face, (6) distribution box, (7) air supply, (8) mechanical cutters, (9) vibration damper, (10) drill bit and (11) drilling mud nozzle.

The flame is created with a modified Arnold 141/050.17 high capacity burner (1), combusting methane and oxygen to establish a 54kW strong flame (see additionally Fig. 6.14 (a)). This burner is ignited with a hot surface ceramic igniter, which also allows to monitor the flame temperature after ignition, by means of a resistance measurement. This igniter is placed inside an igniter tube (2) with a high pressure, high temperature graphite sealing (Conax MHC2 series) at its top. The reactants combust inside a combustion chamber (3) (see additionally Fig. 6.14 (b)) at the end of which a nozzle (4) accelerates and compresses the flow, before it is deviated by a sloped slot milled through the bit face (5). Finally, the combustion gases exit through several nozzles integrated in an interchangeable distribution box (6) (see additionally Fig. 6.14 (c)). The nozzles are protected by an air-shield, which obtains the required air

supply from external pipes (7). Mechanical cutting elements (8) ensure an optimal mechanical drilling process. A vibration damper (9) reduces radial movements of the assembly, reducing the risk of fatigue failure. The mechanical force is transferred to the cutters via the drill bit (10), which forms the outer mantle of the drilling system. The whole assembly is cooled by water respectively flowing in the annulus between combustion chamber and drill bit. The water exits the drill bit face through various nozzles placed at the bit face (11) and flushes the created rock cuttings to the surface.

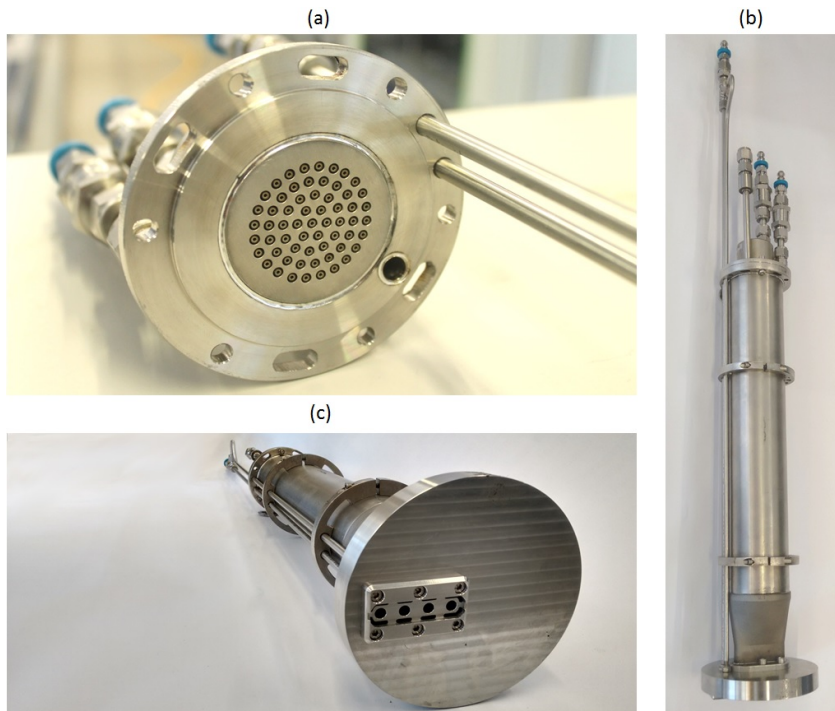


Figure 6.14: Pictures of the designed hybrid drill head equipped with a dummy bit face without mechanical cutters and drilling mud nozzles. (a) Picture of the burner and the upper flange, on the lower right the igniter tube is visible. (b) Side view of the burner assembly. (c) View of the bit face with the distribution box.

A technical drawing of the assembly can be found in Appendix D. The distribution box distributes the hot combustion gases coming from the sloped slot milled in the bit face (Fig. 6.15). It features four nozzles with a diameter of 6mm, distributed over the radius of the drill bit face. This ensures that about 80% of the surface below the drill bit is covered and can be thermally treated. A complete coverage is not possible, due to the required space for the mechanical cutters (Fig. 6.16). The four nozzles are protected by an air-shield, which is created by compressed air, leaving the distribution box through several air slots with a width of 2mm. The part is mounted to the drill bit face with six M4 screws, making it easily exchangeable in case of thermal or mechanical wear. Potential radial or axial loads are absorbed by a shoulder around the distribution box. The height of the distribution box is designed to maintain a 3-4mm gap between the end of the part and the rock surface. This allows a certain wearing of the mechanical cutters, prevents extensive mechanical load on the distribution box and keeps entrainment of drilling mud in the combustion zone at an acceptable level (see Chapter 6.3 and Chapter 5.2.3 for further information about the entrainment issue).

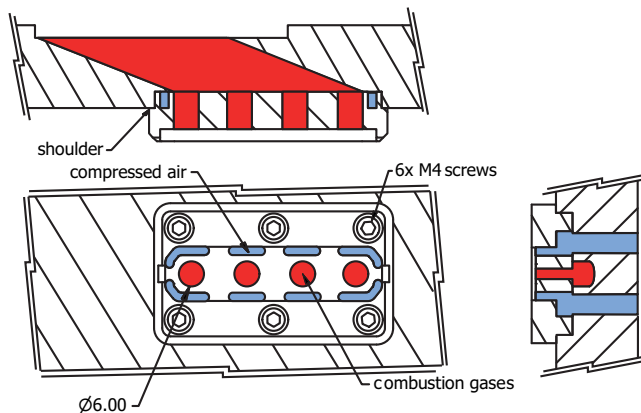


Figure 6.15: Illustration of different views of the distribution box integrated into the drill bit face, red colors indicate combustion gases and blue colors the air shield.

In order to ensure an effective mechanical destruction of the weakened

rock structure, hard metal cutters are brazed onto the drill bit face (Fig. 6.16). Drill mud nozzles are integrated into the drill bit face to ensure cooling of the mechanical cutters and a sufficient particle transport. The particle transport is further enhanced by the slightly convex shaped drill bit face and the octagonal shape of the outer diameter of the drill bit. The design and material selection of the drill bit was done by GZB Bochum in cooperation with a drilling supply company.



Figure 6.16: Modified picture of the first prototype used for the initial reference test, without integrated distribution box. Courtesy of GZB Bochum.

6.5.1.2 Supply network

In order to ensure a constant flow of the process fluids to the drill rig and to guarantee a safe operation, a special supply network was designed (Fig. 6.17). The pressure of every fluid except for the drilling mud is monitored and controlled by pressure reducers. The flow rates are controlled by three flow controllers and valves enable the manual shut-off of single flows. Inside the drill rod, high temperature and high pressure metal hoses are supplying methane, oxygen and compressed air to the drill head. The drilling mud flows free inside the drill string. Flame arrestors after the flame system, at the entrance to the swivels and be-

fore the gas bottles ensure a safe operation of the whole assembly. The igniter is controlled via a power supply and resistance measurement system, allowing a safe ignition and a later observation of the combustion temperature. Gas accumulations inside the drill rod, due to potentially occurring leaks, are indicated by a water indicator (H₂O-I), which further increases the safety of this setup. Additionally, the temperature on the drill bit face is monitored to avoid extensive thermal wearing.

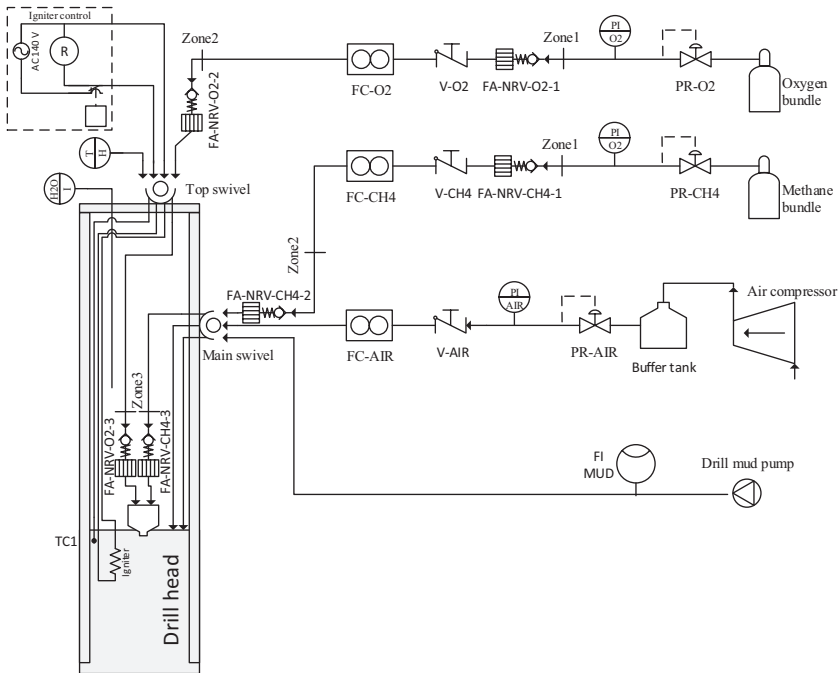


Figure 6.17: Schematic illustration of the network for the thermal-mechanical combined drilling experiment. Symbolic: PR - pressure reducer, FA-NRV - flame arrestor with non-return valve, V - valve, FC - flow controller, TC - thermocouple.

6.5.2 Test of the flame system in the lab

In order to preliminary test the required functionalities of the designed flame system, the module was tested in the laboratory at ETH with the

network shown in Fig. 6.17 without swivels, drill bit and drill pipes. A dummy plate without mechanical cutters, as shown in Fig. 6.14, was mounted and the head was submerged in a water tank to simulate the conditions during drilling and to provide sufficient cooling of the combustion chamber. A stainless steel target with integrated thermocouples, which are aligned along the radius of the drill bit, is placed 3mm under the end of the distribution box, to measure the induced temperatures. In order to ignite the burner, an oxygen flow of 0.31 kg/h was adjusted and the igniter was supplied with a voltage of 120V. After the igniter was heating up for 30s to reach the required surface temperature, a methane flow of 0.04 kg/h (corresponds to $\lambda = 2$) was adjusted, leading to the immediate ignition of the system. Thereafter, the burner was rapidly driven up until a methane flow of 2 kg/h was reached, whereas λ was meanwhile lowered to 1.2. As Fig. 6.18 (a) shows, at a mass flow of 1.6 kg/h of methane, the produced flame jet was able to remove the water between target and distribution box and a surface temperature of about 650°C could be measured, already without help of the air shield. The radial distribution of the temperature shows without air-shield a significant decreasing trend with increasing radial position of the thermocouples from 650°C to 100°C . Only the central nozzles can be sufficiently protected from entrainment by their neighboring flame jets. The outer two nozzles are entrained by water, indicated by the extreme low temperature (position 40mm and 45mm). If the air shield is build up, by pumping compressed air through the air slots, the temperatures of the third nozzle (position 40mm) can be increased by 100% (Fig. 6.18), whereas the temperature of the last nozzle remains at 100°C . Thereby, it has to be mentioned, that due to safety regulations, only half of the designed methane flow was adjusted for this preliminary test. Therefore, it can be expected that at full operation also the outer nozzles will be sufficiently supplied by hot combustion gases, which will increase the treatment zone.

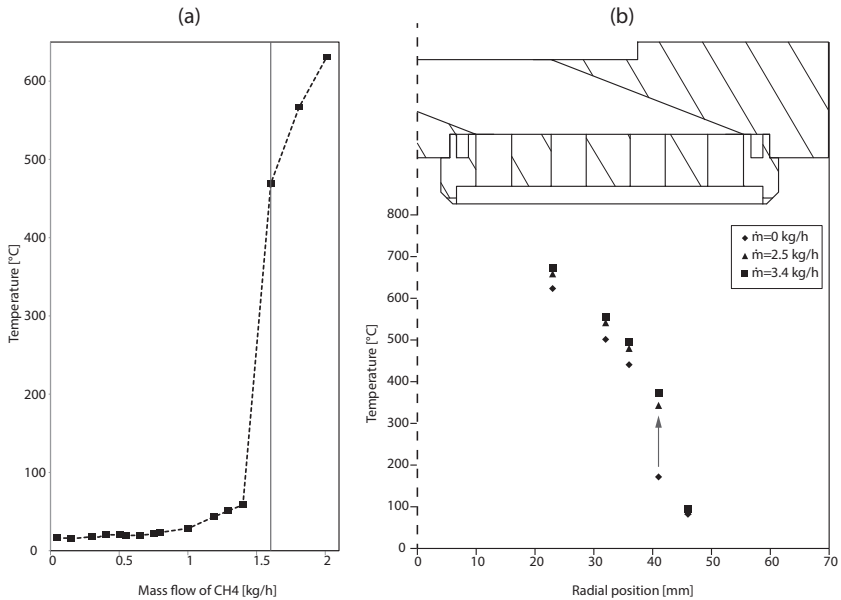


Figure 6.18: Results of the experimental test of the flame system. (a) Temperature progression of the first thermocouple (position 22mm) as a function of the methane mass flow, without any air-shield (except for 1.8kg/h) and $\lambda = 1.2$. (b) Radial temperature distribution for different air shield flow rates along the base plate in a distance of 3mm from the end of the distribution box, measured on a steel plate.

Concluding, the system could be successfully ignited and tested. High temperatures could be induced on the steel target. Nevertheless, the radial distribution is still improvable. If test at higher flow rates do not show an improved distribution, a modification of the interchangeable distribution box might be appropriate. This preliminary tests showed the operational readiness of the drill head with all its functionalities. Therefore, it can be concluded that the designed drill head fulfills the required expectations and can be used in the discussed field test.

6.6 Conclusions of this chapter

In this chapter a thermo-mechanical drilling system was introduced, which combines thermal spallation drilling and mechanical drilling. With this system the limitations for thermal spallation drilling in deep drilling operations, such as soft intrusions, large fractures and fluid intrusions can be overcome. Non-spallable intrusions and sections will be thermally treated by the flame, to reduce the rock strength and finally to reduce the required power input from the mechanical cutters. The feasibility of such a treatment process was shown in two experimental investigations. Further, an air shield protection was introduced as a good possibility to avoid entrainment of cold drilling fluids into the combustion zone. In order to show the applicability and operational readiness of such a combined drilling system, a field test in cooperation with the GZB in Bochum was initiated. In this field test a 11m long combined system with a diameter of approx. 5-1/2 inches (140mm) will be used to assess the applicability of the method. The complete system was developed by the GZB Bochum for a mechanically supported laser drilling system and modified by ETH Zurich towards a flame heating system. The preliminary test of the designed drill head, showed that the system is ready for operation and can be used in the future.

CHAPTER 7

Thermal bore hole enlargement

As discussed in the beginning of this thesis (Chapter 2.3), the development of deep geothermal energy is impeded by the high costs of the drilling phase together with an unfavorable risk assessment of the technology. Besides the possibility to reduce the drilling costs and to shift the risks to the beginning of the project, geothermal energy can also be promoted by reducing the project risk in general (see Fig 7.1). One major reason for project failures are insufficient production rates of the brine, leading to an uneconomical perspective of the power plant. Due to near well bore impedances (formation damage), insufficient access to preexisting natural fractures or an unfavorably located well end, only insufficient fluid flow can be transported through the open fractures, making the well unproductive. Exemplary, the deep geothermal project in St. Gallen, Switzerland was stopped after a production flow of only 10% of the expected flow rate could be observed and an injection test caused a seismic event ($M=3.5$), leading to a lost investment of about 40 Mio. USD [167].

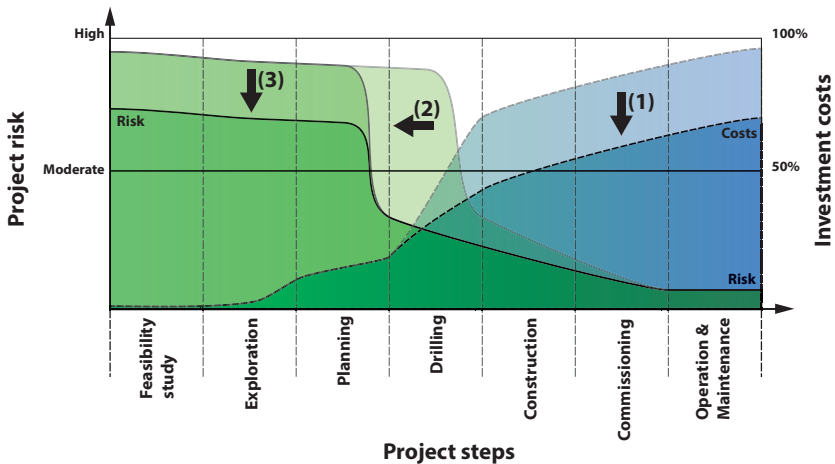


Figure 7.1: Ways to promote geothermal energy: (1) cost reduction due to novel drilling techniques, (2) risk shifted away from expensive projects steps due to increase knowledge and experience, (3) risk reduction, due to bore hole enlargements. Figure adapted from Gehringer *et al.*[22].

Hydraulic stimulation, by high pressure fluid injection, is a commonly used technique to recover formation damage and to increase the reservoir permeability in the reservoir, by creating new fractures and enhancing existing fractures [8, 168, 169]. This method increases the production rate of a well and in EGS-systems establishes an underground heat exchanger by connecting injection and production well [169]. Nevertheless, hydraulic stimulation, in particular in EGS-systems, remains challenging, as direction and extension of the created fractures in the formation are not precisely controllable and therefore large fracture networks, reaching out in the formation, are difficult to create [169, 170]. Further, hydraulic stimulation frequently leads to induced seismicity, which hampers its application [13, 14, 171]. Therefore, in order to promote the development of geothermal energy, ways have to be found to reduce or remove formation damage and to enhance the stimulation process, by providing excellent access to preexisting fractures [7, 8, 11].

7.1 Thermal bore hole enlargement

Thermal bore hole enlargement is a novel technique, which was developed in the course of this thesis. It increases the well diameter by utilizing the thermal spallation process to excavate the rock on the sidewalls of an existing bore hole. Nozzles are placed at the circumference of a burner assembly, which create the required flame jet to induce spalling. As these flame nozzles can be placed freely and a rotation of the system around its axis is possible, a nearly arbitrary geometry of the enlarged bore hole, as *e.g.* slots, notches or complete hole openings (Fig. 7.2), can be created with this technology.

By opening the well bore diameter, near well bore impedances are removed and the created notch serves as an initial fracture source. Additionally, the hydraulic connection between well and rock is improved, access to more preexisting natural fractures can be attained and the initial size of the reservoir is increased. These measures will enhance the hydraulic stimulation process, as lower pressures to achieve initial breakdown of the rock mass are required (removal of well bore impedances) and a larger number of fractures can be stimulated, facilitating fluid circulation and subsequent heat extraction.

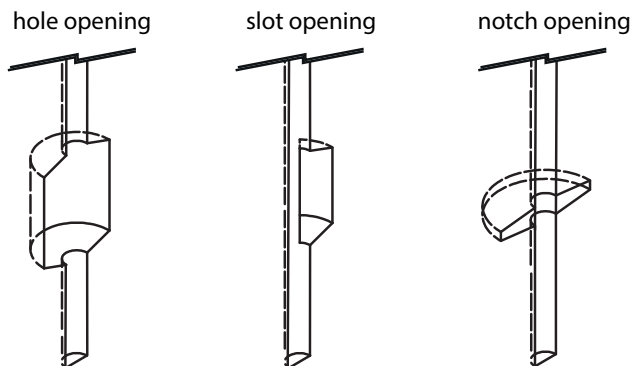


Figure 7.2: Illustration of possible enlargement geometries.

Therewith thermal bore hole enlargement has the potential to enhance the development of engineered geothermal systems, as less total investment is required, the project failure risk can be reduced and the production flow rates are increased. The low additional costs to apply the proposed solution to an abandoned or poorly performing well further increases the potential of this technology.

The thermal enlargement process is conducted as follows (Fig. 7.3). (a) The bottom hole assembly (BHA), consisting of a burner and a packer system, is tripped down into the well to the interval, which will be stimulated. The target zone is sealed off from the rest of the well bore with a packer system. (b) The bore hole fluids are removed from the treatment zone by pumping air through the burner, as entrainment of the high density aqueous fluids into the low dense setting of the flame jet will lead to a short, cold exhaust jet with insufficient treatment power [25, 51, 73, 134]. (c) The burner is driven up by starting the combustion, which initiates the thermal spallation process. During excavation of the bore hole wall, the device is moved axially or rotated to create the desired enlargement geometry. (d) After the process is finished, the whole BHA is removed. The enlargement process can be repeated in other sections of the well or the BHA is retrieved to the surface.

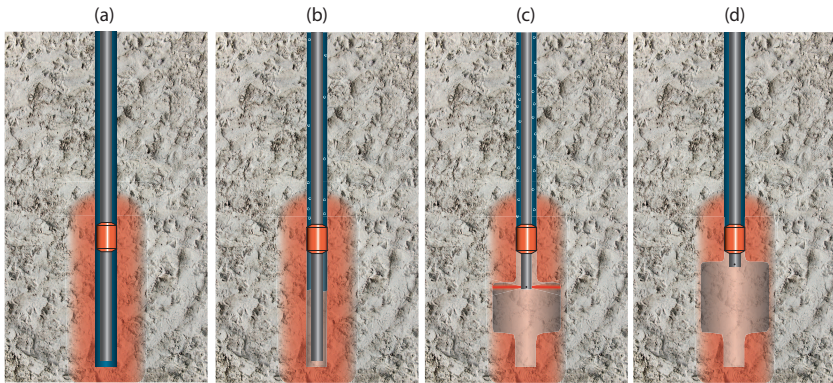


Figure 7.3: Principles of thermal bore hole enlargement. (a) Installation of the jetting system, (b) removal of water from the treatment zone, (c) enlargement of the bore hole, (d) completion of the process.

7.2 Field test in the Grimsel Test Site

In order to demonstrate the applicability of the described thermal bore hole enlargement process, a full-size field test was conducted in the Grimsel Test Site (GTS). The Grimsel Test Site is an underground rock laboratory located in the Aare massif of the Swiss Central Alps (Fig. 7.4 (a)) [172]. In this underground laboratory a wide range of research projects such as geological disposal of radioactive waste, *in-situ* stress analysis and geothermal stimulation experiments are conducted [173–175]. For the application of the technology described above, a borehole was drilled with conventional methods with a diameter of 86mm, a length of 14.5m and a completely vertical orientation. The bore hole has a low inflow of formation fluids and can therefore be considered as water-filled. A homogeneous smooth surface is present and no natural fractures interfere with the well. It lays in the Central Aare granite formation, which has been used as the reference rock material throughout this thesis (details can be found in Section 3.2).

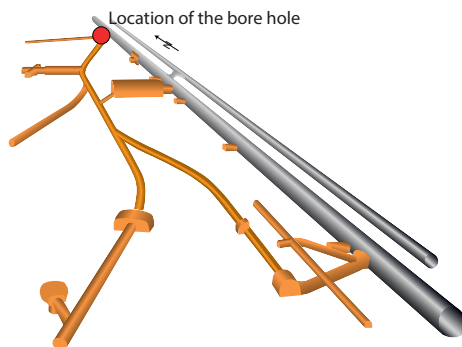


Figure 7.4: Schematic layout of the Grimsel Test Site with the location of the bore hole discussed in this report highlighted.

7.2.1 The experimental setup

A schematic overview over the applied experimental setup can be found in Fig. 7.5 (a). The flame jet required for thermal spallation drilling is supplied by a bottom hole assembly, consisting of a burner and a packer system. The burner is driven by a lean mixture of methane and air, with a combustion power of max. 70kW. The required supply of fluids, electricity and data communication for this bottom hole assembly is established by a 25m long coiled tubing, which is supported by a 4mm steel rope to avoid extensive mechanical load on the coil. The position of coiled tubing and bottom hole assembly inside the bore hole is controlled and maintained by an injector with an attached winch for the steel rope. The bottom hole assembly can be rotated around its axis by revolving the coiled tubing at the top of the injector. A control system with integrated flow controllers and data acquisition systems monitors and controls the supply of the fluids and captures the measurement data. Air is extracted from the surroundings with a 8 bar air compression system. Methane is taken from a methane bottle with an outlet pressure of 10bar. Cooling water is supplied from a tap water connection with about 5 bar and a flow rate of ca 300 l/h. The well is sealed with a well head, which separates the combustion gases rising up from the burner to the surface. A fan attached to the exhaust pipe of the well head guides the gases away from the setup into the access tunnel of the test site.

The coiled tubing feeds all the required fluids from the control system to the bottom hole assembly (Fig. 7.5 (b)). The outside of this coiled tubing forms a corrugated stainless steel hose with an additional stainless steel braiding, making the whole assembly suitable for temperatures up to 500°C and operating pressures of 25 bar. The combustion air flows inside the metal hose, providing a certain cooling effect to the coil and allowing low pressure losses. Methane is supplied via a single PTFE hose with a carbon insulation for static dissipation and a stainless steel braiding. Cooling water supply and return is guaranteed by two Teflon hoses. In case of uncontrolled combustion inside the coiled tubing, these hoses will break first, which will flood the tubing and extinguish the flame. Different electricity cables are placed inside the coiled tubing enabling temperatures measurements and power supply for the igniter and water indication system. The whole system can reach a depth of maximum 25m and requires an area on the surface of about 50m^2 . A modification of the system for greater depths is possible.

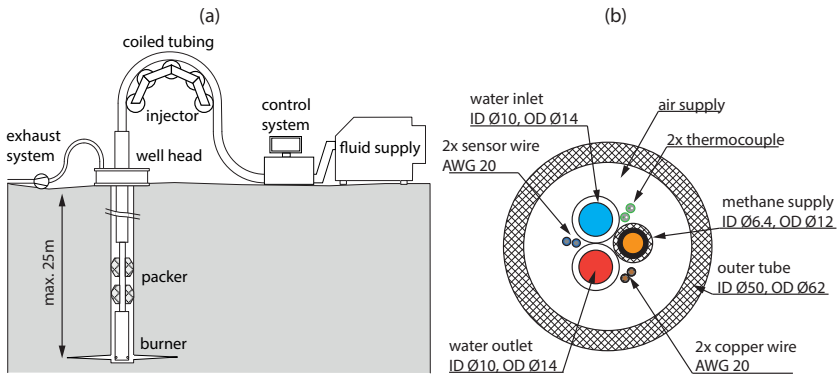


Figure 7.5: (a) Overall layout of the experimental setup. (b) Detailed illustration of a cross section of the applied coiled tubing, with the different diameter highlighted.

The whole bottom hole assembly (BHA) is placed inside the bore hole (Fig. 7.6 (1)). Air (2) and methane (3), supplied by the priorly discussed coiled tubing, are mixed at the entrance of the combustion chamber (4). Their combustion is initiated and monitored with an igniter (5), consisting of a heat wire with an integrated thermocouple [103].

In order to maintain the temperature of the burner at an acceptable level, the combustion chamber (6) is cooled by water (7), which is also supplied and removed via the coiled tubing. After combustion, the hot gases are accelerated and deviated through a single nozzle (8), with a diameter of 7mm, placed at the lower circumference of the BHA. The gases exit the nozzle and impinge on the sidewall of the bore hole, spalling the rock and creating a cavity (9). The combustion gases leave the treatment zone by raising up inside the bore hole. A packer system (10) seals of the combustion zone from aqueous bore hole fluids (11) to maintain a gas-like state around the nozzle, avoiding entrainment of bore hole fluids into the hot flame jet. The packer consists of two stainless steel cylinders, creating a 1mm gap between their circumference and the bore hole wall. It seals off the combustion zone from the above located fluids by sustaining a counter-current flow limitation (CCFL) with zero liquid penetration in the annulus between packer and bore hole wall [176–182]. Thereby, the created particles travel to the surface through the packer together with the combustion gases or sink down to the bottom of the well. In order to observe, if the treatment zone between packer and the lower end of the burner can be kept free from water, a water indication system (12) is integrated at the lower end of the BHA. This systems measures the voltage drop over two open pins and can therewith distinguish between a flooded and a water free situation. The temperature 10mm below the outlet of the nozzle and inside the end of the coiled tubing is observed by two K-type thermocouples (not illustrated).

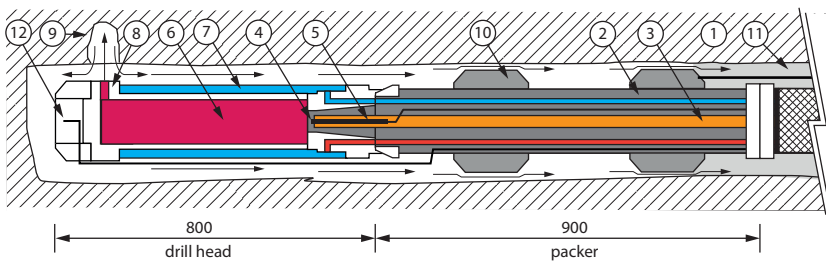


Figure 7.6: (c) Illustration of the bottom hole assembly with the packer system, drill head and nozzle.

7.2.2 Experimental procedure

Two exemplary hole opening geometries were drilled in the priorly mentioned well located in the Grimsel Test Site. The first enlargement experiment aimed at drilling a slot opening, as illustrated in Fig. 7.3 (b), at a depth of 13.5 m. The second enlargement experiment creates a notch opening slightly closer to the surface, at a depth of 7.5 m.

Both trials were drilled with the same procedure. The discussed experimental setup was installed and the burner was tripped down in the water-filled bore hole to the desired position. Thereby, an air flow rate of 3-12 kg/h was adjusted to prevent bore hole fluids from entering the coiled tubing through the nozzle. After the desired position was reached, a methane flow of 0.25 kg/h and an air flow rate of 7.5 kg/h was adjusted, which refers to an air-fuel-ratio of $\lambda = 1.7$ (see Fig. 7.7 (a)). The igniter was started with a voltage of 65 V and a current of 4.5 A. The latter was then increased stepwise until ignition could be observed at 6.7 A for the slot opening and 7.3 A for the notch notch. During the ignition procedure, the burner was lifted up by 10 cm to evacuate bore fluids from the combustion chamber (see the voltage indication in Figure 7.7 (b) at the beginning of the experiment), facilitating the ignition process. After successful ignition, indicated by a temperature increase of the nozzle temperature (Fig 7.7) (a)), the methane and air flow rate was continuously further increased. The rising pressure in the treatment zone, leads first to a partly fulfilled CCFL, indicated by a jump in the voltage measured by the water indication system and fluctuations in the nozzle temperature, caused by water films running down in the annulus. If the flow rates are further increased, a complete removal of the bore hole fluids from the treatment zone can be achieved, detected by a steady signal of the water indicator (Fig. 7.7 (b)) and a rapid temperature increase at the nozzle from about 100°C to 600°C.

For the slot opening, the burner rate was then increased to a flow rate of $\dot{m}_{CH_4} = 2.5 \text{ kg/h}$, $\lambda = 1.2$ and the whole assembly was lifted up to excavate the desired slot. For the notch opening, first, a flow rate of $\dot{m}_{CH_4} = 1.5 \text{ kg/h}$, $\lambda = 1.2$ was adjusted and the coiled tubing was slowly (within 4 minutes) rotated by 180° in both directions. Thereafter the flow rate was increased by steps of 0.25 kg/h and for every step the coil was turned again with the same procedure, until a combustion power of

$\dot{m}_{CH_4} = 3.5 \text{ kg/h}$, $\lambda = 1.2$ was reached. At this last operating condition, high fluctuations in the flow rates were registered, caused by pressure accumulations in the treatment zone.

After completion of the hole opening process, the burner was extinguished by setting the methane flow to zero and the air flow rate was increased to flush up remaining cuttings, preventing stuck pipe issues. The burner was tripped up to the surface and lifted out of the bore hole. The complete enlargement process was finished after about 30min with additionally 15min for tripping in and out.

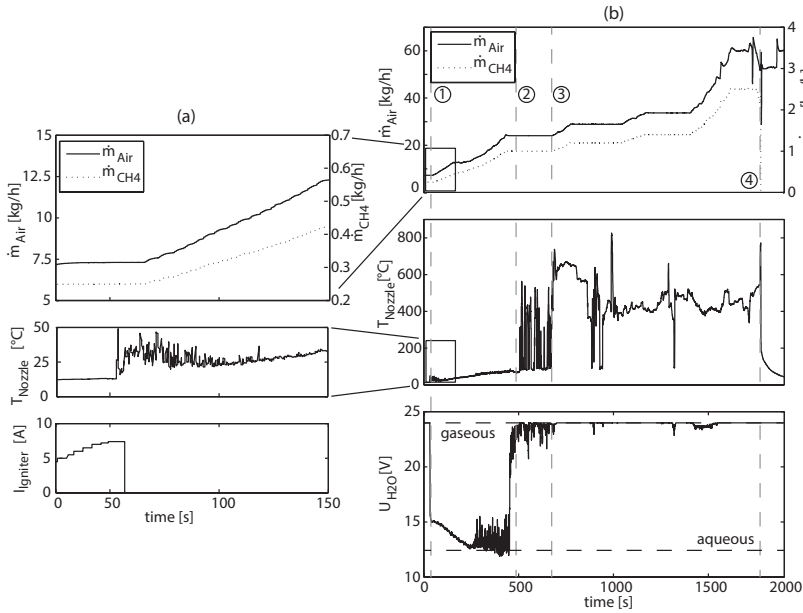


Figure 7.7: (a) Magnification of the ignition procedure. Ignition occurred at ≈ 60 s. (b) Overview over the entire experiment with (1) ignition of the flame, (2) onset of the counter current flow limitation and initiation of the first turning process, (3) complete removal of water from treatment zone. Note the interruption of the zero penetration restriction indicated in the measured voltage and the nozzle temperature, (4) extinction of the flame after completion of the process.

7.2.3 Results of the field test

7.2.3.1 Particle size distribution

The rock particles created during the two discussed thermal enlargement processes were collected and analyzed. Thereby, the particles which were flushed up together with the combustion gases were collected in a radius of 1m around, under and in the wellhead. Additionally, a certain amount of particles could be collected from the bore hole end by tripping a rigid water hose to the bottom of the bore hole and flushing with tap water. At the end of this flushing process, the bore hole was still filled with about 1m of spalls created during the two experiments. The particle distribution is a function of the process and not of the enlargement geometry. Therefore, the particles size distributions for both conducted experiments are similar and only the results of the notch opening experiment are discussed in the following.

After collection, the particles were dried in an oven at a temperature of 80°C for 5 hours, resulting in a dry weight of about 300g. The particles were sieved with in total 14 sieves ranging from 6.7 mm to $25\mu\text{m}$. Thereby, the change of the mesh size between two consecutive sieves is kept between 60% and 75%. The weight of the different sieved fractions were measured with a scale, having a precision of 0.1mg.

Fig. 7.8 (a) shows the resulting weight distribution and Fig. 7.8 (b) the cumulative curve of the particles.

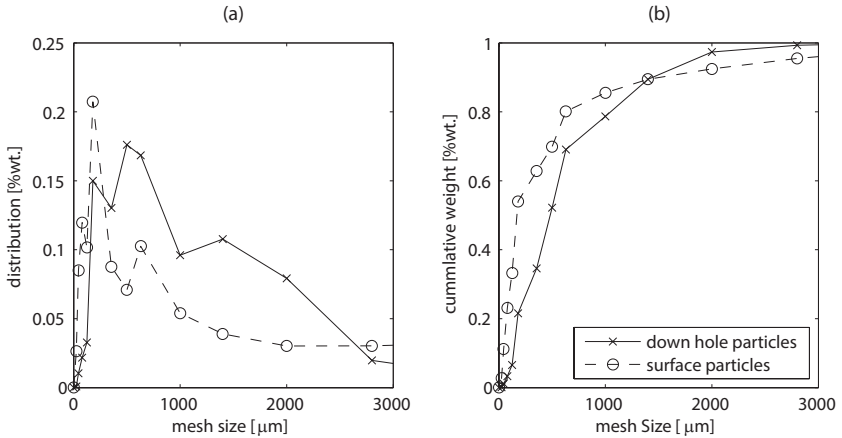


Figure 7.8: (a) Particle size distribution and (b) cumulative distribution of the created particles.

The distribution of the two investigated fractions are relatively similar with particles sizes ranging mainly between $45\mu\text{m}$ and $2000\mu\text{m}$ and having a mean particles size of about $500\mu\text{m}$. The particles are smaller than the grain sizes of the initial rock material, which indicates that the rock fracturing process occurs inter- and intragranularly. Thereby, it cannot be excluded, that the particles have been further disintegrated during the transport process. The collected particles are in a similar size range as cuttings produced during conventional mechanical drilling [183–185]. This suggests that the particles could also be transported up from greater depths by standard methods applied for cutting transport in conventional drilling processes, which indicates the transfer possibility of the technology for deep geothermal systems.

7.2.3.2 Geophysical characterization of the created enlargements

After some time for the particles to sediment, the results were investigated with a down hole camera and an acoustic televiewer. The televiewer logging was run upwards at a speed of 0.8 m/s and an equal value of 0.00075 m was set for the axial and circumferential resolution values, in order to resolve square elements on the bore hole wall.

In the slot drilling experiment (see Fig. 7.9 (a), (c), (d)), performed at a depth of 13.8 m, a longitudinal slot was opened on the bore hole wall. The opening extension in longitudinal direction is about 20 cm with a quite stable orientation in NE orientation. An relative increase of the bore hole radius by a factor of about 50% is measured, with a maximum increase of 25 mm from the initial radius of 43 mm.

The result of the notch drilling experiment, carried out at a shallower depth of 7.5 m are shown in Fig. 7.9 (b). A notch-like opening with a preferential orientation in SW-N direction is created. As shown in Fig. 7.9 (d), the bore hole radius is enlarged by a factor larger than 2 in two defined regions (SW and NNW orientation) and probably significantly larger in a third region (WNW orientation). Thereby, the maximum depth of this third region could not be measured accurately, as the value exceeds the maximum sonde threshold. Indeed, in the region with orientation WNW, the maximum penetration into the formation occurred, which is further observed from the bore hole camera, (Fig. 7.2.2(f), lower left corner). In the remaining circumference of the bore hole, the diameter could only be slightly increased, *e.g.* by 21% from the initial bore hole radius in E orientation. The asymmetry of the shape is due to the fact that the most pronounced exportation (WNW orientation) occurs at the orientation where the nozzle was located at ignition of the burner and the manual turning process was not conducted at a steady pace, which did not allow the flame to excavate all areas equally. Nevertheless, these two experiments proof the applicability of the process in hard formations and the operational readiness of the proposed system.

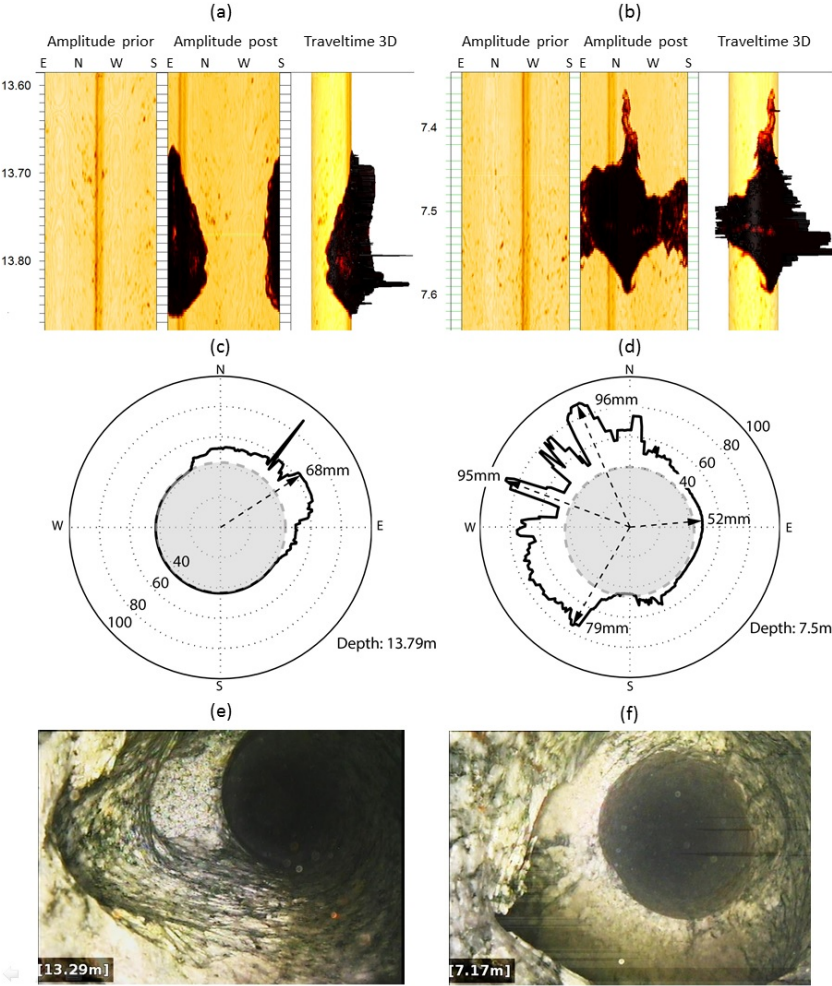


Figure 7.9: Unwrapped amplitude plot prior and after the hole opening process for (a) the slot geometry (b) and the notch opening, with a 3D bore hole image. Cross section of (c) the slot opening and (d) the notch opening. Image from a down hole camera: (e) slot geometry; (f) notch opening.

7.3 Conclusions

Thermal bore hole enlargement is a novel technology, which utilize thermal spallation drilling to enlarge locally the cross section of a well in hard rock sections. Thereby, the hole opening geometry can be selected as required. The technology can be used to remove near well bore impedances, create initial fracture sources and increase the initial size of the reservoir before hydraulic stimulation. These measures will enhance the hydraulic stimulation process, as lower pressures are required and more fractures can be stimulated. The applicability of the technology is shown in a full scale field test, located in the Grimsel Test Site, Switzerland. Two hole opening geometries in a depth of 13.8 m and 7.5 m could be successfully drilling with a methane-air driven burner. Thereby, the radius of the borehole could be increased to a maximum of 2.2 times the initial bore hole radius. This field test puts into evidence the applicability of the process and demonstrates its potential to improve the reservoir creation in deep geothermal systems.

CHAPTER 8

Conclusions & outlook

8.1 Conclusions

The potential of thermal spallation drilling as an alternative technology for deep drilling operations was evaluated in this thesis. Whereas the application of stand-alone spallation drilling for long wells implies certain difficulties, a combination of thermal and mechanical drilling and the use of spallation drilling for bore hole enlargement is promising. During the development of these two systems, a deeper understanding of the physics of the spallation process and their transfer to practical applications could be achieved.

A comprehensive model was introduced to estimate the operating conditions required to initiate spalling of rocks and to assess the maximum velocity possible to drill a certain rock formation. The model was applied in a cost study, which shows that in principle the costs of a geothermal well can be reduced with thermal spallation drilling. Thereby, the largest savings can be achieved by reducing the required tripping times. High drilling velocities do not have a significant effect on the cost structure, as the reduced costs, due to time savings, are compensated by increased costs, due to fuel and compression efforts. Therefore, thermal spallation drilling can have the highest impact, if the postulated reduced tripping efforts, due to low wear rates, can be confirmed in a realistic environment.

Additionally, it is shown that thermal spallation drilling performs well under laboratory conditions, if homogeneous and favorable rock properties are encountered. In real drilling applications, limitations are hindering the applicability of spallation drilling. Non-spallable rock sections, stress relieving fractures and significant intrusions of water into the bore-hole will lead to an interruption of the spallation process. The required temporal change to an mechanical bit is not only time-consuming, but also vanishes most of the discussed benefits of this technology.

This leads to the conclusion that stand-alone spallation is not applicable for drilling long wells in an unknown rock formation and only a combination of thermal spallation drilling with mechanical drilling methods is a reasonable option. This hybrid technology combines the benefits of both drilling technologies and can therewith contribute to the reduction of the drilling costs for geothermal projects. The applicability of this technology was shown in a first feasibility study, where a PDC cutter scratched

the surface of untreated and thermally treated samples. The experimental data allowed to conclude that the implementation of a flame jet as a thermal assistance in conventional drilling could reduce the forces on the drilling tools and in turns also the wearing of drill bits during their operation. Thereby, the application of an air-shield around the flame jet can solve the common entrainment problem. A design for a hybrid drill head to drill a bore hole with a diameter of 140 mm was presented and preliminary tested. This step puts into evidence the general integration possibility of the hybrid drilling concept in real drilling applications.

Beside the integration of thermal spallation drilling in mechanical drilling methods, the technology can also be used to enlarge and enhance an existing bore hole in its production section. This process will reduce stimulation efforts and increase the productivity of an existing well. The feasibility of such a thermal bore hole enlargement process was shown in a field test located in the Grimsel underground laboratory. A system with a length of 25m was used to increase the diameter of an existing bore hole. In two tests the borehole diameter could be locally increased in a depth of 12.5m and 7.5m to a maximum of 2.2 times the original diameter. This shows the operational readiness of this process for deep drilling applications.

Concluding, in the present thesis the potential of thermal spallation drilling as an alternative technology for deep drilling operations was evaluated. Two application possibilities were evaluated, as a suitable option for the integration of thermal spallation drilling. It can be used to enhance the drilling process and to improve the hydraulic stimulation process. These two aspects have been discussed as crucial points for the further development of deep geothermal energy by various authors [7, 8, 11].

8.2 Outlook for future work

Even though the applicability and operational readiness of thermal spallation drilling for certain drilling operations could be shown in the presented thesis, further improvements and development steps are required to enable the use of the presented technologies in deep bore holes.

Model attempts

The presented model can be used to estimate the required operating conditions and the possible drilling velocity. Whereas, the first submodel, evaluating the operating conditions, could be experimentally confirmed, the evaluation of the second submodel (drilling velocity) was only based on some preliminary results published by Hoeser [63]. A further validation of the model would further increase the knowledge of thermal spallation drilling and would provide more accurate design guidelines for thermal spallation tools, which are required for both hybrid drilling operations and thermal bore hole enlargements.

Thermal spallation drilling in deep drilling operations

The presented cost model is based on many assumptions, as only insufficient data for thermal spallation drilling in deep wells were available at the time of publication of this thesis. With increasing experience and knowledge gained during the ongoing field-tests with this technology, the cost model should be updated and further improved. Similarly, the presented limitations of the technology as *e.g.* fractures or soft inclusions are based on personal experience in the lab and field environment. A more detail investigation of these limitations could reveal also other solutions, as a combination of mechanical and thermal drilling methods.

Hybrid drilling

Due to complications in the development of the front face of the drill bit and the swivel and the corresponding delay of several months, the developed hybrid drill head could not be tested in the field. Therefore,

of course, future work should focus on finally testing the complete system. This test would demonstrate the applicability of such a process and would hopefully confirm the discussed benefits of the technology. Further, after a successful demonstration of this combined drilling methods, the design principles of the system should be adjusted towards deep down hole situations. This would require a new supply concept, further simplifications of the overall design and an integration in more complex drill bit faces. Besides the mentioned field tests, further knowledge about the interplay between thermal weakening of the rock structure and wear rate reduction of the mechanical cutters is required for different cutter-rock combinations to estimate the optimal operating conditions of the hybrid drill head. This investigation is important, as the cost study performed in this thesis, showed that the reduction of the wear rate is the most important contributor to cost savings during the drilling process.

Thermal bore hole enhancement

The conducted field test in the Grimsel Test Site showed the applicability and operational readiness of the technology. Thermal bore hole enhancement could be demonstrated for a depth of 12.5m. On a short-term, future work should focus on the further improvement of the used prototype. A new packer system could reduce tripping problems and undesired pressure accumulations around the BHA. A self-rotating nozzle system would eliminate the manual BHA turning process. Thereby, an industrial partner would significantly accelerate the development, as the process engineering design aspects are completed and knowledge in deep drilling operations is required. Furthermore, only hydraulic stimulation experiments, comparing the required efforts on a normal and a thermally enhanced bore hole, would confirm the postulated benefits of the technology. These experiments could be also performed in the Grimsel Test Site, but would require substantial financial and human resources, as the *In-situ* Stimulation and Circulation (ISC) experiment of ETH Zurich showed. On a medium- to long-term perspective, the application of the technology in a deep bore hole (>2000m) seems to be the next logical step, as the operational readiness for this kind of application was shown.

APPENDIX A

Appendix

A Complete description of the matrix structure

The proposed numerical technique is based on Duhamel's theorem. The derivation of this theorem can be widely found in literature [90, 92, 93]. It is based on the principle of superposition and connects the temperature linearly with the heat flux at any point in space and time. The theorem can be written as:

$$\mathbf{T} = \mathbf{X} \cdot \mathbf{q} + \mathbf{T}_0 \quad (\text{A.1})$$

where \mathbf{T} is the temperature field containing the temperature information for all observers at every time step, \mathbf{X} the so called sensitivity matrix, \mathbf{q} the heat flux values for all heat flux elements at every time step and \mathbf{T}_0 the temperature field at the initial conditions ($t < 0$). The sensitivity values inside the sensitivity matrix \mathbf{X} are defined as the first derivative of the temperature response v at a specific temperature observer location (i_T, j_T) and time t_T , with respect to a heat flux unit pulse at another specific location (i_q, j_q) and time t_q (equation A.2) [90].

$$X_{i_T, j_T, i_q, j_q} = \left. \frac{\partial v(i_T, j_T, t_T)}{\partial q(i_q, j_q, t_q)} \right|_{q=1 \text{ W/m}^2} \quad (\text{A.2})$$

If equation A.1 is solved for \mathbf{q} , the heat flux distribution can be estimated, if the temperature field, the initial conditions and the sensitivity matrix are known (equation A.3).

$$\mathbf{q} = \text{inv}(\mathbf{X}) \cdot (\mathbf{T} - \mathbf{T}_0) \quad (\text{A.3})$$

Thereby, for n time steps and for all elements, the time-vector of \mathbf{T} , the time-sensitivity matrix \mathbf{X} and the heat flux time-vector \mathbf{q} are defined by equations A.4 to A.6.

$$\mathbf{T} = \begin{pmatrix} T_1 \\ T_2 \\ \vdots \\ T_n \end{pmatrix} \quad (\text{A.4})$$

$$\mathbf{X} = \begin{pmatrix} \mathbf{X}_1 & 0 & 0 & \cdots & 0 \\ \mathbf{X}_2 & \mathbf{X}_1 & 0 & \cdots & 0 \\ \mathbf{X}_3 & \mathbf{X}_2 & \mathbf{X}_1 & \cdots & 0 \\ \vdots & \vdots & \vdots & \ddots & \vdots \\ \mathbf{X}_n & \mathbf{X}_{(n-1)} & \mathbf{X}_{(n-2)} & \cdots & \mathbf{X}_1 \end{pmatrix} \quad (\text{A.5})$$

$$\mathbf{q} = \begin{pmatrix} \mathbf{q}_1 \\ \mathbf{q}_2 \\ \vdots \\ \mathbf{q}_n \end{pmatrix} \quad (\text{A.6})$$

It has to be considered that all components of the vectors and the matrix stated above are vectors and matrices themselves containing the temperature, heat flux and sensitivity values of each heat flux element and temperature observer for the associated time step. Therefore, these vectors and matrices can be further divided to receive the formulation for the single temperature observers, heat flux elements and sensitivity values at an arbitrarily chosen time step r :

$$\mathbf{T}_r = \begin{pmatrix} T_{1,1,r} \\ T_{1,2,r} \\ \vdots \\ T_{1,j,r} \\ T_{2,1,r} \\ \vdots \\ T_{i,j,r} \end{pmatrix} \quad (\text{A.7})$$

$$\mathbf{X}_r = \begin{pmatrix} X_{1,1,r} & X_{1,2,r} & \cdots & X_{1,j,r} & X_{2,1,r} & \cdots & X_{i,j,r} \\ X_{1,2,r} & X_{1,1,r} & \cdots & X_{2,1,r} & X_{1,j,r} & \cdots & X_{i,j-1,r} \\ \vdots & \vdots & \ddots & \vdots & \vdots & \ddots & \cdots \\ X_{1,j,r} & X_{2,1,r} & \cdots & X_{1,1,r} & X_{1,2,r} & \cdots & X_{i,1,r} \\ X_{2,1,r} & X_{1,j,r} & \cdots & X_{1,2,r} & X_{1,1,r} & \cdots & X_{i-1,1,r} \\ \vdots & \vdots & \ddots & \vdots & \vdots & \ddots & \cdots \\ X_{i,j,r} & X_{i,j-1,r} & \cdots & X_{i,1,r} & X_{i-1,1,r} & \cdots & X_{1,1,r} \end{pmatrix} \quad (\text{A.8})$$

$$\mathbf{q}_r = \begin{pmatrix} q_{1,1,r} \\ q_{1,2,r} \\ \vdots \\ q_{1,j,r} \\ q_{2,1,r} \\ \vdots \\ q_{i,j,r} \end{pmatrix} \quad (\text{A.9})$$

In equation A.8, the sensitivity field is considered as symmetrical, meaning that a heat flux element at position (k, l) has the same sensitivity on the observer at position (m, n) as the element at position (m, n) on the observer at (k, l) .

In general, the number of temperature observers has to be always equal or larger than the number of heat flux elements, so that the linear equation system described by equation A.3 is not underdetermined. If, the number of temperature observers exceeds the number of heat flux elements, the different vectors and matrices can be arranged in the same way, if the heat flux value at the position of the additional temperature observer is set to zero.

The problem which was formulated by equations A.4 to A.9 can be reduced to a 2D mathematical description by combining the time matrices (equations A.4 to A.6) and space matrices (equations A.7 to A.9) of the individual components. This is exemplary shown for a system with $K_y = 1$, $K_z = 2$ heat flux elements and observers and four time steps in

equation A.10, with the initial temperature field set to zero.

$$X = \begin{pmatrix} X_{1,1,1} & X_{1,2,1} & 0 & 0 & 0 & 0 & 0 & 0 \\ X_{1,2,1} & X_{1,1,1} & 0 & 0 & 0 & 0 & 0 & 0 \\ X_{1,1,2} & X_{1,2,2} & X_{1,1,1} & X_{1,2,1} & 0 & 0 & 0 & 0 \\ X_{1,2,2} & X_{1,1,2} & X_{1,2,1} & X_{1,1,1} & 0 & 0 & 0 & 0 \\ X_{1,1,3} & X_{1,2,3} & X_{1,1,2} & X_{1,2,2} & X_{1,1,1} & X_{1,2,1} & 0 & 0 \\ X_{1,2,3} & X_{1,1,3} & X_{1,2,2} & X_{1,1,2} & X_{1,2,1} & X_{1,1,1} & 0 & 0 \\ X_{1,1,4} & X_{1,2,4} & X_{1,1,3} & X_{1,2,3} & X_{1,1,2} & X_{1,2,2} & X_{1,1,1} & X_{1,2,1} \\ X_{1,2,4} & X_{1,1,4} & X_{1,2,3} & X_{1,1,3} & X_{1,2,2} & X_{1,1,2} & X_{1,2,1} & X_{1,1,1} \end{pmatrix} \quad (\text{A.10})$$

B Physical properties of the spallability map

Table A.1: Physical properties of the investigated rock samples; data obtained from literature at room temperature; * property has been measured by the author

Properties	Font.	Rors.	Berea	C. Aare	West.	Sioux	Äspö
E	72	12*	13.5	38.7	59	62	76
$[GPa]$			[186, 187]	[78, 80]	[188-190]	[187, 191]	[192]
ν	0.12	0.16*	0.34	0.33	0.25	0.14	0.25
$[-]$	[193]		[186, 187]	[80]	[188, 190]	[187, 194]	[192]
K_{IC}	0.64	0.47*	1.3	0.64	1.80	2.5	3.5
$[MPa\,m^{0.5}]$			[195, 196]	[81]	[152, 197]	[197]	[198]
α	7.70	8.29*	16	8.4*	7.6	26	7.4
$[10^{-6}\,1/K]$			[199]		[99, 200]	[201-203]	[192, 204]
λ	4.9	2.62*	2.5	3.2	2.4	5.5	2.53
$[W/(m\,K)]$	[205]		[206, 207]	[76, 80]	[206, 208]	[206, 209]	[192, 204]

C Cost tables of the case study

Table A.2: Fixed costs accounted for the cost assessment; all numbers in USD; data from [28]; ⁻ reduced values, due to the use of the spallation technology (with original numbers in brackets), ⁺ increased values, due to the use of the spallation technology (with original numbers in brackets)

Position	Quant.	Unit cost	Tot. costs
Well insurance	1	25,000	25,000
Drilling fluids			
Materials	1	411,000	411,000
Shaker screens	50	500	25,000
Cementing			
Materials	1	3,672,000	3,672,000
Drilling tools			
Stabilizers, reamer	92	900	82,800
Rebuild charges	2	45,000	90,000
Drill pipe repair	92	900	82,800
Well control			
BOP inspect./repair	3	10,000	30,000
BOP consumables	1	20,000	20,000
Rot. head rubbers	5	1,500	7,500
Drill pipe floats	20	500	10,000
Transportation			
Equipment transport	143	500	71,500
Bits			
Surface hole 36in	1	80,000	80,000
Interm.hole 1 26in	1 ⁻ (4)	110,000 ⁺ (85,000)	110,000
Prod. hole 1 17-1/2in	1 ⁻ (3)	65,000 ⁺ (50,000)	65,000
Prod. hole 2 12-1/4in	1 ⁻ (6)	32,500 ⁺ (25,000)	32,500
Prod. hole 3 8-1/2in	1 ⁻ (4)	20,800 ⁺ (16,000)	20,800
Casing accessories			
Liner services	3	35,000	105,000
Centralizers	1	25,000	25,000
Float shoes/collars	1	57,000	57,000
Casing Crew	7	10,000	70,000

Production equipment			
Casing heads	3	15,000	45,000
Valves	6	15,000	90,000
Nuts, studs, gages	1	10,000	10,000
Wellhead installation	1	12,000	36,000
$\sum C_{f,i}$ fixed costs			5,273.900

Table A.3: Variable costs on a daily basis accounted for the cost assessment; all numbers in USD; data from [28], ⁻ reduced values, due to the use of the spallation technology (with original numbers in brackets), ⁺ increased values, due to the use of the spallation technology (with original numbers in brackets) * estimated costs for specific spallation tools

Position	Quant.	Unit Cost	Daily est cost
Drill rig			
Rig day rate	1	30,000 ⁺ (28,000)	30,000
Top Drive rental	1	3,200	3,200
Fuel (gal/day)	1000 ⁻ (2500)	4	4,000
Rig services	1	700	700
Rig crew	1	1,000	1,000
Rig management	1	4,000	4,000
Project management	1	1,000	1,000
Drilling fluids			
Engineer	1	900	4,000
Shakers	3	400	1,200
Mud cooler	1	750	750
Sumless services	1	1500	1,500
Directional services			
Equipment	1	12,000	12,000
Personnel	1	2,000	2,000
Geological services			
Mud Logging	1	2,000	2,000
H2S Monitoring	1	750	750
Geologic Services	1	400	400

Drilling tools			
Jars etc.	1	800	800
Drill pipes ⁺	1	(150) 300	300
Inspections	1	1000	1,000
Well control			
BOP rental	1	2,000 ⁺ (1500)	2,000
Rotating head	1	350	350
Rig site logistics			
Communications	1	250	250
Monitoring sys.	1	500 ⁺ (250)	500
Living Accom.	1	500	500
Water and Power	1	150	150
Spallation equipment			
Fuel compressor rental*	1	2,000	2,000
Fuel storage*	1	1000	1,000
Air compressor rental*	1	2,000	2,000
Top Drive mod*	1	1000	1,000
Safety*	1	500	500
Misc.*	1	1,000	1,000
Methane	tbd	0.25 /m ³	tbd
Air compress variabl	tbd	0.05 /m ³	tbd
Fuel compress variabl	tbd	0.05 /m ³	tbd
$\sum C_{t,j}$ daily costs	82,650 /D		
$\sum C_{t,fuel,spec}$	0.35 /m³		
$\sum C_{t,oxy,spec}$	0.10 /m³		

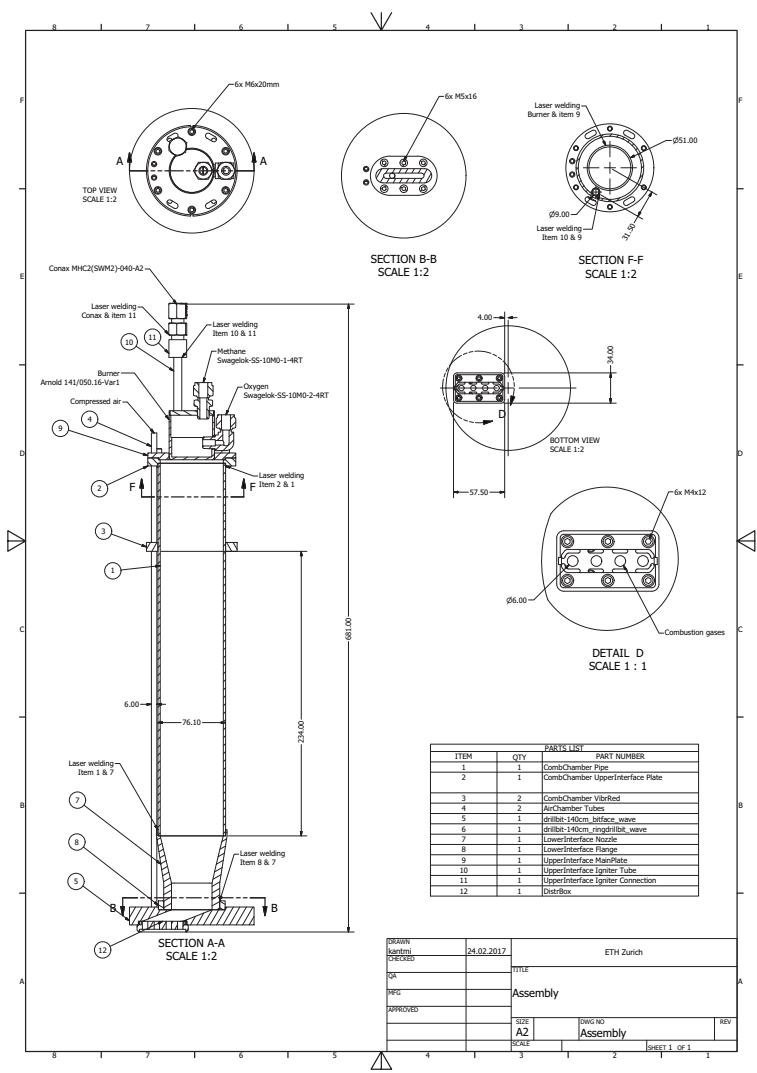
Table A.4: Variable costs based on the length accounted for the cost assessment; all numbers in USD; data from [28], ⁻ reduced values, due to the use of the spallation technology (with original numbers in brackets)s, ⁺ increased values, due to the use of the spallation technology (with original numbers in brackets) * estimated costs for specific spallation tools.

Position	Length (ft)	Unit Cost	Tot. est cost
Casing			
Conductor Pipe	50	400	20,000
Surface Casing	500	300	150,000
Interm. Casing	5000	190	950,000
Prod. Liner 1	5200	216	1,123,200
Prod. L-1 Tie-Back	4800	235	1,128,000
Prod. Liner 2	7200	98	705,600
Prod. Liner 3	3200	68	217,600
$\sum C_{v,k}$			4,294,400

Table A.5: Time schedule for the project; all numbers in days; data from [28], ⁻ reduced values, due to the use of the spallation technology (with original numbers in brackets)s, ⁺ increased values, due to the use of the spallation technology (with original numbers in brackets) * estimated costs for specific spallation tools.

Task	Scheduled time
Preperation D_{prep}	4.7
Drilling D_d	tbd
Tripping D_{trip}^-	(31.4) 15.7
Casing/Cementing D_{cas}	12
Other tasks D_{misc}	33.5

D Technical drawing of the hybrid head



Bibliography

- [1] International Energy Agency, Key Electricity Trends, Excerpts from: Electricity Information 2016. Report, 2016.
- [2] G. Thürler. Statistik der Wasserkraftanlagen der Schweiz. Report, Bundesamt für Energie, 2016.
- [3] G. Walker. Renewable energy and the public. *Land Use Policy*, 12(1):49–59, 1995.
- [4] P. Manso, A. J. Schliess, M. Stähli, and F. Avellan. Electricity supply and hydropower development in Switzerland. *International Journal on Hydropower and Dams*, 23(5):41–47, 2016.
- [5] M. Barry, P. Baur, L. Gaudard, G. Giuliani, W. Hediger, F. Romeo, M. Schillinger, R. Schumann, G. Voegeli, and H. Weigt. The future of swiss hydropower-a review on drivers and uncertainties, WWZ Working Paper 2015/11. Report, Center of Business and Economics (WWZ), University of Basel., 2015.
- [6] P. Previdoli. Infoanlass Energiestrategie 2050. Report, Schweizer Bundesamt für Energie, 2012.
- [7] J. W. Tester et al. *The future of geothermal energy - Impact of enhanced geothermal systems (EGS) on the United States in the 21st century: An assessment*. Idaho National Laboratory, Idaho Falls, 2007.
- [8] S. Hirschberg, S. Wiemer. *Energy from the earth: deep geothermal as a resource for the future*. 2015.
- [9] Mary H Dickson and Mario Fanelli. *Geothermal energy: utilization and technology*. Routledge, 2013.
- [10] International Energy Agency, World Energy Outlook 2013. Report, 2013.
- [11] B. Sigfusson and A. Uihlein. 2014 JRC geothermal energy status report. *Luxembourg: Publications Office of the European Union*, 2015.

- [12] K. Breede, K. Dzebisashvili, and G. Falcone. Overcoming challenges in the classification of deep geothermal potential. *Geoth. Energ. Sci.*, 3(1):19–39, 2015.
- [13] Domenico Giardini. Geothermal quake risks must be faced. *Nature*, 462(7275):848–849, 2009.
- [14] P. Meier, A. Rodriguez, and F. Bethmann. Lessons learnt from Basel: New EGS projects in Switzerland using multistage stimulation and a probabilistic traffic light system for the reduction of seismic risk. In *Proceedings World Geothermal Congress 2015, Melbourne, Australia, 19-25 April 2015*, 2015.
- [15] J. Baumgaertner, T. Gandy, T. Hettkamp, and Dimitra Teza. Drilling of hot and fractured granite at Soultz-sous-Forêts. In *Engine Mid-Term Conference, GFZ Potsdam*.
- [16] R. Bertani. Geothermal power generation in the world 2005-2010 update report. *Geothermics*, 41:1–29, 2012.
- [17] K. Link, L. Rybach, S. Imhasly, and R. Wyss. Geothermal energy in Switzerland, country update. In *World Geothermal Congress 2015, Melbourne, Australia, 19-25 April 2015*.
- [18] B. Sanner, C. Karytsas, D. Mendrinós, and L. Rybach. Current status of ground source heat pumps and underground thermal energy storage in Europe. *Geothermics*, 32(4-6):579–588, 2003.
- [19] Th. Megel and L. Rybach. Production capacity and sustainability of geothermal doublets. In *World Geothermal Congress 2000, Kyushu - Tohoku, Japan, May 28 - June 10, 2000*.
- [20] G. Siddiqi and R. Minder. The swiss federal office of energies path on the road to utilizing switzerlands geothermal resources - from research and development to pilot-and demonstration projects. *Swiss bulletin for applied geology*, 15, 2015.
- [21] M. Allen, P. Avato, M. Gehringer, T. Harding-Newman, J. Levin, V. B. Loksha, Z. Meng, S. Moin, J. Morrow, A. O. Oduolowu, A. Pantelias, and S. K. Sanyal. Success of geothermal wells: A global study. Report, World Bank Group, 2013.

- [22] M. Gehringer and V. Loksha. Geothermal handbook: planning and financing power generation. Report, ESMAP, 2012.
- [23] E. L. Majer, R. Baria, M. Stark, St. Oates, J. Bommer, B. Smith, and H. Asanuma. Induced seismicity associated with enhanced geothermal systems. *Geothermics*, 36(3):185–222, 2007.
- [24] B. Edwards, T. Kraft, C. Cauzzi, P. Kaestli, and S. Wiemer. Seismic monitoring and analysis of deep geothermal projects in St. Gallen and Basel, Switzerland. *Geophysical Journal International*, 201(2):1020–1037, 2015.
- [25] M. Kant, T. Meier, Edoardo Rossi, M. Schuler, Dustin Becker, Dragana Höser, and P. Rudolf Von Rohr. Thermal spallation drilling - an alternative drilling technology for hard rock drilling. *OIL GAS European Magazin*, 3, 2017:23–25, 2017.
- [26] M. Kant, E. Rossi, D. Höser, and P. Rudolf von Rohr. Thermal spallation drilling, an alternative drilling technology for deep heat mining-performance analysis, cost assessment and design aspects. In *41st Workshop on Geothermal Reservoir Engineering, Stanford University, Stanford, California, February 13-15, 2017*.
- [27] W. Lyons and G. J. Plisga. *Standard Handbook of Petroleum and Natural Gas Engineering (Second Edition)*. Gulf Professional Publishing, Burlington, 2004.
- [28] Y. Polsky, L. Capuana, J.T. Finger, M Huh, S. Knudsen, A. Chip Mansure, D. Raymond, and R. Swanson. Sand2008-7866: Enhanced geothermal systems (EGS) well construction technology evaluation report. Report, Sandia National Laboratory, 2008.
- [29] D. Finger, J.T. Blankenship. *Handbook of Best Practices for Geothermal Drilling*. Sandia National Laboratories, 2010.
- [30] Paul K Ngugi. Geothermal well drilling. In *Short Course III on Exploration for Geothermal Resources, Lake Naivasha, Kenya, 2008*.
- [31] G. Bruton, R. Crockett, M. Taylor, D. DenBoer, J. Lund, C. Fleming, R. Ford, G. Garcia, and A. White. PDC bit technology for the 21st century. *Oilfield Review*, 26(2 (2014)), 2014.

- [32] F. Jahn, M. Cook, and M. Grahm. Chapter 4 drilling engineering. *Developments in Petroleum Science*, 55:47–81, 2008.
- [33] J. L. Williams and A. I. Thompson. An analysis of the performance of PDC hybrid drill bits. In *SPE/IADC Drilling Conference, 15-18 March, New Orleans, Louisiana*.
- [34] C. Durrand, M. Skeem, R. Crockett, and D. Hall. Super-hard, thick, shaped PDC cutters for hard rock drilling: development and test results. In *Thirty-Fifth Workshop on Geothermal Reservoir Engineering, Stanford University, Stanford, California, 2010*.
- [35] R. Pessier and M. Damschen. Hybrid bits offer distinct advantages in selected roller-cone and PDC-bit applications. *SPE Drilling and Completion*, 2011.
- [36] L. Okwiri. Geothermal drilling time analysis: A case study of Menengai and Hengill. In *World Geothermal Congress 2015, Melbourne, Australia, 19-25 April 2015*.
- [37] Bruce H. Walker. Some technical and economic aspects of stabilizer placement. *Journal of Petroleum Technology*, 25(06), 1973.
- [38] American Petroleum Institute, recommended practice 54 - recommended practice for occupational safety for oil and gas well drilling and servicing operations, 2007.
- [39] L. M Edwards, G. V. Chilingar, H. H. Rieke, and W. H. Fertl. *Handbook of geothermal energy*. Gulf Publishing Company, Houston, TX, United States, 1982.
- [40] Erik Nelson. Well cementing fundamentals. *Oilfield Review*, 24(2), 2012.
- [41] M. Schuler. *Fundamental Investigations of Supercritical Water Flows for Hydrothermal Spallation Drilling, ETH Zurich, Thesis No. 21803*. Thesis, 2014.
- [42] M. Lukawski, B. J. Anderson, C. Augustine, L. Capuano Jr, K. Beckers, B. Livesay, and J. Tester. Cost analysis of oil, gas,

- and geothermal well drilling. *Journal of Petroleum Science and Engineering*, 118:1–14, 2014.
- [43] S. D. Hillson and J. W. Tester. Heat transfer properties and dissolution behavior of barre granite as applied to hydrothermal jet drilling with chemical enhancement. In *40th Workshop on Geothermal Reservoir Engineering, Stanford, California*. Int. Geoth. Assoc.
- [44] I. V. Timoshkin, J. W. Mackersie, and S. J. MacGregor. Plasma channel microhole drilling technology. In *14th IEEE International Pulsed Power Conference, 2003*, volume 2, pages 1336–1339 Vol.2.
- [45] I. Kocis, T. Kristofic, M. Gajdos, G. Horvath, and S. Jankovic. Utilization of electrical plasma for hard rock drilling and casing milling. In *SPE/IADC Drilling Conference and Exhibition, 17-19 March, London, England, UK*. Society of Petroleum Engineers.
- [46] K. Bybee. Modeling laser-spallation rock drilling. *Journal of Petroleum Technology*, 58(02), 2006.
- [47] M. Kant, E. Rossi, C. Madonna, D. Höser, and P. Rudolf von Rohr. A theory on thermal spalling of rocks with a focus on thermal spallation drilling. *Journal of Geophysical Research: Solid Earth*, 122(3):1805–1815, 2017.
- [48] F. W. Preston and H. E. White. Observations on spalling. *Journal of the American Ceramic Society*, 17:137–144, 1934.
- [49] L. Germanovich. Thermal spalling of rock. *Advances in Fracture Research*, 6:2771–2782, 1997.
- [50] R. M. Rauenzahn and J. W. Tester. Rock failure mechanisms of flame-jet thermal spallation drilling - theory and experimental testing. *International Journal of Rock Mechanics and Mining Sciences and Geomechanics Abstracts*, 26(5):381–399, 1989.
- [51] P. Stathopoulos. *Hydrothermal spallation drilling experiments in a novel high pressure pilot plant*. PhD thesis, Diss. No 21163, 2013.

- [52] T. Meier, P. Stathopoulos, and Ph Rudolf von Rohr. Hot surface ignition of oxygen-ethanol hydrothermal flames. *The Journal of Supercritical Fluids*, 107:462–468, 2016.
- [53] P. Rudolf von Rohr, T. Rothenfluh, and M. Schuler. Rock drilling in great depths by thermal fragmentation using highly exothermic reactions evolving in the environment of a water-based drilling fluid, US Patent US20110303460 A1, 2011.
- [54] C. Augustine and J. W. Tester. Hydrothermal flames: From phenomenological experimental demonstrations to quantitative understanding. *The Journal of Supercritical Fluids*, 47(3):415–430, 2009.
- [55] C. R. Augustine. Hydrothermal spallation drilling and advanced energy conversion technologies for engineered geothermal systems. *PhD thesis, Massachusetts Institute of Technology*, 2009.
- [56] J. J. Calaman and H. C. Rolseth. *Jet Piercing, In E. Pfeleider, Surface Mining (first edition)*. 1968.
- [57] M. C. Sheppard, C. Wick, and T. Burgess. Designing well paths to reduce drag and torque. *SPE Drilling Engineering*, 2(4), 1987.
- [58] J. A. Browning, W. B. Horton, and H. L. Hartman. Recent advances in flame-jet working of minerals. *7th Symposium on Rock Mechanics*, pages 281–324, 1965.
- [59] M. Schuler, T. Rothenfluh, and Ph. Rudolf von Rohr. Simulation of the thermal field of submerged supercritical water jets at near-critical pressures. *The Journal of Supercritical Fluids*, 75(0):128–137, 2013.
- [60] M. A. Kant and P. Rudolf von Rohr. Minimal required boundary conditions for the thermal spallation process of granitic rocks. *International Journal of Rock Mechanics and Mining Sciences*, 84:177–186, 2016.
- [61] O. Vestavik, S. Brown, and S. Kerr. Reelwell drilling method. *SPE/IADC Drilling Conference and Exhibition, 17-19 March, Amsterdam, Netherlands*, 2009.

- [62] T. Butler, P. Fontana, and R. Ottawa. A method for combined jet and mechanical drilling. In *SPE Annual Technical Conference and Exhibition, 23-26 September, New Orleans*.
- [63] D. Hoesser. *Flame-jet assisted drilling technology. 2016, PhD Thesis No. 23896, ETH Zurich*. Thesis, 2016.
- [64] K. G. Pierce, B. J. Livesay, and John T. Finger. Advanced drilling systems study. Technical Report SAND95-0331, Technical Report, SAND95-0331, Sandia National Laboratories, 1996.
- [65] R. Rinaldi. A technical and economic evaluation of thermal spallation drilling technology. Report, Sandia National Laboratories, USA, 1984.
- [66] J. A. Browning. Flame jet gains ground as blast hole drill. *Engineering and Mining Journal*, 1969.
- [67] R.M. Potter and J.W. Tester. Continuous drilling of vertical boreholes by thermal processes: including rock spallation and fusion, US Patent US5771984 A, 1998.
- [68] T.W. Wideman, J.M. Potter, D. Dreesen, and R.M. Potter. Methods and apparatus for thermal drilling, US Patent US8235140 B2, 2012.
- [69] M. A. Wilkinson and J. W. Tester. Experimental measurement of surface temperatures during flame-jet induced thermal spallation. *Rock Mechanics and Rock Engineering*, 26(1):29–62, 1993.
- [70] R. M. Rauenzahn. *Analysis of Rock Mechanics and Gas Dynamics of Flame-Jet Thermal Spallation Drilling, PhD Thesis Massachusetts Institute of Technology*. Thesis, 1986.
- [71] St. Walsh, I. Lomov, and J. Roberts. Geomechanical modeling for thermal spallation drilling. *GRC Transactions*, 35:277–282, 2011.
- [72] K. Prikopsky, P. Rudolf von Rohr, and T. Rothenfluh. Flames in supercritical water and their applications. *Strojnický Casopis*, 59(2):91–103, 2008. Slovakia.

- [73] T. Rothenfluh. *Heat Transfer Phenomena of Supercritical Water Jets in Hydrothermal Spallation Drilling*, PhD thesis, Diss. No. 21001, ETH Zurich. Thesis, 2013.
- [74] R. Ndeda, S. Sebusang, R. Maruma, and E. Ogur. Review of thermal surface drilling technologies. In *Sustainable Research and Innovation (SRI) Conference*.
- [75] C. Teodoriu and C. Cheuffa. A comprehensive review of past and present drilling methods with application to deep geothermal environment. In *36th. Workshop on Geothermal Reservoir Engineering*. Int. Geoth. Assoc.
- [76] M. Kant, J. Ammann, E. Rossi, C. Madonna, D. Hoeser, and P. Rudolf von Rohr. Thermal properties of grimsel granodiorite for temperatures up to 500°C: irreversible changes due to thermal crack formation. *Geophysical Research Letters*, 44(2):771–776, 2016.
- [77] A. Pahl, St. Heusermann, V. Braeuer, and W. Gloeggler. Nagra report 88-39E: Grimsel Test Site: rock stress investigations. Report, Nagra, Schweiz, 1989.
- [78] T. Pilgerstorfer, H. Wannenmacher, K. Grossauer, A. Stucki, and B. Schwegler. Rock mechanical aspects for cavern stability. In *ISRM International Symposium - EUROCK 2013, 23-26 October, Wroclaw, Poland*, pages 151–156. CRC Press.
- [79] J. Rutqvist and C. F. Tsang. A fully coupled three-dimensional thm analysis of the febex in situ test with the rocmas code: Prediction of thm behavior in a bentonite barrier. *Elsevier Geo-Engineering Book Series*, 2:143–148, 2004.
- [80] H. Keusen, Ganguin J., P Schuler, and M Buletti. Nagra NTB 87-14E: Grimsel Test Site - Geology. Report, Nagra, 1989.
- [81] T. Kazerani and J. Zhao. A microstructure-based model to characterize micromechanical parameters controlling compressive and tensile failure in crystallized rock. *Rock Mechanics and Rock Engineering*, 47(2):435–452, 2014.

- [82] A. Moeri, M. Mazurek, M. Adler, M. Schild, S. Siegesmund, A. Vollbrecht, K. Ota, T. Ando, W.R. Alexander, A. Smith, P. Haag, and Ch. Buehler. Nagra report NTB 00-09: The Nagra-JNC in situ study of safety relevant radionuclide retardation in fractured crystalline rock IV: The in situ study of matrix porosity in the vicinity of a water conducting fracture. Report, NAGRA, 2003.
- [83] A. Gens, A. J. Garcia-Molina, S. Olivella, E. E. Alonso, and F. Huertas. Analysis of a full scale in situ test simulating repository conditions. *International Journal for Numerical and Analytical Methods in Geomechanics*, 22(7):515–548, 1998.
- [84] T. E. Diller. *Advances in Heat Flux Measurements in Advances in Heat Transfer*. Elsevier, 1993.
- [85] P. Childs, J. Greenwood, and C. Long. Heat flux measurement techniques. *Proceedings of the Institution of Mechanical Engineers, Part C: Journal of Mechanical Engineering Science*, 213(7):655–677, 1999.
- [86] P. Stathopoulos, F. Hofmann, T. Rothenfluh, and P. Rudolf Von Rohr. Calibration of a gardon sensor in a high-temperature high heat flux stagnation facility. *Experimental Heat Transfer*, 25(3):222–237, 2012.
- [87] T. Meier, P. Stathopoulos, and Ph Rudolf von Rohr. Design and convective calibration of a transverse heat flux sensor. *Experimental Heat Transfer*, 29(2,2016), 2014.
- [88] C. K. Ho, A. R. Mahoney, Andrea Ambrosini, Marlene Bencomo, Aaron Hall, and T. N. Lambert. Characterization of Pyromark 2500 paint for high-temperature solar receivers. *J. Sol. Energy Eng.*, 136, 2013.
- [89] W. M. Pitts, E. Braun, R. Peacock, H. Mitler, E. Johnson, P. Reneke, and L. Blevins. Temperature uncertainties for bare-bead and aspirated thermocouple measurements in fire environments. *ASTM Special Technical Publication*, 1427:3–15, 2003.

- [90] J. V Beck, B Blackwell, and C.R. St. Clair. *Inverse Heat Conduction. Ill-Posed Problems*. John Wiley and Sons, Inc., New York, 1985.
- [91] L. Michalski, K. Eckersdorf, J. Kucharski, and J. McGhee. *Temperature Measurement*. John Wiley and Sons, Ltd, 2002.
- [92] A.N. Tikhonov and V.I.A. Arsenin. *Solutions of ill-posed problems*. Winston and Sons, 1977.
- [93] K. A. Woodbury. *Inverse Engineering Handbook*. CRC Press, 2002.
- [94] M. A. Kant and P. Rudolf von Rohr. Determination of surface heat flux distributions by using surface temperature measurements and applying inverse techniques. *International Journal of Heat and Mass Transfer*, 99:1–9, 2016.
- [95] Yunus A Cengel, Sanford Klein, and William Beckman. *Heat transfer: a practical approach*. WBC McGraw-Hill Boston, 1998.
- [96] V. Hindasageri, R. P. Vedula, and S. V. Prabhu. Heat transfer distribution for impinging methane air premixed flame jets. *Applied Thermal Engineering*, 73(1):461–473, 2014.
- [97] C. L. Rosenberg and M. R. Handy. Experimental deformation of partially melted granite revisited: implications for the continental crust. *Journal of Metamorphic Geology*, 23(1):19–28, 2005.
- [98] M. Friedman, J. Handin, N. G. Higgs, and J. R. Lantz. Strength and ductility of four dry igneous rocks at low pressures and temperatures to partial melting. In *20th U.S. Symposium on Rock Mechanics, Austin, Texas*. American Rock Mechanics Association.
- [99] F. E. Heuze. High-temperature mechanical, physical and thermal properties of granitic rocks - a review. *International Journal of Rock Mechanics and Mining Sciences and Geomechanics Abstracts*, 20(1):3–10, 1983.
- [100] D. P. H. Hasselman. Unified theory of thermal shock fracture initiation and crack propagation in brittle ceramics. *Journal of the American Ceramic Society*, 52(11):600–604, 1969.

- [101] ISO 18434-1:2008(e) Condition monitoring and diagnostics of machines - thermography - part1: General procedures, 2008.
- [102] R. Viskanta. Heat transfer to impinging isothermal gas and flame jets. *Experimental Thermal and Fluid Science*, 6(2):111–134, 1993.
- [103] T. Meier, D. A. May, and Ph Rudolf von Rohr. Numerical investigation of thermal spallation drilling using an uncoupled quasi-static thermoelastic finite element formulation. *Journal of Thermal Stresses*, 39(9):1138–1151, 2016.
- [104] R. Dunham. Classification of carbonate rocks according to depositional textures *in* classification of carbonate rocks -a symposium. pages 108–121, 1962.
- [105] G. Nichols. *Sedimentology and stratigraphy*. John Wiley and Sons, 2009.
- [106] M. J. Heap, Y. Lavallee, L. Petrakova, P. Baud, T. Reuschl, N. R. Varley, and D. B. Dingwell. Microstructural controls on the physical and mechanical properties of edifice-forming andesites at volcn de colima, mexico. *Journal of Geophysical Research: Solid Earth*, 119(4):2925–2963, 2014.
- [107] J. T. Fredrich and T. Wong. Micromechanics of thermally induced cracking in three crustal rocks. *Journal of Geophysical Research: Solid Earth*, 91(B12):12743–12764, 1986.
- [108] T. J. Lu and N. A. Fleck. The thermal shock resistance of solids. *Acta Materialia*, 46(13):4755–4768, 1998.
- [109] G. Siddiqi and B. Evans. Permeability and thermal cracking at pressure in sioux quartzite. *Geological Society, London, Special Publications*, 409(1):49–66, 2015.
- [110] H. F. Wang, B. P. Bonner, S. R. Carlson, B. J. Kowallis, and H. C. Heard. Thermal stress cracking in granite. *Journal of Geophysical Research: Solid Earth*, 94(B2):1745–1758, 1989.

- [111] L. G. Zhao, T. J. Lu, and N. A. Fleck. Crack channelling and spalling in a plate due to thermal shock loading. *Journal of the Mechanics and Physics of Solids*, 48(5):867–897, 2000.
- [112] J. C. Carslaw, H.S Jaeger. *Conduction of Heat in Solids*. Oxford University Press, New York, USA, second edition edition, 1959.
- [113] D. Hahn and M. N. Oezisik. *Heat Conduction*. John Wiley and Sons, Inc., 2012.
- [114] T. von Boeckh, P. Wetzel. *Heat Transfer, Basics and Practice*. Springer, Karlsruhe, 2012.
- [115] J. W. Hutchinson and Z. Suo. *Mixed Mode Cracking in Layered Materials*, volume Volume 29, pages 63–191. Elsevier, 1991.
- [116] R. Hetnarski, M R. Eslami, and G. Gladwell. *Thermal stresses: advanced theory and applications*, volume 41. Springer, 2009.
- [117] H. Tada, P. Paris, and G. R. Irwin. *Handbook for stress analysis of cracks, Third Edition*. ASME, New York, USA, 2000.
- [118] G. R. Irwin. Analysis of stresses and strains near the end of a crack traversing a plate. *J. Appl. Mech.*, 24:361–364, 1957.
- [119] Z. T. Bieniawski. Mechanism of brittle fracture of rock. *International Journal of Rock Mechanics and Mining Sciences and Geomechanics Abstracts*, 4(4):395–406, 1967.
- [120] Stuart D. C. Walsh and Ilya N. Lomov. Micromechanical modeling of thermal spallation in granitic rock. *International Journal of Heat and Mass Transfer*, 65:366–373, 2013.
- [121] P. W. J. Glover, P. Baud, M. Darot, P. G. Meredith, S. A. Boon, M. LeRavalec, S. Zoussi, and T. Reuschle. α/β phase transition in quartz monitored using acoustic emissions. *Geophysical Journal International*, 120(3):775–782, 1995.
- [122] I. Van der Molen. The shift of the α - β transition temperature of quartz associated with the thermal expansion of granite at high pressure. *Tectonophysics*, 73(4):323–342, 1981.

- [123] J. Byerlee. Brittle-ductile transition in rocks. *Journal of Geophysical Research*, 73(14):4741–4750, 1968.
- [124] B. Lewis and G. von Elbe. *Combustion, Flames and Explosions of Gases (Second Edition)*. Academic Press, Pittsburgh, USA, 1961.
- [125] Lino Guzzella and Antonio Sciarretta. *Vehicle propulsion systems*, volume 1. Springer, 2007.
- [126] Ghazi A Karim. *Fuels, energy, and the environment*. CRC Press, 2012.
- [127] H. Martin. Heat and mass transfer between impinging gas jets and solid surfaces. *Advances in Heat Transfer*, 13:1–60, 1977.
- [128] VDI-Gesellschaft Verfahrenstechnik. *VDI Heat Atlas*. Springer Berlin Heidelberg, 2010.
- [129] M. Kaiser. Modeling the time and cost to drill an offshore well. *Energy*, 34(9):1097–1112, 2009.
- [130] C. Kipsang. Cost model for geothermal wells. In *Proceedings World Geothermal Congress 2015*.
- [131] J. L. Thorogood. A mathematical model for analysing drilling performance and estimating well times. *Offshore Europe, 8-11 September, Aberdeen, United Kingdom*, 1987.
- [132] BCAS - British Compressed Air Society Limited BCAS - fact sheed no. 010 - the cost of compressed air. 2007.
- [133] D. Vogler, R. Settgast, C. Annavarapu, P. Bayer, and F. Amann. Hydro - mechanically coupled flow through heterogeneous fractures. In *41st Workshop on Geothermal Reservoir Engineering, Stanford University, Stanford, California, February 22 - 24, 2016*.
- [134] M. Schuler, T. Rothenfluh, and Ph. Rudolf von Rohr. Numerical analysis of penetration lengths in submerged supercritical water jets. *The Journal of Supercritical Fluids*, 82:213–220, 2013.

- [135] B. Valley and K. Evans. Stress orientation to 5km depth in the basement below Basel (Switzerland) from borehole failure analysis. *Swiss Journal of Geosciences*, 102(3):467, 2009.
- [136] J. Zhang. Pore pressure prediction from well logs: Methods, modifications, and new approaches. *Earth-Science Reviews*, 108(1):50–63, 2011.
- [137] J. Zhang. Effective stress, porosity, velocity and abnormal pore pressure prediction accounting for compaction disequilibrium and unloading. *Marine and Petroleum Geology*, 45:2–11, 2013.
- [138] L. Lake. *Petroleum Engineering Handbook*, volume 2. Society of Petroleum Engineers, 2006.
- [139] M. T. Albdiry and M. F. Almensory. Failure analysis of drillstring in petroleum industry: A review. *Engineering Failure Analysis*, 65:74–85, 2016.
- [140] O. Vaisberg, O. Vincke, G. Perrin, J. P. Sarda, and J. B. Fay. Fatigue of drillstring: State of the art. *Oil and Gas Science and Technology - Rev. IFP*, 57(1):7–37, 2002.
- [141] M. Connell, D. Headrick, and C. Isennock. Coiled tubing: Applications for today’s challenges. *Petroleum Engineer International*, 72(7), 1999.
- [142] P. McCutcheon, T. Miszewski, and J. Heaton. Coiled tubing drilling: Directional and horizontal drilling with larger hole sizes. In *SPE Annual Technical Conference and Exhibition, 8-10 October, San Antonio, Texas, USA*. Society of Petroleum Engineers.
- [143] L. J. Leising and I. C. Walton. Cuttings-transport problems and solutions in coiled-tubing drilling. *SPE Drilling and Completion*, 17(01), 2002.
- [144] P. C. Crouse and W. B. Lunan. Coiled tubing drilling - expanding application key to future. In *SPE/ICoTA Coiled Tubing Roundtable, 5-6 April, Houston, Texas, 2000*. Society of Petroleum Engineers.

- [145] J. R. Bailey, E. Biediger, V. Gupta, D. Ertas, W. C. Elks, and F. E. Dupriest. Drilling vibrations modeling and field validation. In *IADC/SPE Drilling Conference, 4-6 March, Orlando, Florida, USA*. Society of Petroleum Engineers.
- [146] J. R. Bailey and S. M. Remmert. Managing drilling vibrations through BHA design optimization. *SPE Drilling and Completion*, 25(04), 2010.
- [147] G. Heisig and M. Neubert. Lateral drillstring vibrations in extended-reach wells. In *IADC/SPE Drilling Conference, 23-25 February, New Orleans*. Society of Petroleum Engineers.
- [148] M. Kant, Edoardo Rossi, Dustin Becker, and P. Rudolf Von Rohr. Enhancing the drilling process for geothermal resources by combining conventional drilling and the spallation technology. In *41st Workshop on Geothermal Reservoir Engineering, Stanford University, Stanford, California, 2017*.
- [149] E. Rossi, M. Kant, F. Amann, M. Saar, and Ph. Rudolf von Rohr. The effects of flame-heating on rock strength: Towards a new drilling technology. In *51st US Rock Mechanics / Geomechanics Symposium, San Francisco, California, USA, 25-28 June 2017*.
- [150] H. Tian, M. Ziegler, and T. Kempka. Physical and mechanical behavior of claystone exposed to temperatures up to 1000°C. *International Journal of Rock Mechanics and Mining Sciences*, 70:144–153, 2014.
- [151] Sheng Huang and Kaiwen Xia. Effect of heat-treatment on the dynamic compressive strength of Longyou sandstone. *Engineering Geology*, 191:1–7, 2015.
- [152] P. G. Meredith and B. K. Atkinson. Fracture toughness and sub-critical crack growth during high-temperature tensile deformation of Westerly granite and Black gabbro. *Physics of the Earth and Planetary Interiors*, 39(1):33–51, 1985.
- [153] Shi Liu and Jinyu Xu. An experimental study on the physico-mechanical properties of two post-high-temperature rocks. *Engineering Geology*, 185:63–70, 2015.

- [154] H. Yavuz, S. Demirdag, and S. Caran. Thermal effect on the physical properties of carbonate rocks. *International Journal of Rock Mechanics and Mining Sciences*, 47(1):94–103, 2010.
- [155] C. Germaý and T. Richard. The scratch test: A high resolution log of rock strength with application to geomechanic and petrophysic. In *SPWLA 55th Annual Logging Symposium, 18-22 May, Abu Dhabi, United Arab Emirates, 2015*. Society of Petrophysicists and Well-Log Analysts.
- [156] F. Dagrain, T. Richard, and C. Germaý. The rock strength device: A scratching apparatus to determine rock properties. In *The 7th National Congress on theoretical and applied Mechanics NCTAM*.
- [157] T. Richard, F. Dagrain, E. Poyol, and E. Detournay. Rock strength determination from scratch tests. *Engineering Geology*, 147:91–100, 2012.
- [158] M. Hajpal and A. Torok. Mineralogical and colour changes of quartz sandstones by heat. *Environmental Geology*, 46(3):311–322, 2004.
- [159] W. Zhang, Q. Sun, Sh. Hao, J. Geng, and C. Lv. Experimental study on the variation of physical and mechanical properties of rock after high temperature treatment. *Applied Thermal Engineering*, 98:1297–1304, 2016.
- [160] H. Tian, T. Kempka, N. Xu, and M. Ziegler. Physical properties of sandstones after high temperature treatment. *Rock Mechanics and Rock Engineering*, 45(6):1113–1117, 2012.
- [161] ASTM International, standard test method for thermal diffusivity by the flash method, USA, 2013.
- [162] C. Clauser and E. Huenges. *Thermal Conductivity of Rocks and Minerals in Rock Physics and Phase Relations*, pages 105–126. American Geophysical Union, 2013.
- [163] M. Osako, A. Yoneda, and E. Ito. Thermal diffusivity, thermal conductivity and heat capacity of serpentine (antigorite) under high

- pressure. *Physics of the Earth and Planetary Interiors*, 183(1):229–233, 2010.
- [164] M. H. B. Nasser and B. Mohanty. Fracture toughness anisotropy in granitic rocks. *International Journal of Rock Mechanics and Mining Sciences*, 45(2):167–193, 2008.
- [165] T. Rothenfluh, M. Schuler, and Ph. Rudolf von Rohr. Development of a calorimeter for heat flux measurements in impinging near-critical water jets confined by an annular wall. *The Journal of Supercritical Fluids*, 73:141–150, 2013.
- [166] G. Bussmann, R. Bracke, T. Eicker, V. Wittig, H. Tuente, J. Gueldenhaupt, L. Groening, F. Kiel, K. Maeggi, and B. Montag. Geostar - a scalable borehole heat exchanger plant for growing district heating systems and constricted large urban infrastructures. In *Proceedings World Geothermal Congress 2015, Melbourne, Australia, 19-25 April 2015*.
- [167] I. Moeck, T. Bloch, R. Graf, St. Heuberger, P. Kuhn, H. Naef, M. Sonderegger, St. Uhlig, and M. Wolfram. The st. gallen project: development of fault controlled geothermal systems in urban areas. In *Proceedings World Geothermal Congress, Melbourne, Australia, 19-25 April 2015*.
- [168] A. Reinicke, E. Rybacki, S. Stanchits, E. Huenges, and G. Dresen. Hydraulic fracturing stimulation techniques and formation damage mechanismsimplications from laboratory testing of tight sandstoneproppant systems. *Chemie der Erde - Geochemistry*, 70:107–117, 2010.
- [169] M. McClure and R. Horne. An investigation of stimulation mechanisms in enhanced geothermal systems. *International Journal of Rock Mechanics and Mining Sciences*, 72:242–260, 2014.
- [170] A. Ghassemi. A review of some rock mechanics issues in geothermal reservoir development. *Geotechnical and Geological Engineering*, 30(3):647–664, 2012.

- [171] T. Kraft, P. Mai, S. Wiemer, N. Deichmann, J. Ripperger, P. Kstli, C. Bachmann, D. Fh, J. Wssner, and D. Giardini. Enhanced geothermal systems: Mitigating risk in urban areas. *Eos, Transactions American Geophysical Union*, 90(32):273–274, 2009.
- [172] V. Braeuer, S. Heusermann, and A. Pahl. Rock stress measurements in the grimsel underground rock laboratory and their geological interpretation. *Nuclear Engineering and Design*, 116(1):21–24, 1989.
- [173] V. Doetsch, J. Gischig, F. Amann, C. Madonna, M. Jalali, B. Valley, and K. Evans. Reservoir stimulation experiments at the Grimsel Test Site: Stress measurements using hydraulic fracturing, hydraulic tests on pre-existing fractures and overcoring. In *Fall Meeting of the American Geophysical Union, San Francisco, CA, 2015*. American Geophysical Union.
- [174] M. Ziegler, S. Loew, and F. Amann. Near-surface rock stress orientations in alpine topography derived from exfoliation fracture surface markings and 3D numerical modelling. *International Journal of Rock Mechanics and Mining Sciences*, 85:129–151, 2016.
- [175] S. Kurosawa, S. James, M. Yui, and M. Ibaraki. Model analysis of the colloid and radionuclide retardation experiment at the Grimsel Test Site. *Journal of colloid and interface science*, 298(1):467–475, 2006.
- [176] G. Wallis. *One-dimensional two-phase flow*. New York, McGraw-Hill, 1969.
- [177] P. Griffith and G. B. Wallis. Two-phase slug flow. *Journal of Heat Transfer*, 83(3):307–318, 1961.
- [178] C. P. Stemmet, J. N. Jongmans, J. van der Schaaf, B. F. M. Kuster, and J. C. Schouten. Hydrodynamics of gasliquid counter-current flow in solid foam packings. *Chemical Engineering Science*, 60(22):6422–6429, 2005.
- [179] Y. Taitel and D. Barnea. Counter current gas-liquid vertical flow, model for flow pattern and pressure drop. *International Journal of Multiphase Flow*, 9(6):637–647, 1983.

- [180] S. Ghiaasiaan. *Two-phase flow, boiling, and condensation: in conventional and miniature systems*. Cambridge University Press, 2007.
- [181] H. Richter. Flooding in tubes and annuli. *International Journal of Multiphase Flow*, 7(6):647–658, 1981.
- [182] J. Jeong. Counter-current flow limitation velocity measured in annular narrow gaps formed between large diameter concentric pipes. *Korean Journal of Chemical Engineering*, 25(2):209–216, 2008.
- [183] D.M. Thornley, W.B. Wilkinson, and A. Parker. A preliminary investigation of the release of oil from contaminated clays and other fine-grained sediments during consolidation. *Quarterly Journal of Engineering Geology and Hydrogeology*, 39(4):375–390, 2006.
- [184] M. Pereira, C. Panisset, A. Martins, C. S. M. Barrozo, and C. Atade. Microwave treatment of drilled cuttings contaminated by synthetic drilling fluid. *Separation and Purification Technology*, 124:68–73, 2014.
- [185] A. Saasen, B. Dahl, and K. Jødestøl. Particle size distribution of top-hole drill cuttings from norwegian sea area offshore wells. *Particulate Science and Technology*, 31(1):85–91, 2013.
- [186] B. Joodi, M. Sarmadivaleh, V. Rasouli, and A. Nabipour. Simulation of the cutting action of a single PDC cutter using DEM. *WIT Transactions on Engineering Sciences*, 81:143–150, 2012.
- [187] W. Krech, F. Henderson, and K. Hjelmstad. *A standard rock suite for rapid excavation research*. US Bureau of Mines, 1974.
- [188] H. Bhat, C. Sammis, and A. Rosakis. The micromechanics of westerley granite at large compressive loads. *Pure and applied geophysics*, 168(12):2181–2198, 2011.
- [189] T. Johnson. Measurement of elastic properties and static strength. Report, Defense Technical Information Center, 1984.

- [190] G. Dollinger and H. Handewith. Correlations between punch test results and rock physical properties. In *4th North American Rock Mechanics Symposium, 31 July-3 August, Seattle, Washington, 2000*. American Rock Mechanics Association.
- [191] P. Santi, J. Holschen, and R. Stephenson. Improving elastic modulus measurements for rock based on geology. *Environmental and Engineering Geoscience*, 6(4):333–346, 2000.
- [192] J. Andersson. *Rock mass response to coupled mechanical thermal loading: Aspö Pillar Stability Experiment, Sweden*. Thesis, 2007.
- [193] J. Sulem, M. Cerrolaza, and B. Ammiar. Numerical analysis of the role of microstructure for contact problems in rock mechanics. In *Numerical Methods in Geotechnical Engineering, Paris, 2002*.
- [194] J. Zar. The use of a laser for ARPA military geophysics program (rock mechanics and rapid excavation), AVCO-everett research laboratory,(everett, mass.). Report, Final Technical Report on BuMines (ARPA) Contract HO210039, 1972.
- [195] N. Park. *Discrete element modeling of rock fracture behavior: fracture toughness and time-dependent fracture growth*. Thesis, 2006.
- [196] P. Lemiszki and J. Landes. Fracture toughness testing of core from the cambro-ordovician section on the oak ridge reservation. In *2nd North American Rock Mechanics Symposium, Montreal, Quebec, Canada, 1996*. American Rock Mechanics Association.
- [197] L. Peck, C. Barton, and R. Gordon. Microstructure and the resistance of rock to tensile fracture. *Journal of Geophysical Research: Solid Earth (19782012)*, 90(B13):11533–11546, 1985.
- [198] T. Backers. *Fracture toughness determination and micromechanics of rock under mode I and mode II loading*. Geoforschungszentrum Potsdam, 2005.
- [199] J. Schoen. *Physical properties of rocks: Fundamentals and principles of petrophysics*, volume 65. Elsevier, 2015.

- [200] T.-f. Wong and W. Brace. Thermal expansion of rocks: some measurements at high pressure. *Tectonophysics*, 57(2-4):95–117, 1979.
- [201] G. Smith. *The effect of size and thermal expansion of aggregates on the durability of concrete*. Thesis, 1951.
- [202] A. Khalafalla. Effect of frequency and temperature on rock dielectric properties. Report, Defense Technical Information Center, 1973.
- [203] Callie Hull. *International critical tables of numerical data, physics, chemistry and technology*, volume 1. National Academies, 1933.
- [204] J. Sundberg and M. Landell. Aspo Hard Rock Laboratoy - determination of linear thermal expansion - sampels from borehole KA2599G01, Aspo HRL. Report, 2002.
- [205] M. Zamora, D. VoThanh, G. Bienfait, and J. Poirier. An empirical relationship between thermal conductivity and elastic wave velocities in sandstone. *Geophysical Research Letters*, 20(16):1679–1682, 1993.
- [206] M. T. Morgan and G. A. West. *The Thermal Conductivity of the Rocks in the Bureau of Mines Standard Rock Suite*, pages 79–90. Springer US, Boston, MA, 1983.
- [207] W. Somerton. *Thermal properties and temperature-related behavior of rock/fluid systems*, volume 37. Elsevier, 1992.
- [208] F. Birch. Thermal conductivity and diffusivity. *Geological Society of America Special Papers*, 36:243–266, 1942.
- [209] W. Woodside and J. Messmer. Thermal conductivity of porous media. II. consolidated sands. *Journal of applied physics*, 32(9):1688–1699, 1961.

List of publications

Journal publications

1. **Michael A. Kant**, Edoardo Rossi, Claudio Madonna, Dragana Hoeser, Philipp Rudolf von Rohr (2017), A theory on thermal spalling of rocks with a focus on thermal spallation drilling, *Journal of Geophysical Research: Solid Earth*, Volume 122, Issue 3, Pages 1805-1815
2. **Michael A. Kant**, Jens Ammann, Edoardo Rossi, Claudio Madonna, Dragana Hoeser, Philipp Rudolf von Rohr (2017), Thermal properties of Central Aare Granite for temperatures up to 500°C: Irreversible changes due to thermal crack formation, *Geophysical Research Letters*, Volume 44, Pages 771-776.
3. **Michael A. Kant**, Thierry Meier, Edoardo Rossi, Martin Schuler, Dustin Becker, Dragana Hoeser, Philipp Rudolf von Rohr (2017), Thermal spallation drilling - an alternative drilling technology for hard rock drilling, *OIL GAS European Magazine* 1/2017, Pages 23-25.
4. **Michael A. Kant**, Philipp Rudolf von Rohr (2016), Determination of surface heat flux distributions by using surface temperature measurements and applying inverse techniques, *International Journal of Heat and Mass Transfer*, Volume 99, Pages 1-9.
5. **Michael A. Kant**, Philipp Rudolf von Rohr (2016), Minimal required boundary conditions for the thermal spallation process of granitic rocks, *International Journal of Rock Mechanics and Mining Sciences*, Volume 84, Pages 177-186.

Patents

1. Philipp Rudolf von Rohr, **Michael A. Kant**, Edoardo Rossi, Process and Device for Thermal Bore Hole Enlargement, EP17188149.3, *patent pending*

Book chapters

1. Philipp Rudolf von Rohr, **Michael A. Kant**, Tobias Rothenfluh, Martin Schuler, Panagiotis Stathopoulos (2015). Drilling and Completion. In Hirschberg, Wiemer, Burgherr (Eds.), Energy from the Earth: Deep Geothermal as a Resource for the Future?, vdf Hochschulverlag, Zurich, Switzerland

Conference contributions

Oral presentations:

1. Edoardo Rossi, **Michael A. Kant**, Florian Amann, Martin O. Saar, Philipp Rudolf von Rohr, The effects of flame-heating on rock strength: Towards a new drilling technology, 51st US Rock Mechanics/Geomechanics Symposium, 25-28 June 2017, San Francisco, California, United States
2. **Michael A. Kant**, Edoardo Rossi, Dustin Becker, Philipp Rudolf von Rohr, Enhancing the drilling process for geothermal resources by combining conventional drilling and the spallation technology, Stanford Geothermal Workshop 2017, 13-15 February 2017, Palo Alto, California, United States
3. **Michael A. Kant**, Edoardo Rossi, Dragana Hoeser, Philipp Rudolf von Rohr. Thermal Spallation Drilling, an Alternative Drilling Technology for Deep Heat Mining - Performance Analysis, Cost Assessment and Design Aspects, Stanford Geothermal Workshop 2017, 13-15 February 2017, Palo Alto, California, United States
4. **Michael A. Kant**, Dragana Hoeser, Martin Schuler, Edoardo Rossi, Philipp Rudolf von Rohr. Thermal Spallation Drilling - an Alternative Drilling Technology for Hard Rock Drilling, Celle Drilling, 12-13 September 2016, Celle, Germany
5. Thierry Meier, **Michael A. Kant**, Dragana Brkic. Philipp Rudolf von Rohr. Flame-Jet Drilling: An Alternative Technique to Access Deep Heat reservoirs, 1st Bochum Drilling Dialogue, 13-14 June 2016, Bochum, Germany

6. **Michael A. Kant**, Thierry Meier, Dragana Brkic, Philipp Rudolf von Rohr. Benefits and Limitations of Thermal Spallation Drilling as an Alternative Drilling Technology, 1st Bochum Drilling Dialogue, 13-14 June 2016, Bochum, Germany
7. **Michael A. Kant**, Claudio Madonna, Philipp Rudolf von Rohr. Spallation Drilling - A Novel Drilling Technology with the Potential to Boost Deep Geothermal Energy in Switzerland, MaP Graduate Symposium, 9 June 2016, Zurich
8. **Michael A. Kant**, Philipp Rudolf von Rohr. Hydrothermal Spallation Drilling a Novel Drilling Technology for Deep Heat Mining - Required and Optimal Operating Conditions, 10th European Congress of Chemical Engineering, 27 September - 1 October 2015, Nice, France
9. Dragana Brkic, **Michael A. Kant**, Thierry Meier, Phillip Rudolf von Rohr. Influence of Process Parameters on Thermal Rock Fracturing Under Ambient Conditions, World Geothermal Congress, 19-25 April 2015, Melbourne, Australia
10. **Michael A. Kant**, Dustin Becker, Dragana Brkic, Thierry Meier, Martin Schuler, Philipp Rudolf von Rohr. Investigation of a Novel Drilling Technology Influence of the Surface Temperature for Hydrothermal Spallation Drilling, World Geothermal Congress, 19-25 April 2015, Melbourne, Australia
11. Thierry Meier, Dragana Brkic, Martin Schuler, **Michael A. Kant**, Philipp Rudolf von Rohr. Hydrothermal Spallation Drilling - Design and Experiments for a Novel Drilling Technology, World Geothermal Congress, 19-25 April 2015, Melbourne, Australia

Poster presentations:

1. Edoardo Rossi, **Michael A. Kant**, Philipp Rudolf von Rohr, and Martin O. Saar. Combining conventional and thermal drilling in order to increase speed and reduce costs of drilling operations to access deep geothermal resources, European Geosciences Union, General Assembly 2017, 23-28 April 2017, Vienna Austria

2. **Michael A. Kant**, Edoardo Rossi, Philipp Rudolf von Rohr, Design of a combined mechanical/thermal drilling system for hard rock drilling, 1st Bochum Drilling Dialogue, 13./14. June 2016, Bochum, Germany
3. **Michael A. Kant**, Claudio Madonna, Alex Hob, Jean-Pierre Burg, Philipp Rudolf von Rohr. Investigation of the boundary conditions and process mechanisms of spallation drilling, SCCER-SoE Annual Conference, 10-11 September 2015, Neuchatel, Switzerland
4. Dragana Hoeser, Thierry Meier, **Michael A. Kant**. Philipp Rudolf von Rohr. Process conditions required for flame-jet drilling, SCCER-SoE Annual Conference, , 10-11 September 2015, Neuchatel, Switzerland

Curriculum Vitae

Michael Kant

Date of birth:	December 3, 1987
Place of birth:	Wiesbaden, Germany
Nationality:	German
09/2013–09/2017	Doctoral studies at the Institute of Process Engineering, ETH Zurich (Prof. Dr. Ph. Rudolf von Rohr)
10/2007–07/2012	Studies of Mechanical Engineering at Karlsruhe Institute of Technology (academic degree: Dipl.-Ing.)
10/2010–03/2011	Internship at Schaeffler (UK) Ltd., Great Britain
09/1998–06/2007	High School in Beilstein and Hochheim, Germany (academic degree: Abitur)

Zurich, September 2017